Exciton-photon hybridisation in ZnSe based microcavities

Arran Curran

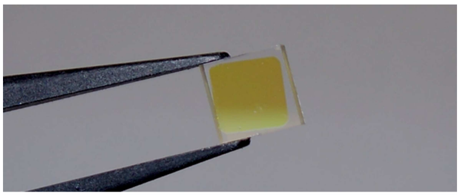

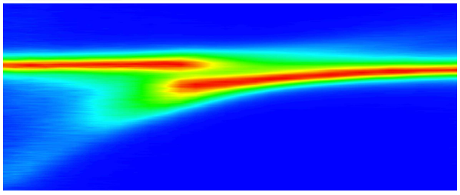

Submitted for the degree of
Doctor of Philosophy in Physics

Heriot-Watt University
School of Engineering and Physical Sciences

April 2008

Abstract

This thesis presents the design, fabrication and experimental analysis of ZnSe based microcavities. Semiconductor microcavities are micro-structures in which the exciton ground state of a semiconductor is coupled to a photonic mode of an optical cavity. The strong light matter coupling mixes the character of excitons and photons, giving rise to the lower and upper cavity polaritons, quasiparticles with an unusual dispersion due to the extreme mass contrast between the composite exciton and photon. In particular, the dispersion of the lower polariton forms a dip around the lowest energy state with zero in-plane momentum. In this dip, which can be seen as a trap in momentum space, the polaritons are efficiently isolated from dephasing mechanisms involving phonons. The features of these quasiparticles promise a variety of applications, for instance lasing without inversion and micro-optical parametric amplifiers, and an environment to study fundamental physics, such as Bose-Einstein condensation in the solid state.

By overcoming the longstanding fabrication problems of ZnSe-based microcavities, the enlarged exciton binding energy in combination with the use of highly reflective dielectric mirrors makes this material system ideally suited to the realisation of polariton-based devices operating at room temperature. An epitaxial liftoff technology is developed that relies on the high etch selectively between the ZnSe heterostructure and a novel II-VI release layer, MgS.

Three hybrid microcavities are fabricated with the liftoff technique and spectroscopically characterised. Angle resolved transmission experiments reveal strong hybridization of the ZnSe/Zn$_{0.9}$Cd$_{0.1}$Se quantum well excitons and cavity photons in a fixed microcavity. A completely length tunable microcavity is presented and shown to exhibit similar dispersion as for the fixed microcavity, with the addition of evidencing the cavity polariton bottleneck effect. The nonlinear optical features are discussed. Photoluminescence data is presented that evidences the first observation of the build up of cavity polaritons at the edge of the momentum space trap in the lower polariton branch, the bottleneck effect, in a ZnSe based microcavity. Finally, lasing at room temperature in the blue spectral region is presented for a metal/dielectric hybrid microcavity.

Acknowledgements

During my postgraduate research and beyond, my thesis supervisors, Professor Richard J. Warburton and Professor Ajoy K. Kar gave me the opportunity to pursue my childhood dream, for which I am truly grateful. Thank you.

I am honored to have this thesis examined by Professor Jeremy J. Baumberg and Dr. Jens Ebbecke.

My research at Heriot-Watt University directly involved the Molecular Beam Epitaxial group run by Dr. Kevin A. Prior, who supplied me with high quality II-VI samples and many stimulating conversations. The semiconductor samples discussed in this thesis were grown by members of his team, namely, Jessica Morrod, Christine Bradford and Richard Moug. I am particulary grateful to colleague, Russell Barbour for his excellent work in developing a length tunable optical cavity. Thank you to Paul Dalgarno, Brian Gerardot, Henry Bookey and Adam Caley who have suffered my relentless assumption that they are there to answer all my questions.

Finally, I wish to express my gratitude to Shelagh who has endlessly offered personal and financial support throughout my undergraduate and postgraduate years. Throughout my PhD Indira has continued to support and love me, even when I have struggled to reciprocate, during periods when Heriot-Watt seemed more like home. Finally, I wish to acknowledge the support and transference of wisdom from my mother, Dianne.

Declaration

This page is intentionally left blank

Contents

List of Figures

Chapter 1

Introduction

1.1 General introduction

The interactions of photons with matter underly much of the physics of semiconductors and have been utilised in many modern technologies. For this reason the interaction of light and matter is a subject of fundamental interest. Consequently much is understood in this area and many new fields of physics have been established. In particular, the focus on light matter interactions has lead to the vertical cavity surface emitting laser (VCSEL), pioneered by Iga *et al.* [1] in the 1980s. The VCSEL has many advantages over the traditional edge emitting semiconductor diode laser, the most notable being the beam shape produced by the device. Edge emitters emit an elliptical beam due to their planar configuration, whereas the VCSEL, as the name suggests, emits normal to the plane of the heterostructure and therefore can produce a spherical Gaussian beam. This has positive effects on many of the application areas [2]. In addition the VCSEL lends itself to mass production due to the simplified testing procedures, where large numbers of devices can be simultaneously tested.

The drive in developing and optimizing the VCSEL led to the first demonstration of quantum electrodynamic phenomena in a solid state environment, viewed as the manifestation of vacuum-field Rabi splitting in analogy to similar phenomena observed in atomic physics. Weisbuch *et al.* [3] were the first to show that for resonant exciton-photon interactions exceeding the damping of the two composite oscillators (*strong coupling regime*), a new pair of quasiparticles are formed, the *cavity polaritons*. Figure 1.1 shows the concept of the cavity polariton where the composite exciton, $|X\rangle$,

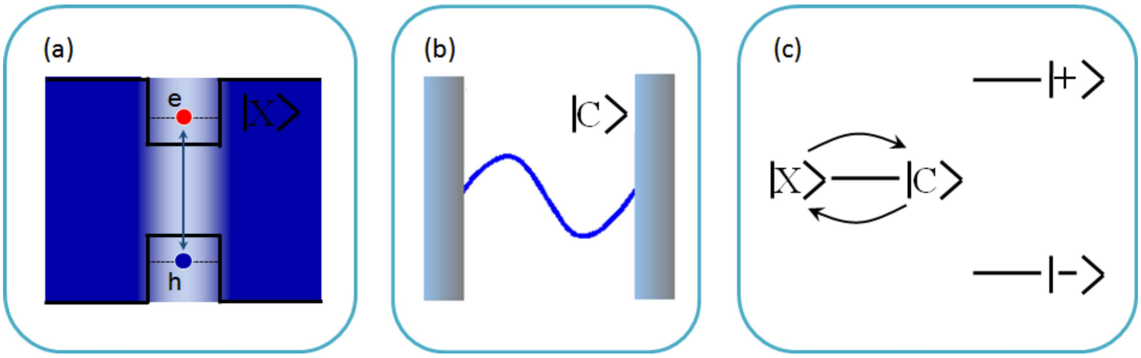

Figure 1.1: (a),(b) Schematic of the components of the cavity polariton, the exciton, $|X\rangle$ and cavity photon, $|C\rangle$. (c) The strong hybridisation leads to an oscillation from exciton to photon and splits the modes into two new states, the upper, $|+\rangle$ and lower, $|-\rangle$ cavity polaritons.

and cavity photon, $|C\rangle$, are combined in a microcavity to produce the upper, $|+\rangle$ and lower, $|-\rangle$ cavity polaritons spectrally separated by the normal mode splitting, $\hbar\Omega$. The microcavity permits control of both the electronic and photonic states, making it ideal for the study of cavity polaritons. [4, 5, 6, 7, 8].

In fact the microcavity has led to many phenomena seen in the field of atom physics being implemented in a solid state environment:

1. Vacuum-field Rabi splitting.
2. Bose-Einstein Condensation.
3. Polariton amplification leading to lasing *without* population inversion.

The idea of a condensate of cavity polaritons, and its application, an ultralow threshold laser was first discussed by Imamoğlu *et al.* [9] in 1996. Figure 1.2 details the physics of a cavity polariton condensate and the resulting emission of coherent light. Electron-hole pairs are injected, typically with a laser, well above the energy of the cavity polaritons. Cooling mechanisms lead to the formation of excitons and thus cavity polaritons, in particular polaritons populate the lower branch with high momentum. These hot polaritons can further relax down the dispersion curve through phonon

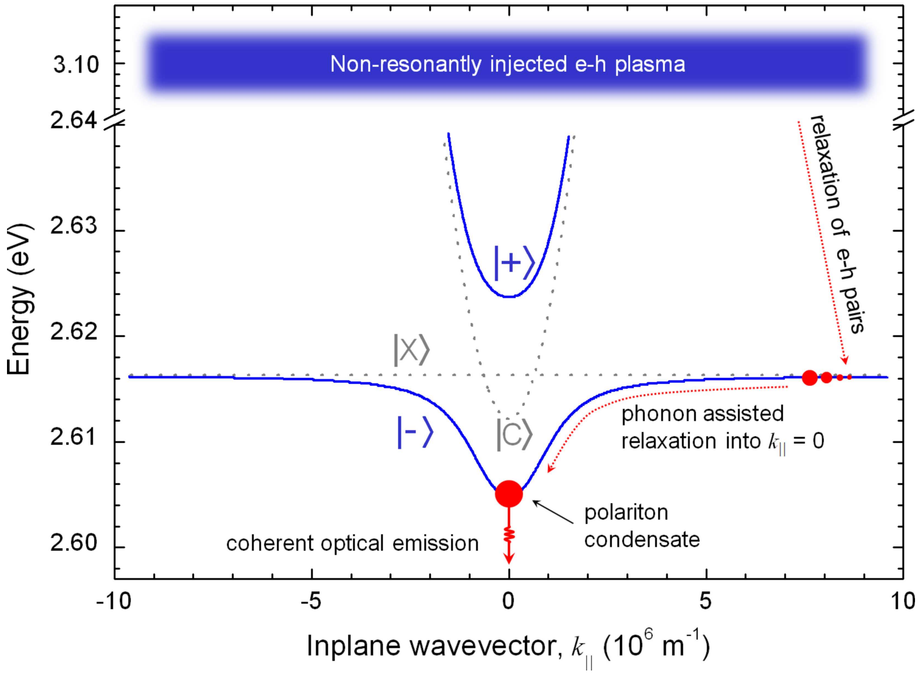

Figure 1.2: Electron-hole pairs, non-resonantly injected, relax to form high momentum cavity polaritons, which in turn become trapped within the dip in the lower polariton dispersion, through phonon assisted cooling. This leads to a build up of polaritons at $k_{||} = 0$, and beyond a critical density, a polariton condensate which can optically relax, emitting a stream of coherent photons. The exciton,$|X\rangle$, cavity photon, $|C\rangle$, upper, $|+\rangle$ and lower, $|-\rangle$ cavity polaritons are labeled.

assisted cooling. Due to the unusual shape of the lower cavity polariton dispersion curve, the polaritons can become trapped near $k_{||} = 0$, and beyond a critical density, begin to condensate into a degenerate state. At this point the only mechanism for the polaritons to further relax is found in the release of a coherent beam of light within a small solid angle normal to the microcavity plane. A crucial feature of a polariton condensate is that due to the characteristics of the bosonic cavity polaritons, condensation can occur at higher temperatures than that of the atomic physics counterpart. This is due to the fact that the mass of the cavity polariton is much less than the mass of a typical atom used in atomic Bose-Einstein condensation experiments. The steep dispersion of the lower polariton around $k_{||} = 0$, due to its photonic component, results in the temperature and density criteria for condensation being more readily achievable.

After the first demonstration of a microcavity operating in the strong coupling regime in 1992, the research focussed on linear characterisation such as the in-plane dispersion [10] and the improvement of the cavity structures. In 1996 it was reported that spontaneous transitions to a coherent state in the polariton system had been observed in a GaAs based microcavity [11]. But this was later shown to be explained in the traditional framework of population inversion of excitons [12]. Conclusive spontaneous phase transitions occurring in the strong coupling regime in a GaAs based microcavity has not been evidenced to date. The relaxation of the polaritons appears to be too inefficient to achieve a condensation in the lowest energy state and the strong coupling regime breaks down due to the high densities required. However it has been possible to demonstrate the quantum degeneracy of polaritons by resonantly exciting the polariton modes. The coherence of the incident laser beam is transferred to the polariton system. This coherence is efficiently preserved in a microcavity because pure dephasing mechanisms are not efficient and the relaxation time is comparable to the population lifetime of the polaritons. The absence of efficient pure dephasing mechanisms enables the transfer of the injected polariton excitation to other states preserving the initial coherence. Based on this property it has been possible to demonstrate a parametric polariton wavemixing, in which the coherence of the incident laser is transferred to a signal and an idler polariton mode, satisfying energy and in-plane momentum conservation [6]. This process is highly efficient and presents potential for technical application in ultrafast amplification devices [8].

During the later years of the 1990s and into the early years of the new millennium, the first strongly coupled microcavities in the ZnSe [13], CdTe [14, 15], and GaN [16] material systems were realised. The advantage of these systems is the larger oscillator strength of the exciton. CdTe based microcavities have seen much success with Le Si Dang *et al.* demonstrating a non-linear stimulation effect occurring in the strong coupling regime under non-resonant excitation [17] and later, convincing evidence for the first Bose-Einstein condensate in a solid state environment [18]. GaN based microcavities are promising, however GaN quantum wells are plagued by quantum confined Stark broadening [19]. The work reported has been based on bulk GaN microcavities [20, 21].

To date a ZnSe hybrid device operating in the strong regime has been reported in 1995 [13] and the Purcell effect for a CdSe/ZnSe quantum dot in 2005 [22]. Monolithic devices have shown clear strong coupling for CdTe [17, 18] and GaN [20] systems but not for ZnSe. The advantage of working within the ZnSe material system is that higher exciton binding energies than that of the GaAs system are accessible along with narrower exciton linewidths than that found within the GaN system. The large oscillator strength, thus large binding energies, found in the ZnSe material system combined with the high performance of dielectric mirrors makes these samples ideally suited to the study of parametric scattering [6, 8] and Bose-Einstein condensation. Additional, ZnSe-based microcavities offer operation in the strong coupling regime within the blue/green spectrum. This is advantageous since it makes ZnSe-based devices applicable to a broad range of industries such as medical imaging, printing, storage and display.

1.2 Scope and outline

This thesis is concerned with the ZnSe material system. A new fabrication technology, based on an epitaxial liftoff technique using a novel MgS sacrificial layer, has been realised, perfected and successfully applied to the fabrication of hybrid ZnSe based microcavities that operate in both the weak and strong coupling regimes. Chapter 2 will discuss the fundamentals of semiconductor heterostructures, optical resonators and the combination of the two, the microcavity, all in the context of ZnSe based microcavities. The remainder of the thesis will address two areas. First, the fabrication techniques developed, perfected and applied to realise a variety of hybrid ZnSe based microcavities will be discussed in chapters 3 and 4. A detailed discussion of the spectroscopic techniques used to probe the microcavities will also be given in Chapter 4. Secondly, the optical properties of fabricated microcavities will be discussed. A fixed hybrid microcavity and fully tunable microcavity (chapter 5) operating in the strong coupling regime will be presented. The observation of nonlinear phenomena in a hybrid microcavity is reported in chapter 6. Population inversion in a monolithic hybrid ZnSe based microcavity operating at room temperature is presented in section 6.2 followed by the first demonstration of the cavity polariton bottleneck in the ZnSe material system (section 6.1). The thesis will be summarised along with a review of the current status of ZnSe based microcavities and future prospects in chapter 7.

Chapter 2

Semiconductor microcavities

This chapter discusses the two components of the cavity polariton, namely the confined exciton and cavity photon and will conclude with a description of the strong hybridisation of the two quantized states.

2.1 Semiconductor basics

In the following sections the behaviour of the fundamental excitation, the exciton, will be described for bulk and low dimensional semiconductor heterostructures, in particular the quantum well.

2.1.1 Bulk semiconductors

At room temperature semiconductors have a lower conductivity than a metal and the introduction of impurities results in an increase in the conductivity, whereas the opposite is true for metals. With controlled introduction of impurities, semiconductors can cover a large range of conductivity and as such are technologically extremely useful. Group IV elements such as silicon and germanium are classed as elemental semiconductors; binary compounds such as gallium arsenide (GaAs) and zinc selenide (ZnSe) are classed as compound semiconductors and are formed from elements of the groups III-V and II-VI, respectively. Figure 2.1(a) shows the schematic of the band structure of a typical semiconductor where the lowest (highest) energy level of the conduction (valence) band occurs for electrons with zero wavevector. This type of semiconductor is aptly categorised as a direct bandgap semiconductor, such as GaAs and ZnSe. Due to the crystalline structure the wavefunctions of the valence and conduction electrons overlap to form energy bands, separated by a forbidden zone, the bandgap, typically of the order of $1-3$ eV. At absolute zero, an intrinsic semiconductor would be indistinguishable from an insulator. With the introduction of thermal energy the probability of electrons contributing to the overall conductivity is finite and the material's conductivity increases monotonically with temperature. This is an idealistic view of semiconductors and neglects the importance of doping. The work presented in this thesis is not concerned with doping of semiconductors. The semiconductor samples presented in this thesis have a negligible doping concentration of $\sim 10^{15}$ cm^{-3} (10^{7} ZnSe atoms per dopant), measured by secondary ion mass spectrometry [23].

Absorption of photons of energy greater than the bandgap results in electrons being promoted into the conduction band from the valence band, where the ionized site is treated as a particle (hole) with finite mass, forming an electron-hole (e-h) pair. Absorption data clearly shows the contribution of free e-h pairs to the absorption, as a broad band due to the large range of kinetic energy of the particles above the bandgap. Additionally, e-h pairs can be bound together, resulting in a Coulomb correlated quasiparticle. The Coulomb coupling leads to the so called exciton with hydrogenic-like bound levels. These excitations differ from the free e-h pair and are identified by a narrow atomic-like absorption peak on the low energy shoulder of the absorption spectrum. The observation of bound excitons in a bulk semiconductor was first reported by Sturge *et al.* [24].

A simplified mathematical description of the localised bulk exciton is that of a hydrogen-like atom. The Hamiltonian describing the e-h interaction within an idealised solid with isotropic, nondegenerate parabolic bands is composed of the kinetic energy of the electron and hole and their Coulomb interaction,

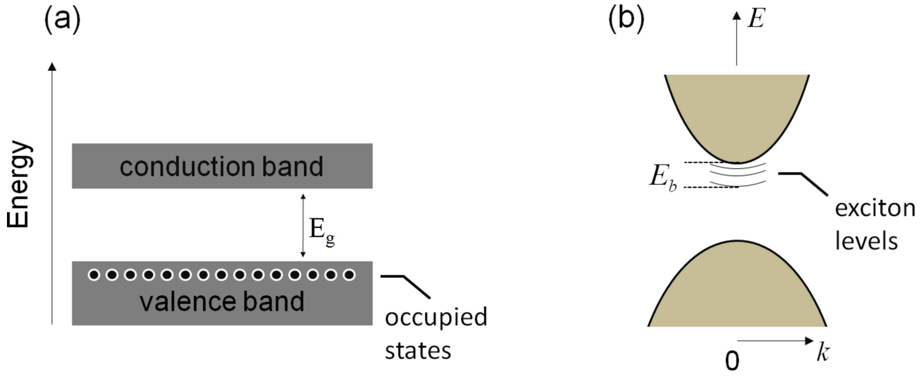

Figure 2.1: (a) Simplified band diagram, where valence (conduction) electron wavefunctions overlap to form a continuum, the valence (conduction) band, separated by a forbidden gap of magnitude E_g. (b) Energy dispersion for conduction and valence bands showing also the exciton levels.

$$H_{e-h} = E_g + \frac{p_e^2}{2m_e^*} + \frac{p_h^2}{2m_h^*} - \frac{e^2}{\epsilon|r_e - r_h|}, \tag{2.1}$$

with eigensolutions,

$$E_n = E_g - \frac{\mu e^4}{2\epsilon^2\hbar^2 n^2} + \frac{\hbar^2 k^2}{2m_X^*} \quad n = 1, 2, 3, ... \quad . \tag{2.2}$$

The energy levels given by (2.2) are composed of the bandgap, E_g, the exciton binding energy, E_b, (2nd term in (2.2)) and the dispersive kinetic energy term (3rd term in (2.2)). The binding energy of the exciton is equal to one effective Rydberg, Ry^* scaled by the reduced mass of the exciton, $\mu \sim m_e^*$, and the background dielectric constant of the semiconductor, ϵ_b, $Ry^* = \frac{\mu e^4}{2\epsilon_b^2\hbar^2}$. The dispersive kinetic energy of the exciton is dependent on its motion in momentum space, k and its effective mass, $m_X^* \sim m_h^*$. Similarly, the exciton is bound within an effective Bohr radius, $a_B^* = \frac{\epsilon}{\mu}a_B$. This description of the exciton is valid within the context of the assumptions made, namely the introduction of an effective mass to allow for the treatment of the electron and holes as free particles and that Coulomb screening effects have been accounted for by the use of a macroscopic dielectric constant, ϵ.

$$\frac{1}{\mu} = \frac{1}{m_e^*} + \frac{1}{m_h^*} \quad \text{and} \quad m_X^* = m_e^* + m_h^* \tag{2.3}$$

For bulk GaAs and ZnSe the electron (hole) effective masses, m_e (m_h) are 0.065 (0.5) and 0.15 (0.6) [25] and the background dielectric constant, ϵ_b is 12.9 and 8.1 resulting in a binding energy, E_b of 4.7 and 24.9 meV, respectively. The significantly higher binding energy for ZnSe gives the first indication of the advantages of wide-bandgap semiconductors.

Excitonic effects play a significant role in modifying the optical recombination of e-h pairs. To further understand excitonic effects, interband transition probabilities must be considered. Interband recombination transition rates are given by Fermi's golden rule [26],

$$W = \frac{2\pi}{\hbar} \sum_{f,i} \mid \langle f \mid -e\mathbf{r} \cdot \mathbf{E} \mid i \rangle \mid^2 \delta(E_f - E_i + \hbar\omega), \tag{2.4}$$

where i and f denote the initial and final states, respectively. The strength of an optical transition is characterised by the oscillator strength, f_{osc} defined by [26],

$$f_{osc} = \frac{2m_e\omega}{\hbar} \mid \langle f \mid \mathbf{E} \cdot \mathbf{r} \mid i \rangle \mid^2, \tag{2.5}$$

where m_e is the free electron mass and ω is the transition angular frequency. The oscillator strength of an e-h pair can be thought of as how well the electron and hole wavefunctions are matched. The probability of an electron wavefunction overlapping with a hole wavefunction is enhanced by excitonic effects: e-h correlation leads to an increase in the oscillator strength by a so called Sommerfeld factor. The exciton can be treated as a single quasiparticle with an oscillator strength given by,

$$f_{osc}^{X} = \frac{2m_e\omega}{\hbar} \mid \langle u_c \mid \mathbf{E} \cdot \mathbf{r} \mid u_v \rangle \mid^2 \cdot \frac{1}{\pi a_B^3}, \tag{2.6}$$

where $\langle u_c \mid \mathbf{E} \cdot \mathbf{r} \mid u_v \rangle$ is the valence to conduction band matrix element and a_B is the Bohr radius.

2.1.2 Low dimension semiconductors

In a direct bandgap semiconductor the reduction in dimensionality in one or more dimensions leads to the quantisation of the continuum above the band-edge and a further increase in the exciton correlation. Interest in low-dimensionality of semiconductors increased during the early 1970s after reported device possibilities made by Esaki *et al.* [27]. Soon after, the quantization of the above band continuum was shown in two fundamental experiments by Esaki *et al.* [28] and Dingle *et al.* [29]. The simplest example of reduced dimensionality is the quantum well, an epitaxial layer of semiconductor (well), between two layers of thick,[1] higher bandgap semiconductor (barrier). When the well thickness is small enough, discrete levels begin to form above the band-edge continuum, resulting in a series of energy levels given by (2.7). Figure 2.2(a) shows this remarkable phenomenon as seen by Dingle *et al.* [29]. The absorption spectra of a series of heterostructures show the transition from bulk to quantisation of the above band-edge continuum with reduced epitaxial layer thickness. For the 400 nm sample the low energy absorption peak corresponds to the formation of bulk excitons above which the broad spectral absorption is due to the formation of free e-h pairs. The effects of reduced dimensionality are seen in the absorption spectra for the thinner (21 and 14 nm) samples. The reduced freedom in the growth direction quantises the electron and hole states leading to a series of absorption peaks. Assuming the quantisation energy is larger than the exciton binding energy, and that the exciton

---

[1] Thicker than the penetration depth of the electron or hole wavefunctions.

is at rest (strong confinement limit), the Coulomb correlated electrons and holes form a series of levels, E_n given by,

$$E_n = E_g + \frac{\hbar^2 \pi^2 n^2}{2 m_X^* L_z^2} \quad n = 1, 2, 3, \ldots . \tag{2.7}$$

In addition to the energy quantisation, the density of states (DOS) significantly deviates from that of the three dimensional case (3D). Figure 2.2(b) shows the DOS for 3D and 2D. The 2D DOS is readily calculated by examining the problem in k-space. Looking at the allowed states within energies E and $E + dE$ and taking the parabolic approximation of electron dispersion,

$$\rho_{3D} = \frac{\sqrt{2 m_X^{*3} E}}{\pi^2 \hbar^3} \quad \text{and} \quad \rho_{2D} = \frac{n m_X^*}{\pi \hbar^2} \quad n = 1, 2, 3, \ldots . \tag{2.8}$$

The DOS for each 2D sub-band is evidently independent of energy and well thickness with steps at E_n.

The effects of reduced dimensionality are demonstrated in photoluminescence spectra of, for example, a ZnSe/ZnCdSe multiple quantum well (MQW). Figure 2.3 shows the photoluminescence from a II-VI MQW that will be discussed further in chapter 3. The two main optical features are found at 2.54 eV and 2.69 eV and are attributed to optical recombination of confined excitons in the ZnCdSe well and bulk excitons in the ZnSe barrier. The relative size of the two features is a direct consequence of the increased quantum efficiency induced by the confinement effects discussed.

The increase in quantum efficiency from bulk to reduced dimensionality can be appreciated by returning to the oscillator strength where a further concentration occurs in a similar way as before. Continuing with the infinite well approximation the 2D oscillator strength per unit area for a confined exciton reads as [30],

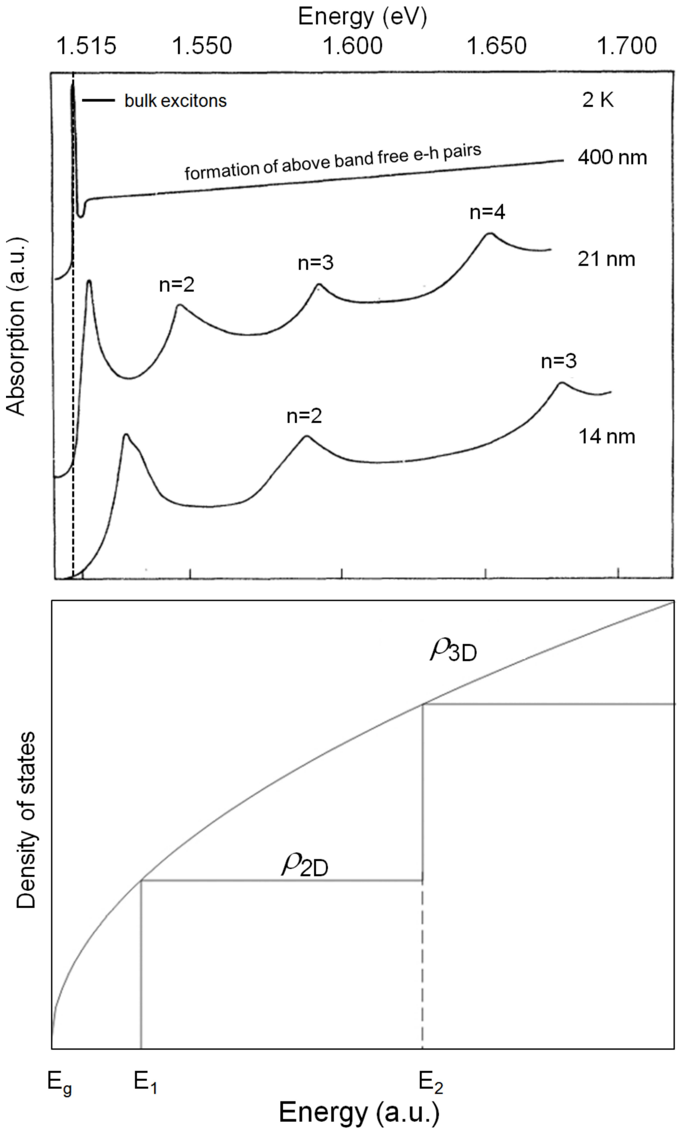

Figure 2.2: (a) Absorption spectra of GaAs epitaxial layers ranging from 400 to 14 nm thickness at 2 K. Taken from Dingle *et al.* [29]. (b) Calculated density of states for bulk (3D) and 2D semiconductors.

$$f_{osc}^{2D} = \frac{2m_e\omega}{\hbar} \mid \langle u_c \mid \mathbf{E} \cdot \mathbf{r} \mid u_v \rangle \mid^2 \cdot \frac{8}{\pi a_B^2}. \tag{2.9}$$

In the exact 2D case, where the well thickness $L_w \ll a_B^*$ the exciton binding energy is also increased by a factor of 4 although this is not the case for a finite quantum well, where the binding energy is increased by, typically, a factor of two.

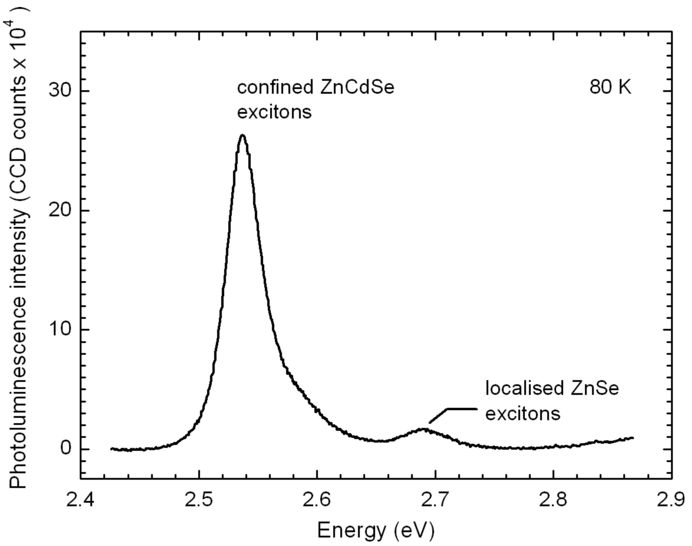

Figure 2.3: Photoluminescence from a ZnSe/ZnCdSe multiple quantum well, highlighting the concentration of the oscillator strength due to reduced dimensionality.

2.2 Optical confinement

The observation of cavity polaritons requires the controlled confinement of the exciton to be coupled with a confined cavity photon. The characteristic features of photonic modes in a planar optical cavity are dominated by the reflectance of the mirrors. A distributed Bragg reflector (DBR) offers a high degree of control and performance and is ideally suited for microcavity structures. The following section discusses the details of a planar optical cavity and the controlled confinement of photonic modes.

2.2.1 Distributed Bragg reflectors

DBRs are composed of alternating high and low refractive index material such that each successive reflection of light at the design wavelength, λ_{sb}, undergoes a π-phase shift to give constructive interference at the DBR surface. This is achieved by controlling the layer thickness, L_j of the two materials of refractive index, n_j, $L_j = \frac{\lambda_{sb}}{4n_j}$. Figure 2.4(b) shows the schematic of a typical DBR along with the optical paths of

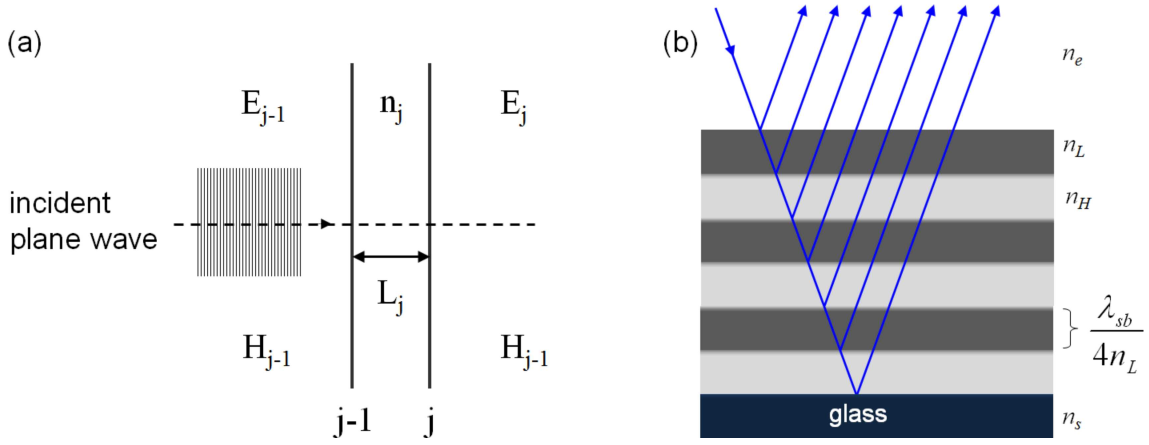

Figure 2.4: (a) Schematic of adjacent layers within a quarter wave stack (DBR) of N layers, with incident radiation E_{j-1} and H_{j-1} at the $j-1$ interface. n_j and α_j are, respectively, the refractive index and absorption coefficient of the jth layer. Due to the periodicity of the structure $n_j \equiv n_{j\pm2}, n_{j\pm4}$, etc. The same is true for the absorption coefficient, α. (b) Schematic of a dielectric stack showing the optical reflections of incident light. Refraction has been neglected for simplicity. Not to scale.

incident light.

The transfer matrix (TM) is the most versatile method when dealing with optical thin films. For a detailed discussion of optical thin films and their application see [31]. Here the TM method is described for a DBR. Each layer in the DBR is represented by a 2×2 matrix that contains the real (refractive index) and imaginary (absorption coefficient) parts of the dielectric function of the layer.

Figure 2.4 (a) defines the mathematical parameters required for a TM calculation. Refractive index, n_j and absorption coefficient, α_j define the *j-th* layer in the periodic structure. E_j and H_j are, respectively, the electric and magnetic field amplitudes. The incident radiation normal to the $j-1$ interface is given by,

$$\begin{pmatrix} E_{j-1} \\ H_{j-1} \end{pmatrix} = \begin{pmatrix} \cos\phi_j & \frac{i}{\epsilon_j}\sin\phi_j \\ i\epsilon_j \sin\phi_j & \cos\phi_j \end{pmatrix} \begin{pmatrix} E_j \\ H_j \end{pmatrix}, \tag{2.10}$$

where $\phi_j = \frac{2\pi d_j}{\lambda}(n_j - ik_j)\cos\theta$ and $\epsilon_j = n_j - ik_j$. The 2×2 matrix, M_j, in (2.10) contains all the optical information for any given layer in the DBR and simply taking the product of all the layers gives a complete optical description. For a stack of $2N$ layers the incident radiation at the DBR surface is,

$$\begin{pmatrix} E_o \\ H_o \end{pmatrix} = \prod_{i=1}^{N} M_i \begin{pmatrix} 1 \\ n_s \end{pmatrix}. \tag{2.11}$$

The electric and magnetic fields at the last interface have been normalized so that, $E_N = 1$ and $H_N = n_s E_N$, where n_s is the substrate refractive index. Equation (2.11) can be used to calculate the reflectivity, R, transmission, T and absorption, A for any given combination of dielectric stacks. Additionally excitonic effects can be incorporated by representing an active layer with a Lorentzian oscillator. The reflection and transmission for a DBR are given by the matrix elements, E_o and H_o of (2.11),

$$R = \left| \frac{E_o - H_o}{E_o + H_o} \right|^2 \qquad \text{and} \qquad T = \frac{4n_s}{\mid E_o - H_o \mid^2}. \tag{2.12}$$

The expression for reflectivity is simulated and presented in figure 2.5 along with the phase of reflected light as a function of wavelength. The phase of reflected light is determined by the stacking order of the DBR and this is important since the electric field profile within a cavity is determined by the phase of reflection. This will be discussed further in section 2.2.2. The DBR is characterised by a spectrally broad, high reflectivity band centred around the design wavelength, the stop band, with oscillating side bands on either side. Standard materials, SiO_2 and TiO_2 are used in the simulation with wavelength independent refractive indices 2.36 and 1.46 respectively. Three examples of reflectance are presented for N = 3, 4 and 7 (6, 8 and 14 quarter wave layers) at a design wavelength of λ_{sb} = 500 nm.

The reflectivity dependence on N can be seen more readily in the following limits. For a lossless quarter wave stack surrounded by a medium of refractive index n_e, the reflectance at normal incidence in the spectral region of λ_{sb} can be reduced to [32],

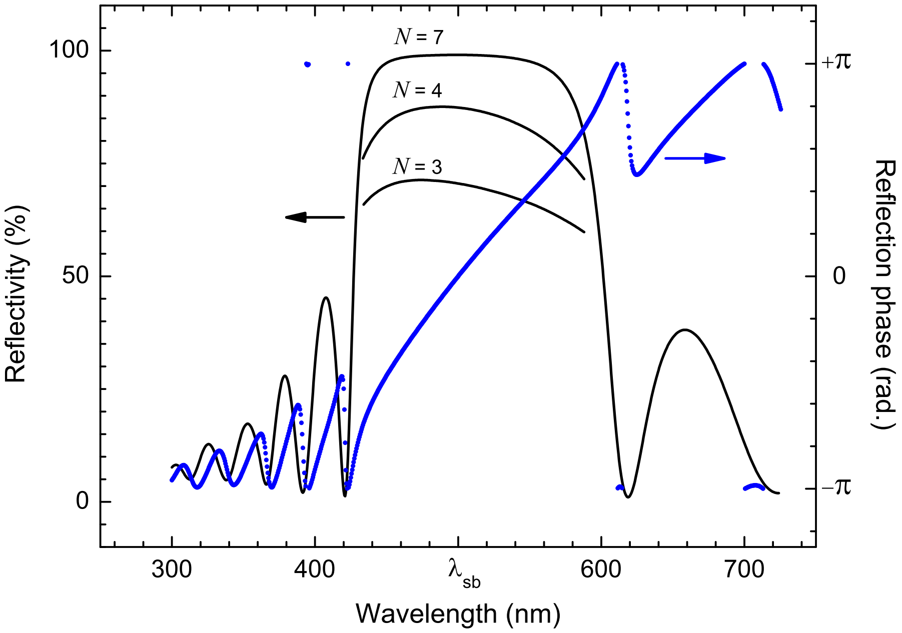

Figure 2.5: Reflectance and reflectance phase for a typical dielectric stack. The reflectance is simulated for 3 different values of N, 3, 4 and 7 at a design wavelength of λ_{sb} = 500 nm. Materials TiO$_2$ (n_H = 2.36) and SiO$_2$ (n_L = 1.46) on a glass substrate (n = 1.52) are simulated. The DBR is assumed to be surrounded by vacuum.

$$R = \left(\frac{1 - \frac{n_e}{n_s} \left(\frac{n_1}{n_2} \right)^{2N}}{1 + \frac{n_e}{n_s} \left(\frac{n_1}{n_2} \right)^{2N}} \right)^2 , \tag{2.13}$$

with a spectral width, $\Delta_{sb} = \frac{4\lambda_{sb}\Delta n}{\pi n_{eff}}$ where the substrate, external, first and second layer refractive indices are n_s, n_e, n_1 and n_2 respectively. The effective refractive index, n_{eff} is given by, $2(\frac{1}{n_1} + \frac{1}{n_2})^{-1}$. The main points to note from (2.13) are that the reflectivity within the stop band increases as the power of $2N$ and as $\frac{n_1}{n_2} \to 0$. A maximum contrast of indices, Δn, between the DBR composite materials is desirable along with low absorption coefficients at the design wavelength. The number of pairs can then be readily adjusted until the desired reflectivity is achieved.

Due to the distributed nature of DBRs, incident radiation undergoes phase dispersion $\theta(\omega)$ and a reflection delay, $\tau(\omega)$. It is customary to interpret the reflection delay by introducing an imaginary fixed phase mirror that when positioned at a physical depth

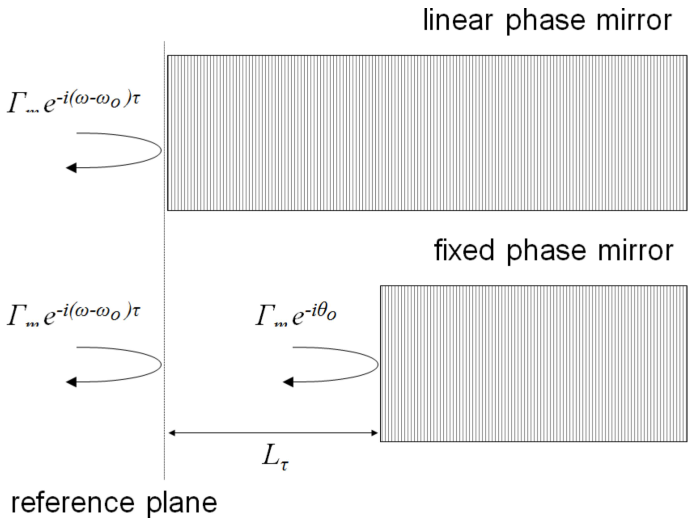

Figure 2.6: By replacing a linear phase mirror with a fixed phase mirror, the concept of an *apparent depth*, L_τ is illustrated. Reflected radiation is identical from both mirrors when the fixed phase mirror is placed at a depth L_τ relative to the linear phase mirror.

relative to the linear phase mirror appears identical. Figure 2.6 illustrates this. This interpretation is satisfied when the *apparent depth*, L_τ [33],

$$L_\tau = \frac{c\tau}{2n_e}, \tag{2.14}$$

where the reflection delay, τ is given by,

$$\tau = \frac{\lambda_{sb}}{2c}\frac{n_1 n_2}{n_1 - n_2} \quad N \gg 1, \quad n_1 \gg n_2. \tag{2.15}$$

Equation (2.15) is an approximation for the case when the number of layers, $N \gg 1$. For the situation where $N \to 1$ or $\Delta n \to 0$ see Babic *et al.* [33]. Note that n_1 and n_2 are the refractive indices of the high and low refractive index material respectively, irrespective of stacking order. The significance of (2.14) and (2.15) is that for a high refractive index contrast, one can achieve a smaller cavity mode volume, which is desirable when trying to maximise exciton-photon interactions. The use of dielectric mirrors has the further advantage of eliminating disorder effects due to the alloy used

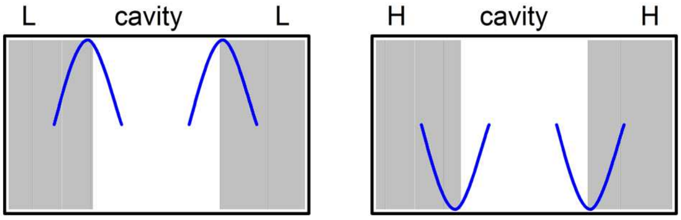

Figure 2.7: Possible configurations of sample structure both of which produce a symmetrical distribution of the electric field. The phase dependency of the electric field results in antinodes being found at low index-cavity interfaces and nodes at high index-cavity interfaces independent of cavity index within the limit that $n_c > n_H$.

in semiconductor mirrors. Additionally, advantages of employing dielectric mirrors is seen in the width of the stop band which is dependent on the contrast of the refractive indices. The AlAs/$Al_{0.4}Ga_{0.6}As$ semiconductor mirror used in [3] gives a stop band of 55 nm, a factor of 5 narrower compared to a TiO_2/SiO_2 DBR of the same reflectivity.

2.2.2 Planar optical cavities

Combining two DBRs, forming a planar optical cavity of refractive index, n_c, will support a mode m when the physical cavity length $L_c = \frac{m\lambda}{2n_c}$.

Figure 2.7 shows the significance of the sequence of the periodic structure with respect to high (H) and low (L) refractive indices. The electric field within the cavity experiences an index dependent phase shift at each DBR-cavity interface. For the case when $n_c > n_H$, L-cavity-L (LL) configurations result in antinodes at the DBR-cavity interface. HH configurations result in nodes at the DBR-cavity interface. For the case when $n_c < n_H$ the situation is reversed. This work only considers the case where $n_c > n_H$, which is the case for a ZnSe-based microcavity. The difference in how the electric field propagates through a HH or LL configuration means that LL structures will always produce n antinodes whereas HH will have $n + 1$ antinodes within the cavity.

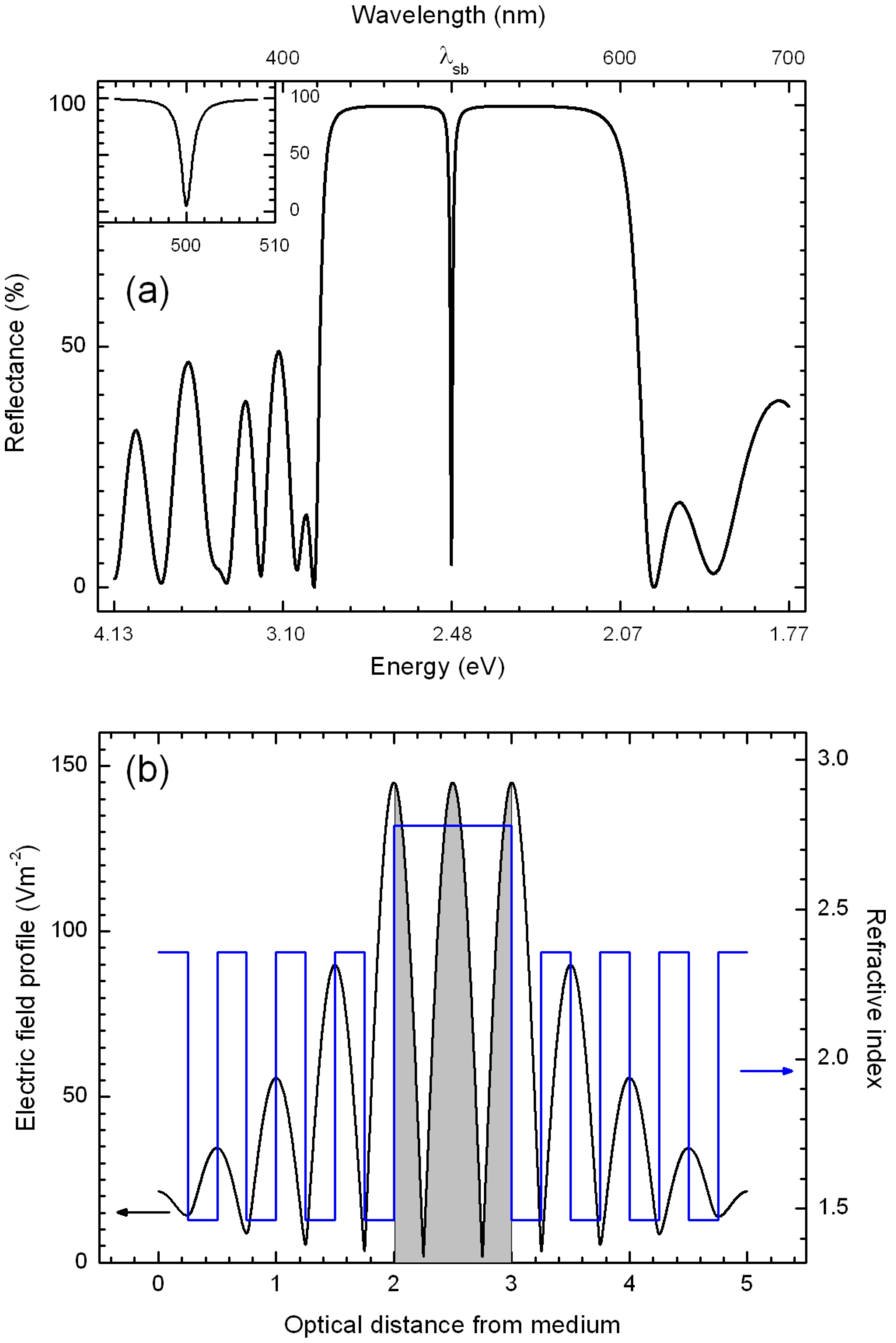

Figure 2.8: (a) Reflection for a planar cavity composed of two TiO_2/SiO_2 DBRs with N = 8 and an air gap of one optical length at 500 nm. (b) Electric field and refractive index profiles of the cavity. The electric field is simulated for incident light at λ_{sb} = 500 nm with a power of 1 W m^{-2}.

Using the same parameters as figure 2.5 with N = 8 and an air gap of one optical length at a wavelength of 500 nm, the simulated reflectance and electric field profile are presented in figure 2.8. In an optical cavity the high reflectance stop band, Δ_{sb}, is interrupted by a transmission line corresponding to the mode of the cavity, with a full width at half maximum, γ_c, given by,

$$\gamma_c = \frac{\lambda_{sb}^2(1-\sqrt{R_1R_2})}{2\pi n_c L_{eff}}, \tag{2.16}$$

where L_{eff} is the effective cavity length given by $L_c + 2L_\tau$. Like the reflectance, γ_c is dependent on the number of layers, N in the DBR and that the cavity linewidth needs to be comparable to the exciton linewidth, γ_X for optimum coupling (see section 2.3.2). It is desirable to have a high reflectance, prolonging the photonic lifetime, whilst ensuring $\gamma_c \sim \gamma_X$. For a LL TiO$_2$/SiO$_2$ cavity with N = 1 and a ZnSe spacer of physical length $\frac{\lambda_{sb}}{n_c}$ and refractive index, n_c = 2.78 the peak reflectivity is, R = 0.976 at λ_{sb} = 500 nm which, from (2.14), leads to an apparent depth L_τ = 172 nm for each DBR and an effective cavity length, L_{eff} = 524 nm. Note that the external refractive index, n_e in (2.14) is taken as the internal refractive index of the cavity, n_c. From (2.16) the linewidth of such a microcavity is, γ_c = 0.65 nm $\equiv$ 3.2 meV. Typically, at 80 K, ZnCdSe quantum well excitons have a linewidth, γ_X $\sim$ 10 meV and 5 meV at 4 K. Taking the parameters of [3] and neglecting disorder broadening mechanisms, the cavity linewidth is found to be, γ_c = 0.12 nm $\equiv$ 0.23 meV. This satisfies the matching criteria for strong coupling for the Al$_{0.2}$Ga$_{0.8}$As/GaAs quantum well with a linewidth of $\gamma_X \sim 2$ meV from [3].

An important feature of an optical cavity is the dispersion and how it compares to that of an uncoupled exciton. Uncoupled optical cavities and excitons have, respectively, the following dispersion,

$$E_C(k_{||}) \approx E_C(0) + \frac{\hbar^2}{2m_C^*}k_{||}^2 \quad \text{and} \quad E_X(k_{||}) = E_X(0)^{(n=1)} + \frac{\hbar^2}{2m_X^*}k_{||}^2, \tag{2.17}$$

where the effective mass of the cavity photon, $m_C^* = \frac{\hbar n_c}{c}k_z$. For the lowest resonant mode at λ = 500 nm in a cavity of refractive index 2.78, the photon mass is $1.4 \times 10^{-5} m_e$ (1.3$\times 10^{-35}$ kg), 5 orders of magnitude lower than a typical ZnSe/ZnCdSe quantum well exciton. This is crucial to cavity polariton dispersion measurements since the dispersion of the exciton is very weak in comparison to the cavity photon, and with careful design, the dispersion of the two states can be such that they intersect in momentum space.

2.3 Cavity polaritons

In the previous sections the fundamental components of the cavity polariton, the exciton and cavity photon, have been discussed. The following will address the hybridization of the two states and detail the optical characteristics of the cavity polariton.

2.3.1 Light-matter hybridization

The polariton is the resulting quasiparticle of a photon coupling with a fundamental excitation with the same wavevector. In the strong coupling regime the energy oscillates from photon to excitation and back again; the photon is absorbed to form an excitation before it exits the system and the excitation annihilates before dephasing, producing a photon. The polariton is thus the fundamental propagation mode of an excitation through a medium. The exciton-polariton was first studied by Hopfield [34] in bulk semiconductors. However, the coupling efficiencies for exciton-polaritons are sufficiently low to hinder experimental studies due to momentum conversation rules. The advantage of combining quantum well excitons with cavity photons is that momentum conservation can be satisfied in a controlled environment. The microcavity is such an environment and ideally suited to the study of cavity polaritons. The interconversion between photons and excitons can be observed in the optical spectrum which, in the strong coupling regime, exhibits two resonant features energetically separated by a normal mode splitting, $\hbar\Omega$,

$$\hbar\Omega \propto \sqrt{\frac{f_{osc}^{2D} N_{qw}}{L_{eff}}}, \tag{2.18}$$

where N_{qw} is the number of quantum wells within the microcavity. In order to maximise $\hbar\Omega$ a material with a high oscillator strength is desirable for the active medium. This is one of the factors that has hindered experimental studies with III-V microcavities, since the relatively low oscillator strength in this system leads to thermalisation of the excitons and the breakdown of strong coupling for high excitation densities. ZnSe based microcavities with large oscillator strength are a very attractive alternative. Additionally, the choice of materials for the Bragg reflector is important since a high refractive index contrast leads to a reduced effective cavity length. The design and fabrication of ZnSe based microcavities with ZnCdSe quantum wells will be discussed in chapter 3. A detailed description of the cavity polariton is given in the following section.

2.3.2 Cavity polariton dispersion: Coupled oscillator model

Treating the exciton and photon as quantum mechanical oscillators the coupling Hamiltonian is simply the sum of the Hamiltonian of the exciton, cavity photon and their interaction and is given by [35],

$$H_{cp} = \sum_{\mathbf{k}} E_C(k_{||}) a_{\mathbf{k}}^{\dagger} a_{\mathbf{k}} + \sum_{\mathbf{k}} E_X(k_{||}) b_{\mathbf{k}}^{\dagger} b_{\mathbf{k}} + \hbar \sum_{\mathbf{k}} \Omega (a_{\mathbf{k}}^{\dagger} b_{\mathbf{k}} + b_{\mathbf{k}}^{\dagger} a_{\mathbf{k}}), \tag{2.19}$$

where $a_{\mathbf{k}}^{\dagger}$ and $a_{\mathbf{k}}$ ($b_{\mathbf{k}}^{\dagger}$ and $b_{\mathbf{k}}$) are the creation and annihilation operators of the cavity photon (exciton) with in-plane wavevector **k**, respectively. The third term in (2.19) describes the coupling. The cavity polariton Hamiltonian 2.19 can be diagonalised to transfer it to the polariton basis and reads,

$$H_{cp} = \sum_{\mathbf{k}} E_l(k_{||}) p^{\dagger}_{\mathbf{k}} p_{\mathbf{k}} + \sum_{\mathbf{k}} E_u(k_{||}) u^{\dagger}_{\mathbf{k}} u_{\mathbf{k}}. \tag{2.20}$$

The lower and upper polariton boson operators, $p_{\mathbf{k}} = C_{\mathbf{k}} a_{\mathbf{k}} + X_{\mathbf{k}} b_{\mathbf{k}}$ and $u_{\mathbf{k}} = X_{\mathbf{k}} a_{\mathbf{k}} - C_{\mathbf{k}} b_{\mathbf{k}}$, respectively, are obtained through the unitary transformation [34],

$$\begin{pmatrix} p_{\mathbf{k}} \\ u_{\mathbf{k}} \end{pmatrix} = \begin{pmatrix} X_{\mathbf{k}} & C_{\mathbf{k}} \\ -C_{\mathbf{k}} & X_{\mathbf{k}} \end{pmatrix} \begin{pmatrix} b_{\mathbf{k}} \\ a_{\mathbf{k}} \end{pmatrix}. \tag{2.21}$$

The quantities $|C_{\mathbf{k}}|^2$ and $|X_{\mathbf{k}}|^2$ represent, respectively, the photonic and excitonic fraction of the lower polariton branch and are given by,

$$|C_{\mathbf{k}}|^2 = \frac{(\hbar\Omega)^2}{2\sqrt{\delta^{(-)2}_{\mathbf{k}} + (\hbar\Omega)^2}\left(\delta^{(-)2}_{\mathbf{k}} + \sqrt{\delta^{(-)2}_{\mathbf{k}} + (\hbar\Omega)^2}\right)}, \tag{2.22}$$

$$|X_{\mathbf{k}}|^2 = \frac{\delta^{(-)}_{\mathbf{k}} + \sqrt{\delta^{(-)2}_{\mathbf{k}} + (\hbar\Omega)^2}}{2\sqrt{\delta^{(-)2}_{\mathbf{k}} + (\hbar\Omega)^2}}, \tag{2.23}$$

where $\delta^{(\pm)}_{\mathbf{k}}$ is defined as $E_C(k_{||}) \pm E_X(k_{||})$. The eigenenergies of the cavity polariton are found from,

$$\begin{vmatrix} E_X(k_{||}) + i\gamma_X - E(k_{||}) & \hbar V \\ \hbar V & E_C(k_{||}) + i\gamma_c - E(k_{||}) \end{vmatrix} = 0, \tag{2.24}$$

where the matrix element between the exciton and cavity photon, $\hbar V$ is given by,

$$V = \sqrt{\frac{c\Gamma_o(1+\sqrt{R})}{n_c L_{eff}\sqrt{R}}}. \tag{2.25}$$

Only in the limit $\hbar V \gg \gamma_X, \gamma_c$ is $\hbar V$ a direct measurement of the polariton normal mode splitting. For a discussion of the case $\hbar V \sim \gamma_X, \gamma_c$ see [30]. In the work presented in this thesis $\hbar V > \gamma_X, \gamma_c$ which results in a normal mode splitting, $\hbar\Omega$ of magnitude $\Omega \sim V$. γ_X and γ_c are the nonradiative broadening of the exciton and the cavity mode linewidth, respectively. The nonradiative exciton lifetime, Γ_o is given by,

$$\Gamma_o = \frac{\pi e^2}{4\pi\epsilon_o n_c m_o c} f_{osc}^{2D}. \tag{2.26}$$

Combining (2.25) and (2.26) the exciton oscillator strength can be deduced from the experimentally observed spectral splitting of microcavities. This will be discussed in detail in chapter 5. The terms n_c and L_{eff} are defined in section 2.2.2. The solutions to (2.24) read as,

$$E_{l,u}(k_{||}) = \frac{\delta_{\mathbf{k}}^{(+)} - i(\gamma_X + \gamma_c)}{2} \pm \sqrt{\frac{1}{4}(\delta_{\mathbf{k}}^{(-)} + i(\gamma_X - \gamma_c))^2 + (\hbar V)^2}. \tag{2.27}$$

Examining (2.27) and considering only the resonant case ($\delta_0^{(-)} = E_C(k_{||}) - E_X(k_{||}) = 0$) the two regimes of exciton-photon coupling are clearly defined. In the case of $2\hbar V \leq \mid \gamma_c - \gamma_X \mid$ the second term in (2.27) is purely imaginary or zero and the dispersion is that of the two uncoupled states. This is the case of the weak coupling regime. The strong coupling regime occurs when $2\hbar V > \mid \gamma_c - \gamma_X \mid$ and two real polariton states exist with a splitting of the mixed mode energies given by,

$$\hbar\Omega = 2\sqrt{(\hbar V)^2 - \frac{1}{4}(\gamma_c - \gamma_X)^2}. \tag{2.28}$$

This result has a significant impact on the design of microcavities since the cavity mode linewidth, γ_c must be matched to γ_X in order to maximise the spectroscopic splitting, $\hbar\Omega$. This will be discussed further in chapter 3. The dispersion for a quan-

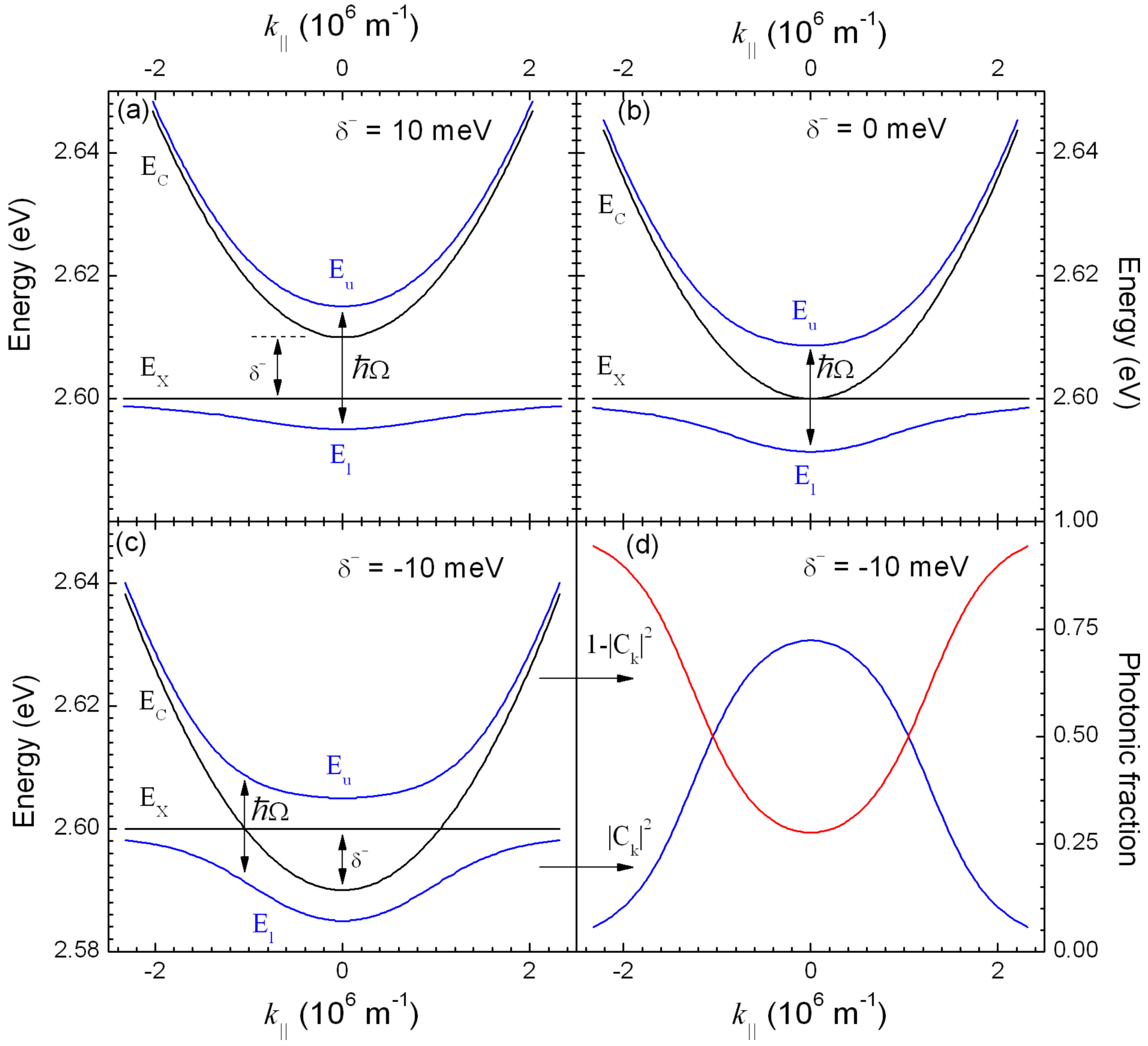

Figure 2.9: (a-c) Simulated cavity polariton dispersion for, $\delta_0^{(-)}$ = 10, 0 and -10 meV detuning. (d) For the case of negative detuning the photonic fractions of the upper, 1-$|C_\mathbf{k}|^2$, and lower, $|C_\mathbf{k}|^2$, polariton are presented.

tum well emitting at 2.60 eV embedded within a SiO$_2$/TiO$_2$ planar cavity detuned to $\delta_0^{(-)}$ = 10, 0 and -10 meV at normal incidence, is simulated (2.27) and presented in figure 2.9 (a-c) along with the uncoupled cavity photon and exciton (2.17). In the case of negative detuning the photonic fractions of the upper, 1-$|C_\mathbf{k}|^2$, and lower, $|C_\mathbf{k}|^2$, polariton are presented in figure 2.9 (d).

Chapter 3

Fabrication techniques and design of ZnSe based microcavities

As discussed in chapters 1 and 2 the oscillator strengths of excitons in the II-VI material system are sufficiently large that the microcavity continues to operate in the strong coupling regime under high excitation densities and at elevated temperatures. This is crucial to the study of cavity polariton condensates and the realisation of a viable microcavity device, which is reflected in the increase of the number of reports in recent years of II-VI and nitride based microcavities. GaN based microcavities are promising but to date only bulk GaN microcavities have shown strong coupling [20, 21] and are hampered by quantum confined Stark broadening of the exciton [19]. The ZnSe material system is very attractive due to its large oscillator strength [13, 36], which is highlighted in the typical binding energy of ZnSe excitons, $E_b \sim 30$ meV [37]. However, fabrication of II-VI based microcavities is a challenge with all growth techniques. II-VI based microcavities operating in the strong coupling regime have been reported, either involving growth-etch-growth processing [13, 38] or the use of semiconductor mirrors [18]. Hybrid devices have the advantage brought by the use of dielectric mirrors but are challenging to fabricate because of the difficulties in controlling the etching at the interface between the GaAs substrate and the epilayer. Large light penetration depth due to the low refractive index contrast is an inherent disadvantage of the monolithic approach. The growth of ZnSe based mirrors is very complex, requiring complicated epilayer sequences to mimic alloy compounds and to avoid the build up of strain. Currently the only report of a ZnSe based mirror is composed of ~ 500 epitaxial layers [39], but to date strong exciton photon coupling has not been achieved in an all semiconductor ZnSe based microcavity. This is acceptable in the case of

Lohmeyer *et al.* [39] where the focus is on monolithic ZnSe based vertical cavity surface emitting lasers (VCSEL). For a VCSEL, enhancement of the radiate rate of the internal exciton is proportional to the quality factor, $Q = \frac{E_c}{\gamma_c}$ and inversely proportional to the cavity mode volume, V ($\frac{Q}{V}$), whereas for a microcavity to operate in the strong coupling regime $\frac{Q}{\sqrt{V}}$ must be maximised. It is therefore desirable to use materials that have a high refractive index contrast, readily increasing Q and decreasing V. This makes the use of dielectric mirrors very attractive for any cavity polariton experiment.

The microcavities presented in this thesis are planar hybrid devices composed of a semiconductor active medium with dielectric or metallic mirrors. The following discussion is separated into two sections. Section 3.1 details the semiconductor heterostructure followed by a discussion of a selective etching technique, epitaxial liftoff [40] that was developed and perfected. This new technology has allowed for the fabrication of high quality ZnSe based microcavities without the problems encountered with previous hybrid technologies [36]. The key design considerations will conclude chapter 3.

3.1 Semiconductor growth and structure

The growth of the semiconductor active layer requires a number of different growth steps. Although the heterostructure is not in itself complicated from a growth point of view, it is, however made up of several constituent parts each of which had to be optimised before the full structure could be successfully grown. A systematic series of samples were grown, calibrating the Cd concentration, quantum well thickness and the overall thickness of the active layer. The following discussion details the heterostructure that was developed in collaboration with J. K. Morrod.

The active region [41] of all the microcavities discussed in this thesis was designed by the author and grown by members of K. A Prior's group by molecular beam epitaxy

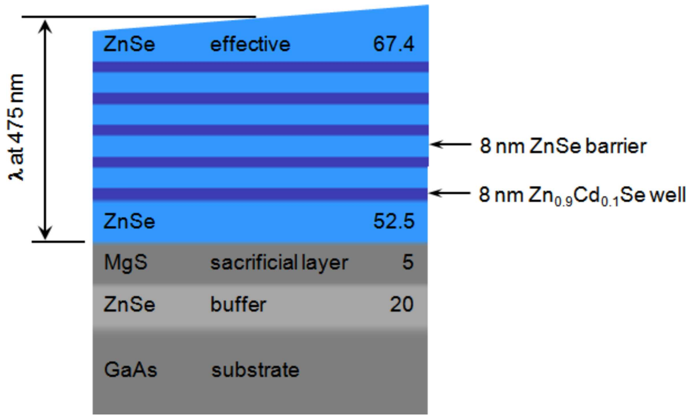

Figure 3.1: Schematic of the molecular beam epitaxy grown heterostructure before processing. Stopping the rotation during the growth of the top epitaxial layer produces a thickness gradient, allowing translational tuning of the completed microcavity. Not to scale. Units are in nm.

on high quality GaAs n^+ substrates following deposition of a 20 nm ZnSe buffer layer. A sacrificial layer of zincblende MgS (5 nm) was grown [42], then the active region, 5 ZnSe(8 nm)/$Zn_{0.9}Cd_{0.1}Se$(8 nm) quantum wells with ZnSe spacers (~ 53 nm) top and bottom such that the physical thickness of the active layer (~ 170 nm) at the centre of the wafer was equal to one optical wavelength at the emission of the quantum well at ~ 475 nm. The effect of 10% Cd in the well on the refractive index is negligible and the entire active layer is treated as bulk ZnSe with refractive index 2.78. A schematic of the heterostructure is presented in figure 3.1.

3.1.1 Sample thickness gradient

Rotation of the sample was stopped during part of the growth of the top ZnSe spacer to allow translational tuning of completed microcavities, calibrated by measuring the thickness gradient of reference samples using broadband reflection spectroscopy. Broadband reflection spectra contain the optical interference pattern produced by the phase difference, $\delta\phi$, between reflected light at a wavelength λ, from the front and back of the epilayer of refractive index, n and thickness, d given by,

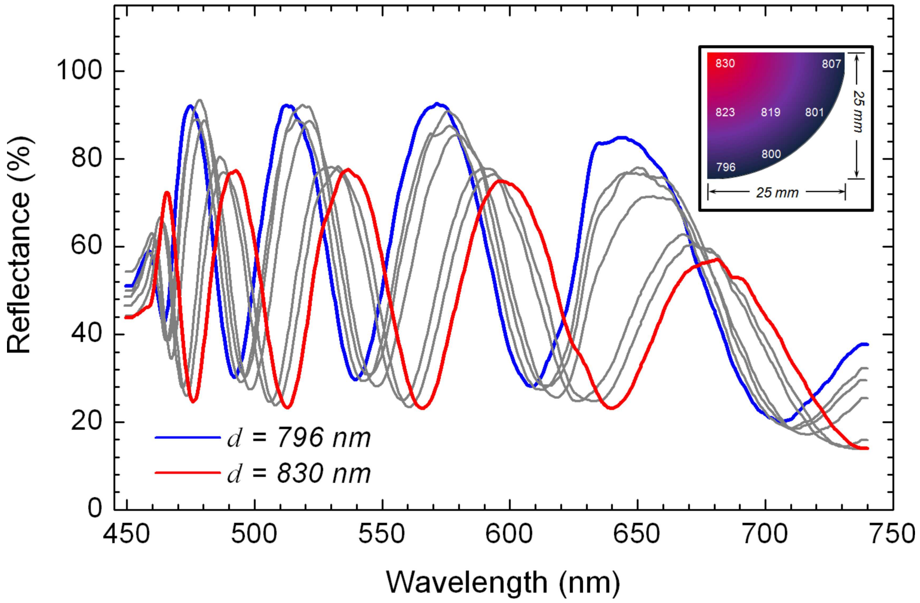

Figure 3.2: Broadband reflection spectra taken at different points across a ZnSe calibration wafer for measuring the gradient produced when the wafer rotation is stopped during growth. Inset: Schematic of the ZnSe wafer. The points where reflection measurements were taken are marked with the numerical value of the deduced epilayer thickness. Units are in nm unless stated otherwise.

$$\delta\phi = \frac{4\pi n d}{\lambda}. \tag{3.1}$$

At any peak in the reflection spectra the phase shift is an integer multiple of π. Taking two adjacent peaks results in two simultaneous equations, $\delta\phi_n$ and $\delta\phi_{n+1}$ which can be solved for d. A thick ($\sim$ μm) epitaxial layer of ZnSe was grown followed by further growth of 50 nm of ZnSe without rotating the wafer in order to measure experimentally the gradient of the epilayer. Figure 3.2 presents a series of broadband reflection spectra taken at room temperature at different points across the ZnSe wafer. The spectral peaks clearly red shift from thin to thicker parts of the wafer. Using (3.1), the thickness at each point on the wafer was deduced. A schematic of the arial view of the wafer, highlighting the points where the light was incident with the deduced epilayer thickness, is presented in figure 3.2 (inset). From this an average translation tuning of ~ 20 meV mm^{-1} was found for completed microcavities.

The overall strain in the active epilayer was kept sufficiently low in order to prevent strain relaxation through the formation of dislocations. It is noted that the zincblende MgS layer is helpful in reducing the overall strain, as its lattice constant, 0.5622 nm [42], is smaller than that of GaAs, 0.5653 nm [37], whereas the ZnSe lattice constant, 0.5668 nm [37], is larger. The in-plane lattice constant of the entire heterostructure is determined by the GaAs substrate. The MgS layer can therefore provide some strain compensation for the subsequent growth of ZnSe.

3.2 II-VI epitaxial liftoff

Epitaxial liftoff technique was originally developed for the III-V material system [43] in response to the limitations of the growth process where high quality single crystal substrates, lattice matched to that of the semiconductor heterostructure are required. This property limits the range of heterostructures that can be grown since a degree of lattice mismatch often present causes the formation of dislocation densities (typically > 10^6 cm^{-2}) resulting in degradation of the devices. By introducing a sacrificial layer below the active epitaxial layer, post growth processing enables a sample to be transferred to a new substrate with the desired properties for device fabrication. The following details the technique of epitaxial liftoff, applied to the II-VI material system.

3.2.1 Sample processing

Small 3×3 mm^2 samples where cleaved from the wafer (3.1), taking considerable care to get perfect cleaves, before coating the surface with a hard wax (Apexion W). A clean cleave is best achieved by lightly ‘tapping’ the top edge of the semiconductor wafer with the tip of a diamond scribe before inverting the wafer and applying a monotonic increase in pressure above the scribed mark. An audible, single click marks a successful cleave. Cleaved samples where then arranged on a glass microscope slide and transferred to a hot plate heated to a temperature of ~ 100 °C. Small pieces of the wax were then placed on top of the samples and left to melt, resulting in domes of wax forming across the sample surface. Further annealing in an oven at 80 °C for 30 minutes ensures that the wax covers the entire surface of the sample (figure 3.3 (a)). This is a similar technique developed for the GaAs material system [43]. Instead of HF, HCl is used with a concentration of 30% for the etch. MgS reacts with HCl to form $MgCl_2$ and H_2S, both of which are water soluble up to high concentrations. Conversely, the other layers in the heterostructure, ZnSe and ZnCdSe, are etched at a much slower rate. The wax coated samples were placed face up in the HCl at room temperature. Typically the epitaxial layer released from the substrate within 30 minutes. As is the case in GaAs based liftoff, the wax coated epitaxial layer floated to the surface, leaving the GaAs substrate behind at the bottom of the glass beaker. The etch rate of the MgS sacrificial layer is estimated to be about 3 mm hr^{-1} (see figure 3.4 (a)). This is considerably larger than the etch rate of AlAs sacrificial layers used in GaAs based liftoff. Using the wax technique, the AlAs etch rate is approximately 0.3 mm hr^{-1} [43], and has been increased to 1 mm hr^{-1} by increasing the etchant temperature [44]. It has been argued that the limiting step in AlAs etching is the solubility of H_2 gas which is one of the reaction products [43]. The etching cannot be accelerated without H_2 gas coming out of the etched channel. In the case of the II-VI liftoff technique, the etch rate is considerably faster and this is in all probability related to the high solubility of the reaction products.

Yablonovitch *et al.* [43] have shown that the etch rate is given by,

$$v_r = \frac{\sqrt{2}Dn}{3\pi N\sqrt{RL_s}}, \tag{3.2}$$

by equating the flux of etchant into the etched channel to the flux of the chemical products moving out of the channel. D and N are, respectively, the diffusion constant and molar concentration of the etchant product. n is the molar concentration of the dissolved sacrificial material. R is the radius of curvature of the epitaxial layer induced by the surface tension of the wax coating. This is a striking result since the etch rate, v_r, decreases with the sacrificial layer thickness, L_s. For the II-VI material system the derivation of the etch rate requires a more complex chemical analysis since the etchant products are highly soluble. In order to probe this issue experimentally, a series of ZnSe/ZnCdSe samples with varying sacrificial layer thickness was grown and their etch rates measured. Figure 3.4 (a) shows the measured etch rate for four wafers with L_s = 2, 5, 20 and 30 nm. Four 3×3 mm^2 samples were prepared from each wafer and the etch time recorded. An inverse trend is clear for $L_s > 2$ nm. In the case of L_s = 2 nm the samples did not lift and it is thought that for $L_s \leq 2$ nm diffusion of the ZnSe in the buffer and in the heterostructure results in zinc rich MgS pillars forming across the sacrificial layer, halting the etch [23].

The epitaxial liftoff technique relies on a large contrast in the etch rates of the sacrificial layer and the epitaxial layer to be lifted. The etch rate of ZnSe in HCl was measured by exposing part of the surface of a bulk ZnSe wafer to the HCl, protecting the other part of the surface with 10 μm strips of photoresist each separated by 10 μm (see figure 3.4 (b) inset). After removing the photoresist, the etched depth was measured with an atomic force micrograph. The topography of the sample is shown in figure 3.4 (b). Even after 3 days in HCl, the ZnSe etch depth was only ~ 10 nm. By comparing the etch rate of the MgS sacrificial layers in the liftoff process, ~ 3 mm hr^{-1} with this measurement, $\sim$ 14 nm hr^{-1} one can conclude that the contrast in etch rates between MgS and ZnSe in 30% HCl is $\geq 10^7$.

After lifting the active layer (figure 3.1), the epitaxial layer was washed in deionised water and transferred to the new functional substrate with a vacuum pen. Details of the new functional substrate are given in section 3.3. By applying a small force ($\sim$ μN $\equiv$

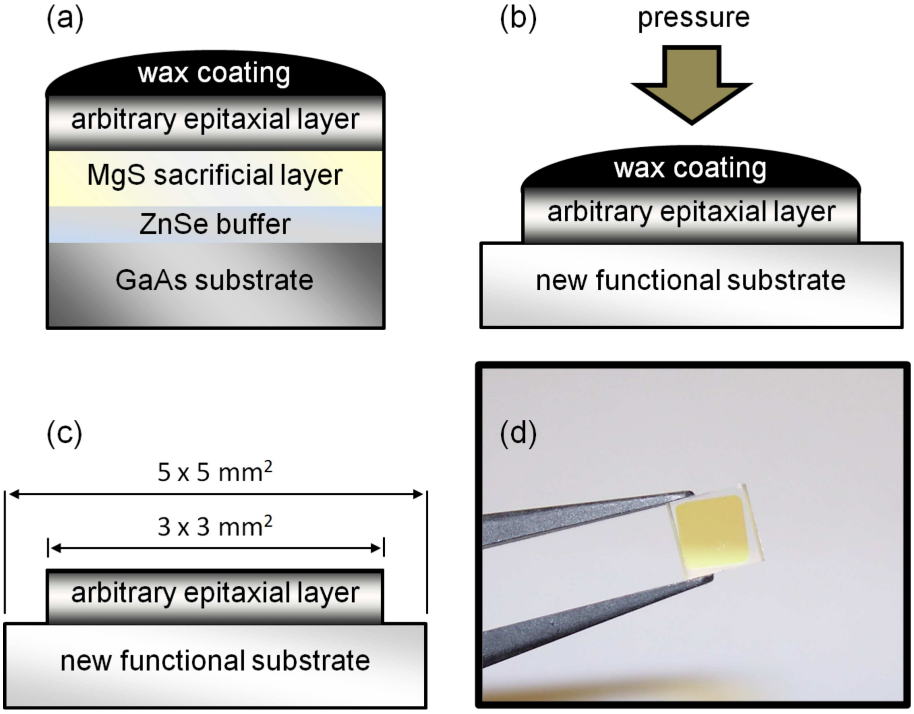

Figure 3.3: (a) 3×3 mm^2 sample coated with a layer of wax. (b) After the liftoff the epilayer is washed in deionised water and transferred to a new substrate. Bonding takes place over a period of 24 hours, with the application of ~ 10 g weight placed on top of the sample. (c) Samples are completed by removing the wax coating with trichlorethylene. (d) Image of a ZnSe epilayer transferred to a fused silica substrate.

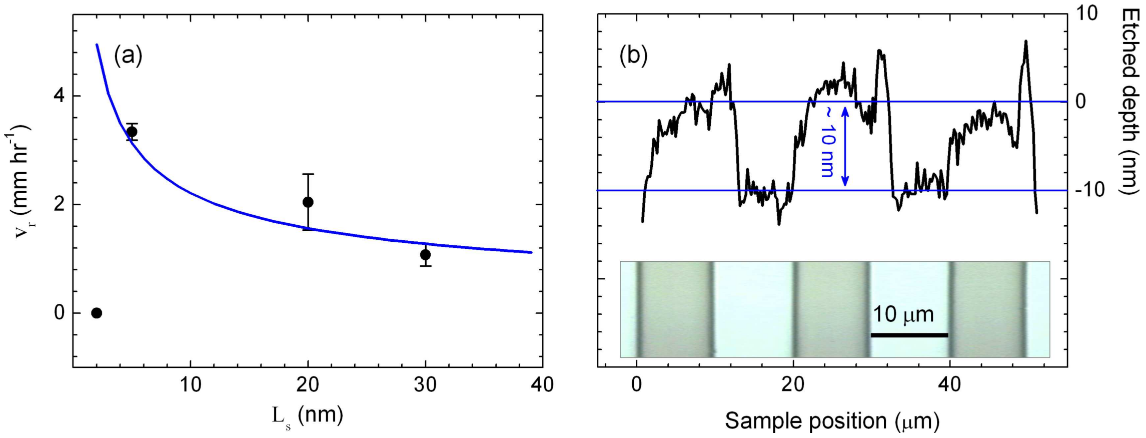

Figure 3.4: (a) Etch rates for a series of samples with varying sacrificial layer thickness, L_s. The solid line represents an inverse square fit, $v_r = \frac{\alpha}{\sqrt{L_s}}$, where the coefficient, α = 7.3. (b) Atomic force micrograph showing the topography of a ZnSe wafer with a grid of photoresist on top, after 3 days submerged in HCl. The selectivity was found to be $\geq 10^7$. Inset: Optical image of the wafer, showing the photoresist grid.

10 g) to the wax coated epilayer it was found that the epitaxial layers strongly bonded to the new substrate (figure 3.3(b)). No adhesive was used. The bonding between epitaxial layer and substrate is most likely through the van der Waals interaction [45]. The surface of the new substrates are optically flat (surface roughness $\sim$ 1 nm as measured by atomic force microscopy). After overnight drying, the wax was removed by dissolving it away in warm trichloroethylene. This left a ~ 170 nm thick epitaxial layer on the new substrate. Figures 3.3(c,d) show, respectively, a schematic and an image of a lifted ZnSe epitaxial layer on a new substrate. The epitaxial layers were crack-free over square millimeter areas.

3.2.2 Post processing characterisation

In order to probe the optical quality of the liftoff layers, photoluminescence spectroscopy was performed on both the original wafer material and on a lifted sample on a fused silica substrate. Photoluminescence was excited by a GaN laser diode emitting at 400 nm. A few hundred μW of power was focussed to a spot size of ~ 10 μm with a $\times 5$ microscope objective. The same objective collected the photoluminescence which was focussed into a grating spectrometer and imaged onto a multi-channel charge-coupled-device camera as detector. Results taken at 80 K are presented in figure 3.5 (a). The wafer material exhibits a strong photoluminescence feature at 2.604 eV, attributed to the heavy hole exciton transition, X_{hh} of the ZnCdSe/ZnSe quantum wells. Figure 3.5 presents also, (a) photoluminescence (offset for clarity) and (b) broadband transmission for the epitaxial layer on the fused silica substrate. The X_{hh} is observed to red shift by 3 meV after liftoff in the photoluminescence. This is a direct result of the strain relaxation in the epitaxial layer after it has been lifted off the GaAs substrate. Luminescence efficiency of the quantum well is not changed within the measurement uncertainty of about 10% by the liftoff procedure [40]. The epitaxial liftoff technique has the additional advantage that transmission experiments can be readily performed on ZnSe based structures. The X_{hh} and X_{lh} transitions are observed at 2.604 and 2.639 eV, respectively, in the transmission spectrum.

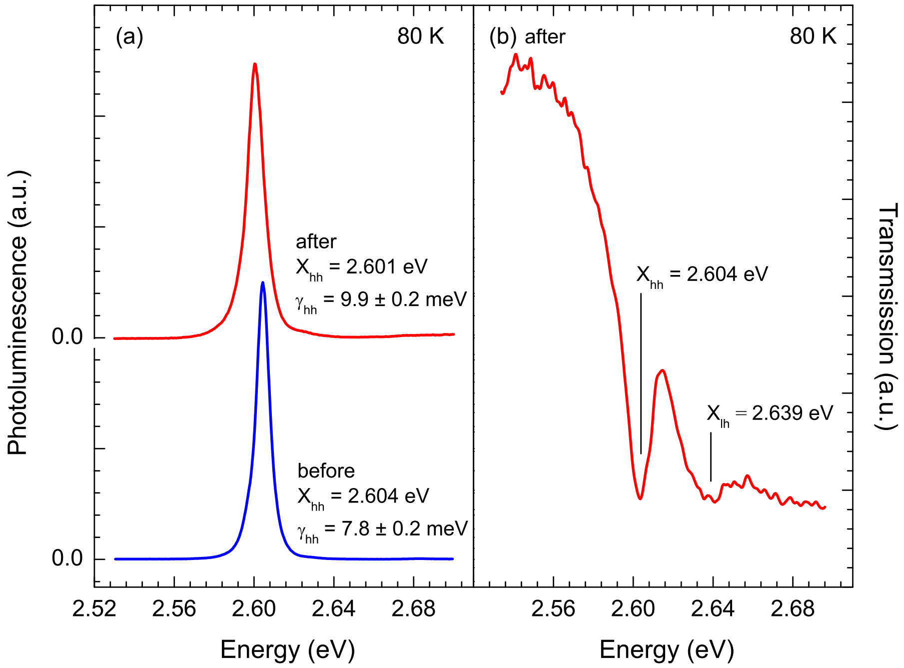

Figure 3.5: (a) Photoluminescence before and after the liftoff process. A red shift of 3 meV is observed due to the relaxation of the material after it has been removed from the GaAs substrate. After the etch the sample was transferred to a fused silica substrate. Spectra are offset for clarity. (b) Broadband transmission of the lifted sample.

It has been suggested that an amorphous interlayer forms between the lifted epilayer and new substrate [45]. This is crucial since further coating of the sample is limited due to the temperature requirements in typical coating techniques. Test samples, lifted and transferred to fused silica substrates, were found to be destroyed when heated to a temperature of ~ 100 °C due to the evaporation of the amorphous layer and/or trapped water droplets. The work presented in chapter 4 details the techniques used to complete the ZnSe based microcavities.

3.3 Designing ZnSe based microcavities

The design of a microcavity must satisfy two key criteria. First, the antinodes of the electric field profile within the microcavity must coincide with the position of the quantum wells. This is done through the design of the heterostructure along with the

	SiO_2/Ta_2O_5
λ_{sb} (nm)	475
n_H	2.15
n_L	1.46
n_c	2.78
τ (fs)	3.60
L_τ (nm)	194

Table 3.1: Calculated values for the reflection delay, τ and apparent length, L_τ for SiO_2/Ta_2O_5 mirrors, along with the refractive indices, n_H and n_L used in (2.15). n_c is the refractive index of the cavity medium and substitutes for n_e in (2.14). The mirror is assumed to be mounted on a glass substrate of index, n_s = 1.5 in a medium of index, n_e = 1.0.

correct choice of the stacking order of the reflector's $\frac{\lambda}{4}$ layers. Secondly, the cavity linewidth, γ_c is closely matched to the linewidth of the quantum well, γ_{hh} satisfying, $(\hbar\Omega)^2 \gg (\gamma_{hh} - \gamma_c)^2$ (see chapter 2). Equation (2.16) gives the linewidth of a planar cavity which is readily customised for a given pair of $\frac{\lambda}{4}$ layers.

The materials used in this work for the mirrors are silicon dioxide (SiO_2), n_L = 1.46 and tantalum oxide (Ta_2O_5), n_H = 2.15 which offer a high refractive index contrast, $\Delta n = 0.69$ and small absorption, $\alpha \simeq 0$ at λ = 475 nm. Other possible materials such as titanium dioxide and zirconium dioxide where ruled out due to their larger absorption coefficients. Table 3.1 shows the calculated values for τ (2.15) and L_τ (2.14) for a SiO_2/Ta_2O_5 mirror. The cavity refractive index, n_c replaces n_e in (2.14). It is noted that τ and L_τ are independent of the number of $\frac{\lambda}{4}$ pairs, N.

Figure 3.6 presents the simulated electric field profiles found along the growth direction of 8 possible microcavities composed of SiO_2/Ta_2O_5 mirrors with a bulk ZnSe cavity. Electric field simulations were performed using commercial software and the ZnSe absorption was set to zero for simplicity. Recall that L (H) designates low (high) refractive index material and that LL (HH) configurations produce n (n + 1) antinodes within the cavity (chapter 2). All HH configurations are given by gH(LH)^7-ZnSe-H(LH)^{7}a structures, and LL as g(HL)^7-ZnSe-(LH)^{7}a structures, where g and a denote, respectively, glass (n = 1.46) and air (n = 1). Refractive indices used in the simulations for SiO_2, Ta_2O_5 and ZnSe are 1.46, 2.15 and 2.78, respectively. Figure 3.6 (a-d) ((e-h)) show the electric field profiles for HH (LL) structures of cavity lengths, 2λ, $\frac{3}{2}\lambda$, λ and $\frac{1}{2}\lambda$, respectively, at λ_{sb} = 475 nm. With either HH or LL configurations the electric field distribution is symmetrical which is not the case for HL or LH configurations where the electric field distribution is asymmetric. HL and LH configurations were not considered. Works have been reported where quantum wells have been incorporated into the mirror [46] but this can only be considered for lattice matched semiconductor mirrors. HH structures are not ideal since the electric field intensity at the location of the quantum wells is comparatively low. For cavity indices, n_c that are higher than the high index mirror material, n_H much of the electric field intensity resides in the mirror-cavity interface and is unavailable to the quantum wells. Figure 3.6 (h) clearly shows that a LL $\frac{1}{2}\lambda$ structure is not suitable since there are no available antinodes within the cavity. The remaining design configurations, figure 3.6 (e-g) are all suitable. However, the ZnSe material system places an extra restriction in that the overall thickness of a ZnSe based heterostructure should not exceed ~ 300 nm so as to avoid dislocations [23]. The physical thickness of the ZnSe cavity in figure 3.6 (e-g) are, respectively, 342, 256 and 171 nm. The structure used in figure 3.6 (g) was chosen so as to be well below dislocation threshold.

Table 3.2 lists the calculated linewidths of the microcavity design of figure 3.6 (g) for $2 \leq N \leq 10$. The refractive indices of the other composite materials used in the calculation of (2.16) are listed in table 3.1.

The mirrors were specifically chosen such that the cavity linewidth, γ_c was optimum for strong coupling with the ZnSe/ZnCdSe quantum wells. The bare exciton linewidth, γ_{hh} = 9.89 meV, as measured by photoluminescence (figure 3.5 (a)). From table 3.2 and figure 3.6 (g) a microcavity fabricated from SiO_2/Ta_2O_5 mirrors with N = 7 results in a cavity linewidth, γ_c = 4.2 meV. In order to compensate for any possible disorder broadening mechanisms of the completed microcavity N = 7 is a suitable choice. This

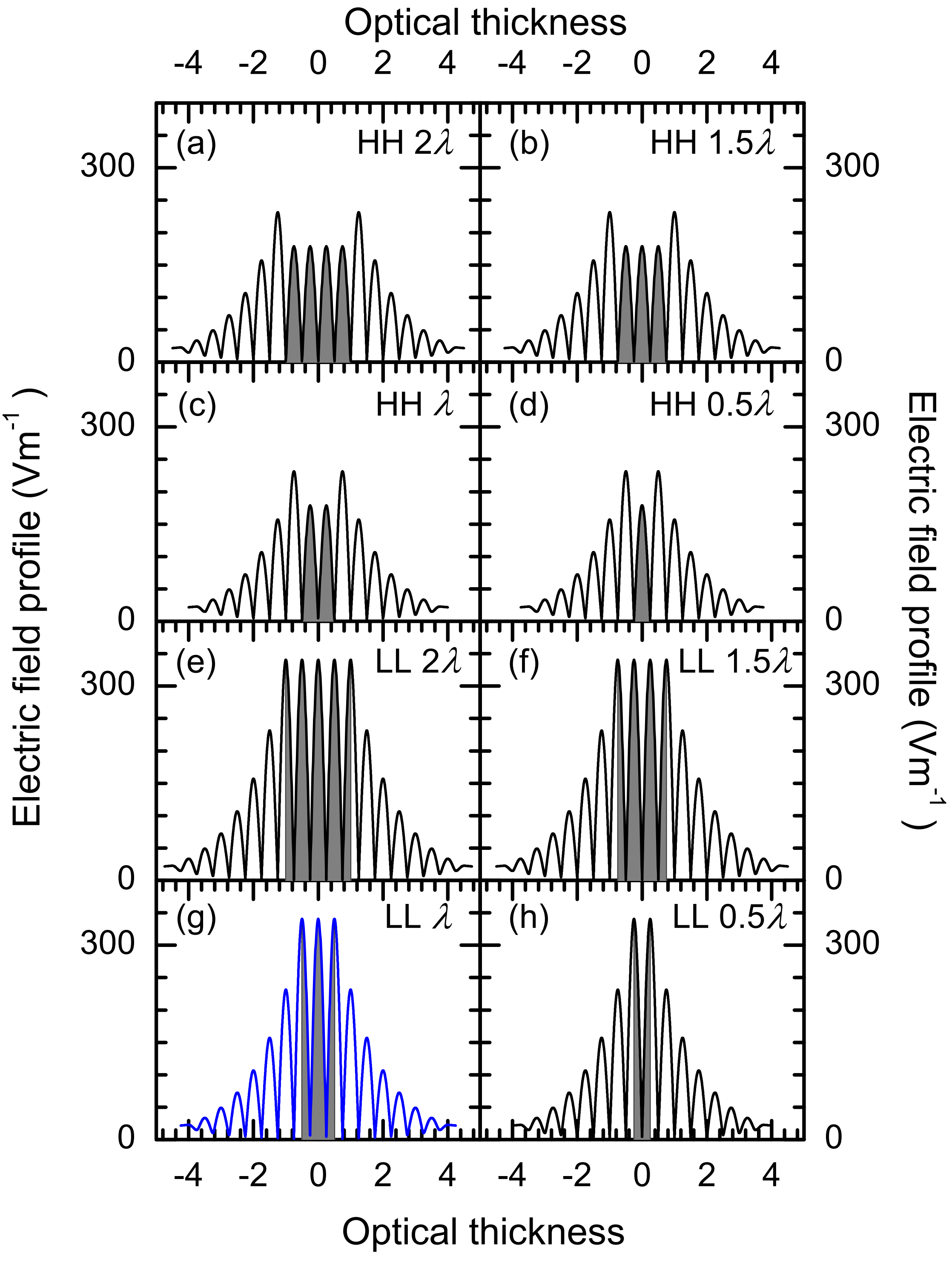

Figure 3.6: Simulated electric field profiles along the growth direction of microcavities with a bulk ZnSe cavity of optical lengths clockwise from top left, 2λ, $\frac{3}{4}\lambda$, λ and $\frac{1}{2}\lambda$. The electric field distribution is shown for HH and LL configuration for each cavity length. All HH configurations are designated by gH(LH)^7-ZnSe-H(LH)^{7}a structures, and LL as g(HL)^7-ZnSe-(LH)^{7}a structures. Refractive indices used in the calculation for SiO$_2$, Ta$_2$O$_5$ and ZnSe are 1.46, 2.15 and 2.78 respectively. Incident radiation of wavelength, λ = 475 nm at 1 W m^{-2}. Absorption has not been considered for simplicity.

N	R	γ_c (nm)	γ_c (meV)
2	0.18	18.9	104.1
3	0.47	12.2	67.3
4	0.71	6.7	37.0
5	0.85	3.4	18.6
6	0.93	1.63	9.0
7	0.97	0.77	4.2
8	0.98	0.36	1.96
9	0.993	0.17	0.91
10	0.997	0.076	0.42

Table 3.2: Calculated cavity linewidths, γ_c composed of N pairs of SiO_2/Ta_2O_5 $\frac{\lambda}{4}$ layers and a ZnSe λ cavity.

gives $\gamma_{hh} - \gamma_c$ = 5.8 meV, which should be sufficient to drive a ZnSe based microcavity into the strong coupling regime. The dielectric mirrors, designed by the author, were deposited onto high optical quality fused silica by Dr. E. Schmidt of Optische Interferenz Bauelemente GmbH. The mirror transmission was measured to be 3.9% at 475 nm with a structure designated by $g(LH)^7La$ and compares well to the simulated value of 3.8%. Figure 3.7 presents the measured broadband transmission at room temperature along with the transfer matrix simulation (2.12) for the dielectric mirror. Deviation of the measured from the calculated spectrum is attributed to extrinsic absorbtion in the coating, especially at short wavelengths.

3.4 Summary

To summarise, the epitaxial liftoff process was discussed in the context of fabrication of ZnSe based microcavities with dielectric mirrors. Previously this was achieved by etching through the back of the GaAs substrate to create a window to allow for deposition of a dielectric mirror. Section 3.3 discussed the design of a ZnSe based microcavity with identical top and bottom dielectric mirrors. The following chapter details the microcavities successfully fabricated based on the techniques and calculations discussed above. The top mirror of each microcavity presented differs and the

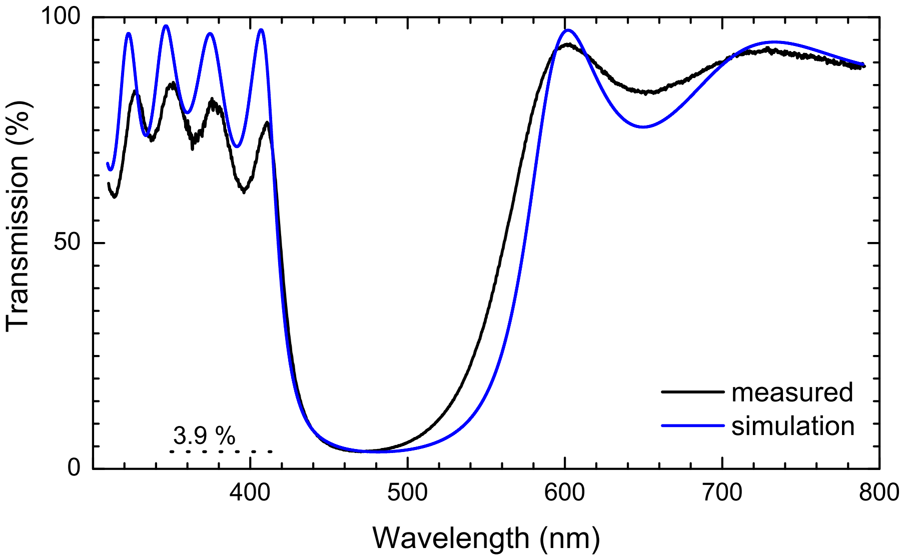

Figure 3.7: Measured and simulated transmission of the dielectric mirrors coated by Optische Interferenz Bauelemente GmbH. The transfer matrix, described in chapter 2, is used to simulate the mirror transmission with a structure g(LH)^{7}La (L:SiO$_2$, n = 1.46, H:Ta$_2$O$_5$, n = 2.1, g:glass, n = 1.46 and a:air, n = 1.0).

techniques and calculations for each is discussed in the relevant sections of chapter 4.

The semiconductor heterostructure and the process of transferring ZnSe/Zn$_{0.9}$Cd$_{0.1}$Se quantum wells was detailed in sections 3.1 and 3.2. Translational tuning of the completed microcavities is possible due to the gradient across the semiconductor wafer. This was measured to be $\sim$ 20 meV mm^{-1} using reflection spectra from a reference sample. The other crucial element to the semiconductor heterostructure is the MgS release layer. The technique allowing ZnSe based epilayers to be transferred to a functional substrate was perfected and characterised. An etch selectivity of 10^7 was achieved confirming that ZnSe based epilayers are unharmed by the epitaxial liftoff technique. Finally, optimum microcavity designs were presented. The design of the dielectric mirrors used to fabricate a variety of ZnSe based microcavities was described in detail, paying attention to the resulting cavity linewidths and the strong coupling criteria, $2\hbar V >\mid \gamma_c - \gamma_X \mid$. A SiO$_2$/Ta$_2O_5$ dielectric cavity of one optical wavelength at the emission of the ZnSe/Zn$_{0.9}$Cd$_{0.1}$Se (~ 475 nm at 77 K) was detailed.

Chapter 4

Three microcavity experiments

This chapter details the successful fabrication of three ZnSe based microcavities and the methods used to experimentally probe them. The first stage in the fabrication process (section 4.1) was common to all the microcavities discussed in this thesis. Due to the temperature sensitivity of the lifted epilayer, further coating of a dielectric mirror was not possible. A variety of solutions to completing the fabrication of three different ZnSe based microcavities is discussed.

4.1 Initial fabrication

The first fabrication step was common to all three of the microcavities presented in this thesis. Following the epitaxial liftoff process the lifted epilayer, supported by the layer of wax, was transferred to a SiO_2/Ta_2O_5 mirror forming half of the microcavity. Binding to the new substrate took place without any adhesive and is discussed in detail in chapter 3. All fabrication steps were carried out in an air filtered environment, reducing the possibility of dust particles becoming trapped within the microcavity.

Common to all the microcavities is the thick fused silica substrates used for the dielectric mirrors. The optical quality of the fused silica substrates is crucial since any disorder will be superimposed onto the optical characteristics of the light-matter interactions. A high degree of optical flatness ($< \frac{\lambda}{10}$ for λ = 475 nm) was determined by examination of the topography using atomic force microscopy. To further ensure quality, the substrates were optically probed by viewing the beam profile of laser light, coupled to a single mode optical fibre, after being focused and reflected off the back of an uncoated substrate. Figure 4.1 (a). The bottom interface of the substrate was positioned at the focal plane of a $\times$ 10 microscope objective which was illuminated by a single mode fibre coupled laser emitting at a wavelength of 474 nm. The reflected light was collected and collimated by the same objective. The collimated light was detected by a coupled charged device, the image of which is presented in figure 4.1 (b). The Airy-like diffraction pattern generated from the effective circular aperture of the single mode fibre is clearly undistorted by the confocal setup or the substrate. To confirm this was the case across the visible spectrum, a second laser, emitting at a wavelength of 633 nm was focussed with the same lens and imaged as before (figure 4.1 (c)). As expected the shorter wavelength produces a greater density of maxima in the diffraction pattern. The clarity of the beam profiles, produced by circular diffraction from the single mode fibre coupled lasers shows that the spatial information is not distorted by either the objective lens, the beam splitter or the fused silica substrate in the spectral region of $475 \rightarrow 633$ nm. The spectral work presented in this thesis is within $450 \rightarrow 500$ nm.

4.2 Fixed microcavity

To fabricate the first microcavity presented in this thesis, a second dielectric mirror, identical to the first, was mechanically held against the active layer forming the fixed microcavity. From figure 3.7 the stopband of the composite mirrors was found to be ~ 180 nm. This allows an upper limit to be placed on the cavity length since during the experiments presented in chapter 5 only a single transmission mode was ever observed within the stopband, evidencing the free spectral range to be ≥ 180 nm. From $L_{cav} + 2L_{\tau}$ = $\frac{1}{2\Delta(1/\lambda)}$, where L_c and $2L_{\tau}$ = 388 nm (see table 3.1) are the physical cavity length and the apparent depth introduced by the dielectric mirrors, respectively, an upper limit on the cavity length can be deduced. $\Delta(1/\lambda)$ is the change in wave number. The upper limit on the physical cavity length is found to be ≤ 312 nm. This

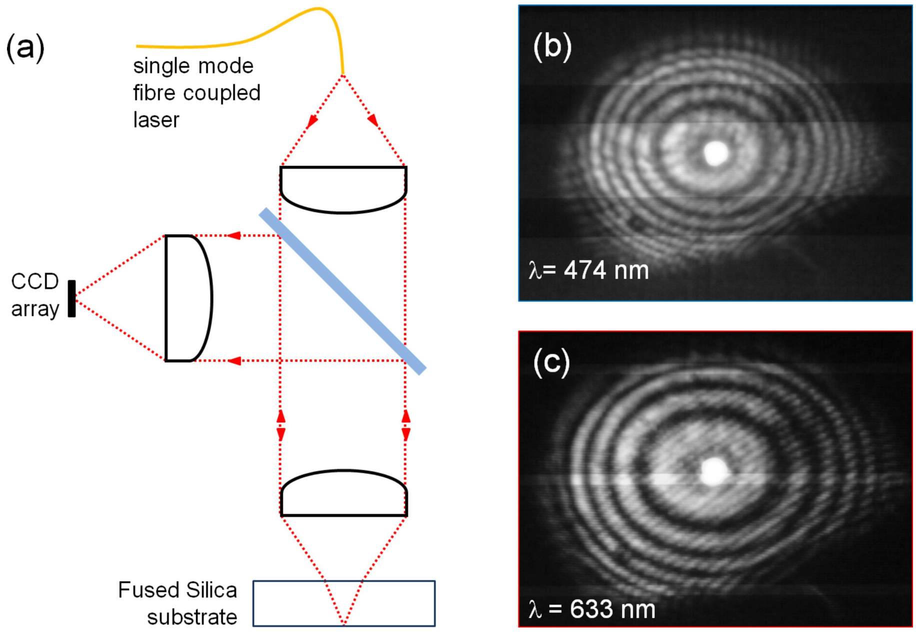

Figure 4.1: (a) Experimental setup used to probe the optical quality of the fused silica substrates. Beam profiles from two fibre coupled lasers after being focused and reflected off the back of an uncoated fused silica substrate are presented on the right. Laser light at a wavelength of 474 nm and (b) 633 nm.

indicates that the achieved cavity length is one optical wavelength at the emission of the quantum well, $L_{cav} \sim 170$ nm and refractive index n_c = 2.78. It is noted that only physical cavity lengths of integer wavelengths at the emission of the quantum well are possible due to positioning requirements of the electric field, discussed in chapter 3. The transmission of the mirrors used was measured, via broad band transmission at room temperature, to be 3.8%. Assuming negligible absorption, the reflectivity for the mirrors is 96.2%. Figure 4.2 presents a schematic of the completed fixed microcavity. The samples were sandwiched between two identical brass plates, designed such that optical access to the sample was not obstructed.

4.2.1 Spectroscopic techniques

Completed microcavities were transferred to a continuous flow cryostat and characterised by measuring broadband transmission and photoluminescence. Figure 4.4

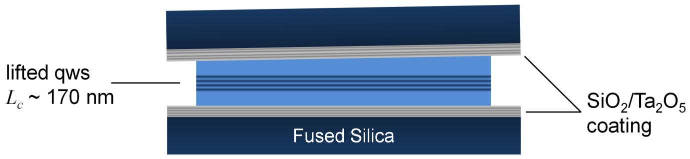

Figure 4.2: Schematic of the fixed microcavity. After transferring the epilayer to a dielectric mirror, a second mirror, identical to the bottom mirror, was placed on top of the epilayer and mechanically fixed in place. The cavity length was found to be ~ 170 nm, with a refractive index, n_c = 2.78. The transmission of the mirrors used was measured to be 3.8% (96.2% reflectivity, assuming zero absorbtion).

shows the experimental setup built and used for transmission and photoluminescence spectroscopy. For the purpose of measuring the polariton dispersion, angle resolved transmission spectroscopy is ideal. White light continuum (WLC) is an ideal broadband coherent source for the technique used here. The WLC was generated by focusing ~ 2 μJ of laser light from a regenerative amplifier emitting ~ 200 fs pulses at λ = 800 nm and a repetition rate of 1 kHz , into a cuvette of deionized water. The generation of WLC by the propagation of high power ultrashort laser pulses in transparent nonlinear media is a well known phenomenon [47]. When a strong electromagnetic pulse produced by a laser travels through a nonlinear medium, it induces an appreciable intensity dependent refractive index, imposing a phase modulation on the electromagnetic pulse, a phenomenon known as self-phase modulation. The refractive index intensity dependence n_2 induces a frequency change of $\Delta\omega = -\frac{\omega n_2}{c}\frac{dI(z,t)}{dt}z$ for $n_2 > 0$. The self-phase modulation of the electromagnetic pulse results in the leading (negative intensity gradient) and trailing (positive intensity gradient) edges being lowered and increased in frequency, respectively. The result is that the quasi-monochromatic laser pulse is spectral stretched to produce a broadband source.

The output of the regenerative amplifier was only quasi-Gaussian and due to the mechanisms of continuum generation the profile of the WLC closely follows that of the laser used to generate it. To improve the profile of the regenerative amplifier output a spatial filter was assembled. The laser light was focused into a high vacuum chamber containing a 100 μm pin hole with quartz entry and exit windows. The beam profile of

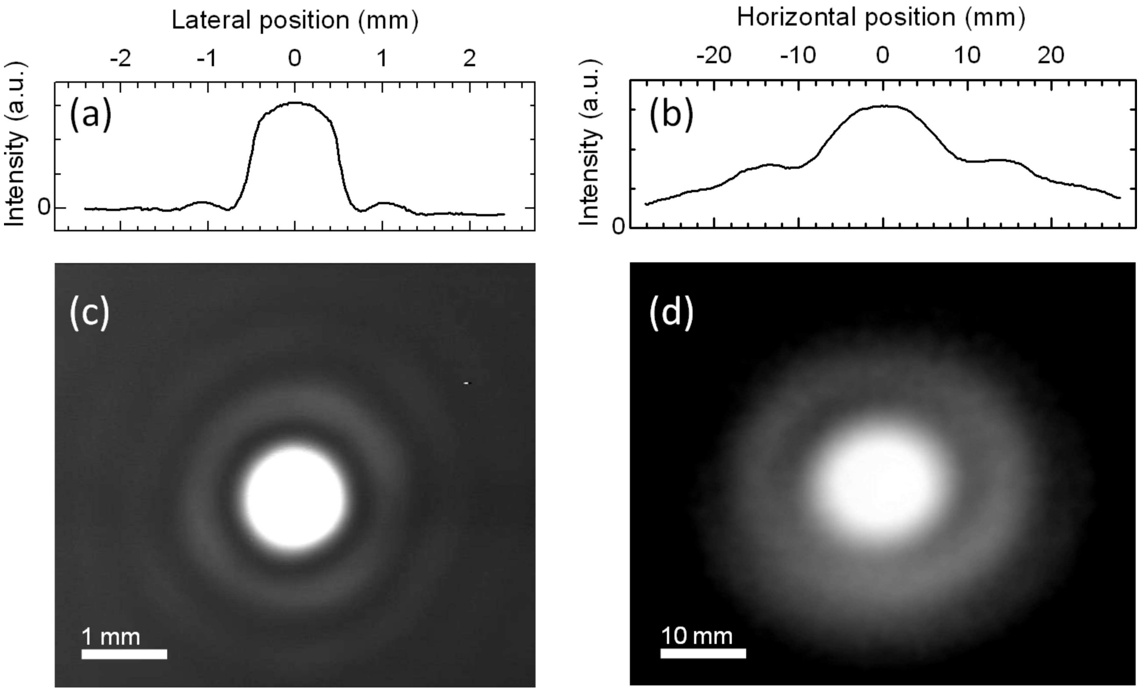

Figure 4.3: (a) Intensity profile across the centre of the regenerative amplifier beam after a 100 μm pinhole spatial filter. (b) Beam profile of the regenerative amplifier after a 100 μm pinhole spatial filter. (c) Intensity profile of the generated white light continuum collimated to a beam diameter of ~ 25 mm and (b) the full beam profile.

the regenerative amplifier, after passing through a 100 μm spatial filter, is presented in figure 4.3 (a - b) along with the generated WLC, figure 4.3 (c - d). Figure 4.4 shows a schematic of the entire experiment, where the spatial filter and WLC components are clearly labeled. The generation of WLC is highly dependent on the regenerative amplifier intensity. For daily adjustment, a variable neutral density filter was positioned after the spatial filter followed by a variable aperture so that the central, Gaussian-like profile of the regenerative amplifier was used to generate the WLC. Following the generation of the white light the broadband source was collimated to a beam diameter of ~ 24 mm and any residual laser light filtered out with an infra red short pass filter. Figure 4.3 (c) and (d) show the beam profile of the generated WLC.

Two identical lenses, with their numerical aperture matched to the cryostat, were used to focus and collect light at the sample. Fully illuminating the objective lens, white light was focused to a spot size of ~ 20 μm at the sample and transmitted light was col-

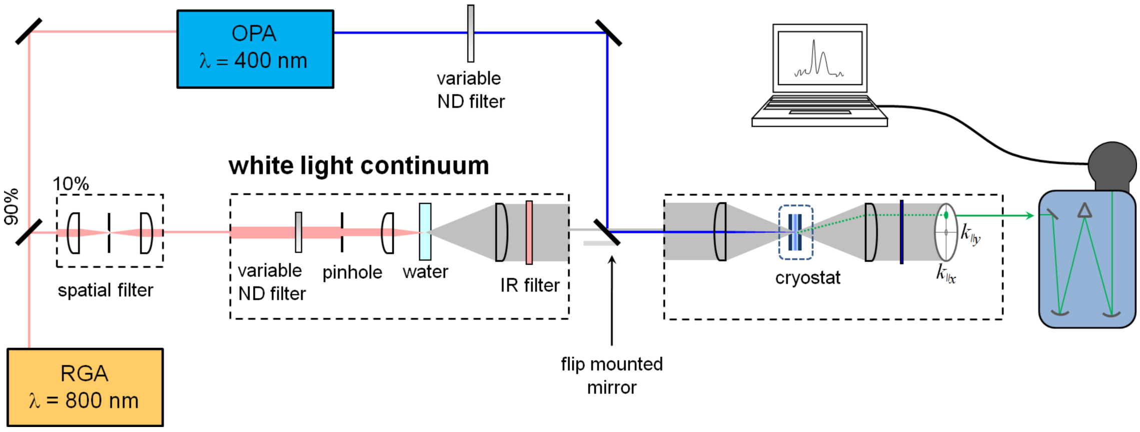

Figure 4.4: Experimental setup for angle resolved broadband transmission spectroscopy. White light is focused and collected at the sample by two identical lenses, NA matched to the cryostat. A 500 μm fibre bundle was used to scan through the transmitted light and dispersed and imaged with a spectrometer and charged coupled device as detector.

limated back to a diameter of 24 mm. The cross sectional profile of the collimated transmission corresponds to a range of angles of incidence. A fibre coupled spectrometer was used to scan through the collimated light and thus record a series of angle resolved transmission spectra. A 500 μm fibre bundle was used to collect the transmitted optical information with an angular spread of $\pm 0.35°$. In this way lateral displacement of the fibre is related to angle of incidence at the microcavity. Taking into account the glass substrate of the mirrors, the range of angle of incidence at the microcavity surface was $\pm 6° \pm 0.35°$. Each spectrum was taken at different points through the centre of the collimated beam with increments of 1 mm. Since the in-plane wavevector inside the cavity, $k_{||}$ is related to the angle of incidence, θ by $k_{||} = \frac{\omega_c}{c} sin(\theta)$ the dispersion of the microcavity can be measured in k-space between $\pm 1.39 \pm 0.08 \times 10^6$ m^{-1}.

For photoluminescence experiments laser light from the 4th harmonic of an optical parametric amplifier emitting at a wavelength of 400 nm (3.1 eV) was focused at the sample to a spot size of ~ 10 μm using the same objective as before. It is noted that excitation of the microcavity with a laser at 3.1 eV injects an e-h gas and the angle of incidence is ‘lost’ during the phonon cooling of the e-h gas, whereas the angle of emission contains the momentum information of the emitting state. A variable neutral density filter was used to attenuate the average excitation energy from a maximum of 180 mJ cm^{-2} (~ 200 fs pulses with 10 μJ of energy and a rep rate of 1 kHz). Note that the excitation energy stated here is an estimate of the average energy actually entering and exciting the semiconductor sample, after losses from optical elements and the microcavity DBR. Angle resolved photoluminescence was collected with the same procedure as for transmission spectroscopy.

To measure the uncoupled linewidth of the cavity photon, γ_c the microcavity was red shifted so that the energy of the cavity photon was ~ 150 meV below the X$_{hh}$ transition (E$_c <$ E$_{X_{hh}}$ = 2.604 eV). Fitting a Lorentzian to the white light transmission spectrum (figure 4.5 top), γ_c was found to be 15.5 ± 0.3 meV. This is a factor of 4 greater compared to the theoretical value of 4.2 meV which is attributed to disorder effects and anti-parallelism of the two mirrors. The uncoupled exciton was measured to be E$_{X_{hh}}$ = 2.608 eV with γ_{hh} = 10.1 ± 0.2 meV from photoluminescence spectra taken from the same point on the detuned microcavity (figure 4.5 bottom). The 7 meV blue shift of the heavy hole exciton from photoluminescence at 80 K (figure 3.5 (a)) to 20 K is as expected due to the decrease in the materials band gap, which in turn is a result of a decrease in electron-phonon interactions at lower temperatures [48]. The measured linewidth for the completed microcavity is broader than expected: Measurements on the bare quantum well epilayer, transferred to a fused silica substrate, figure 3.5 (a), resulted in a linewidth of 9.9 ± 0.2 meV. The broadening of the linewidth by 0.3 meV is perhaps due to small fluctuations in the mechanical strain induced by the clamp, holding the fixed microcavity together.

The resultant Q of the cavity was modest, ~ 170 which is suitably matched to the effective $Q \sim 260$ of the quantum wells. High Q is desirable for enhancing the coupling of the exciton and cavity photon ($\frac{Q}{\sqrt{V}}$) but care must be taken to ensure that the coupling is within the strong coupling regime and this is achieved in the limit $(\gamma_{hh} - \gamma_c)^2 \rightarrow 0$.

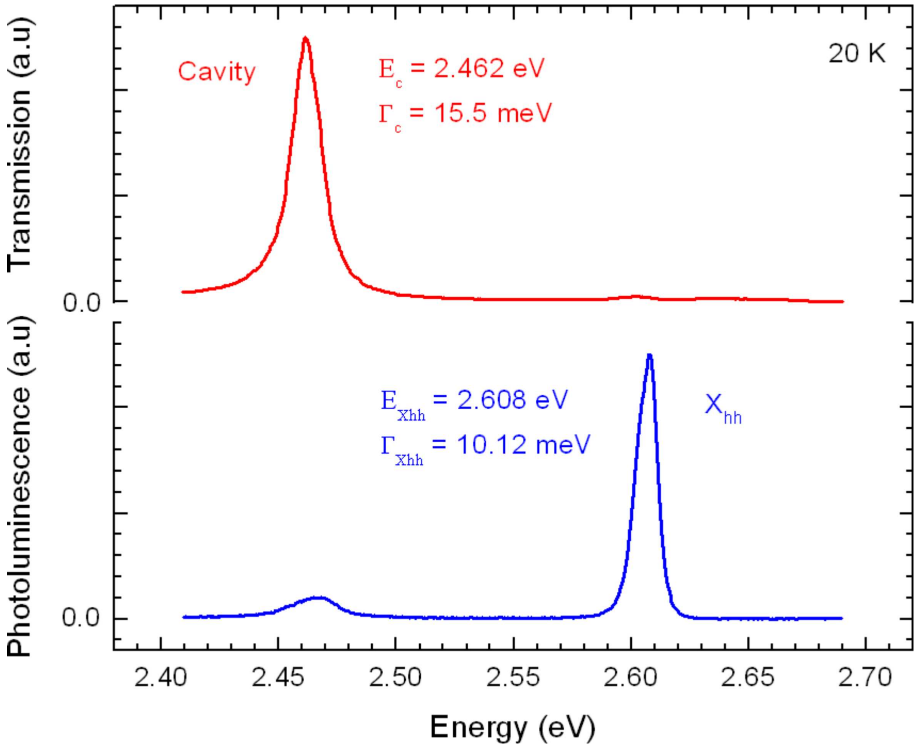

Figure 4.5: Uncoupled cavity transmission (top) and quantum well photoluminescence (bottom) for the fixed microcavity. The microcavity was detuned by ~ 150 meV. Fitting Lorentzian curves to the spectra γ_c was found to be 15.5 ± 0.3 meV and γ_{hh} = 10.1 ± 0.2 meV.

An increase in the mirror reflectivity would readily result in a much higher cavity Q but would equally drive the microcavity into the weak coupling regime, where it would be more suitable, for example, for Purcell factor experiments.

Figure 4.6 presents the transmission of the fixed microcavity, tuned to resonance (E_c = E_{hh}) at normal incidence, achieved by selecting the appropriate spot on the microcavity. The sample was cooled to 80 K. Two spectral peaks are clearly resolved at 2.594 eV and 2.618 eV on either side of the uncoupled heavy hole exciton transition (E$_{Xhh}$ = 2.604 eV measured from transmission spectrum at 80 K, figure 3.5 (b)). Following the standard nomenclature [49], the lower energy peak corresponds to the lower cavity polariton, the higher energy peak to the upper cavity polariton. The measured spectral splitting is, $\hbar\Omega$ = 24 meV. From the measured linewidths of the uncoupled cavity mode and quantum wells (figure 4.5), $(\gamma_{hh} - \gamma_c)^2 \sim 29$ meV^2 $\ll$ $(\hbar\Omega)^2$ = 576 meV^2, clearly well within the strong coupling regime.

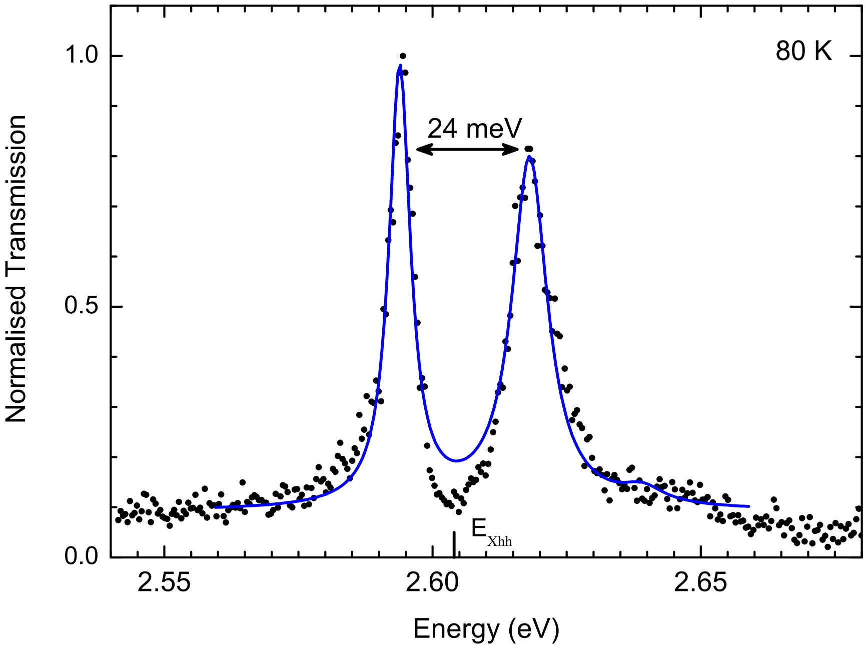

Figure 4.6: White light transmission of the fixed microcavity translated to resonance at normal incidence. Two spectral peaks are clearly resolved at 2.594 eV and 2.618 eV on either side of the heavy hole exciton transition (E_{hh} = 2.604 eV measured from transmission of a bare sample, figure 3.5 (b)). The solid line is a Lorentzian fit as guide to the eye and was used to measure the normal mode splitting which was found to be 24 meV. Fit parameters used for the Lorentzian curve for the lower (upper) peak are 4.7 (8.1) meV for the full width at half maximum and 0.7 (1) for the normalised integrated area.

Further discussion of the fixed microcavity operating in the strong coupling regime is presented in chapter 5. As will be discussed, the fixed microcavity was a successful device in which the cavity polariton was studied, clearly evidencing the high degree of quality achievable with the fabrication technique discussed above. However, to ensure a high degree of quality, the fabrication process was very intensive, with each stage having to be carried out with great care so as to minimise defects such as cracks in the epilayer and dust particles becoming trapped within the microcavity. Trapped dust particles in the fixed microcavity was a significant problem since a single micrometer particle would render the entire sample useless and it was necessary to repeat the fabrication many times before a successful device was realised. The issue of dust can be greatly improved by coating the second mirror directly onto the epilayer. Attempts were made to coat the semiconductor wafer with a dielectric coating before the liftoff process, however, due to the inherently poor adhesion between ZnSe and $\mathrm{SiO_2}$ the tension required for the liftoff technique resulted in the coating peeling away from the wafer, leaving the epilayer still attached to the GaAs substrate. The other method investigated was to coat the sample after the epilayer had been transferred to the first dielectric mirror. It was found that this was not possible for a dielectric coating due to the elevated temperatures required for standard coating techniques. Test samples were transferred to a fused silica substrate and gradually heated to a temperature of $100\ ^\circ$C in an oxygen free environment. The sample was viewed under a $\times\ 10$ optical microscope during the heating process. The observation was that for temperatures above $\sim 80\ ^\circ$ sudden cracks and peeling appeared across the epilayer. Following from the work of Yabonovitvh *et al.* [45], the temperature sensitivity of the lifted samples was attributed to an amorphous interlayer formed between the lifted epilayer and its new substrate during the bonding process. With this in mind the samples were coated at room temperature using resistive thermal evaporation and magnetron sputtering, as discussed in detail in the following section.

4.3 Monolithic hybrid microcavity

The second microcavity presented is a metal-dielectric hybrid microcavity. A monolithic device offers the advantage of reduced cavity mode volumes since the top mirror is coated directly on the sample and any trapped dust particles will only increase the cavity length in the region of the particle and not across the entire device, as is the case for the fixed microcavity. After bonding the epilayer to the dielectric mirror, the sample was transferred to a high vacuum resistive thermal evaporation and magnetron sputtering chamber where the microcavity was coated with the sample close to room temperature. Reflectivity of $> 90\%$ is readily achievable with Ag coatings whilst still allowing for optical communication through the layer. It will be shown below that the optimum thickness of Ag would result in a theoretical cavity linewidth of $\sim$

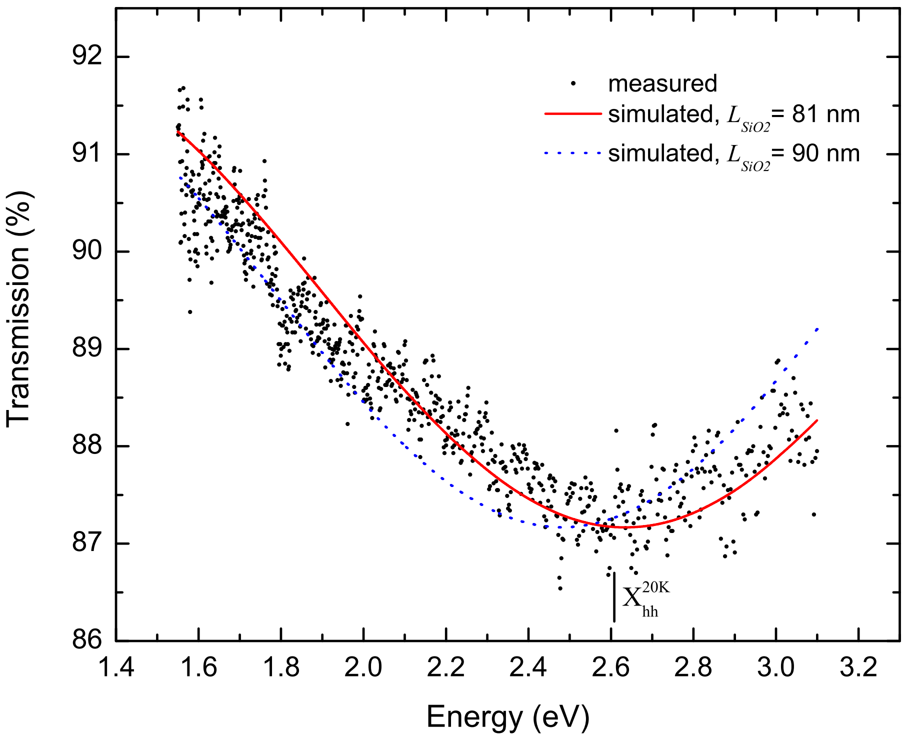

Figure 4.7: Broadband transmission of a reference sample, coated along with the microcavity. The reference sample was prepared with a $\frac{\lambda}{4}$ MgF$_2$ layer so as to give a contrast in refractive index between the fused silica substrate and the SiO$_2$ coating. A transfer matrix simulation (solid line) confirms a SiO$_2$ thickness of 81 nm, a $\frac{\lambda}{4}$ layer at 475 nm for refractive index, n = 1.46. A second simulation was performed for a SiO$_2$ thickness of 90 nm (dotted line). The measured transition of the heavy hole exciton is marked.

7 meV. Applying the strong coupling criteria, $(\gamma_{hh} - \gamma_c)^2 \sim 7$ meV^2 $\ll (\hbar\Omega)^2$ = 576 meV^2. It is therefore expected that a metal-dielectric hybrid microcavity will operate in the strong coupling regime. It was found however that the completed microcavities did not evidence strong coupling. This was due to the quantum well excitons being energetically out of reach of the cavity dispersion which was attributed to the physical length of cavity being too short or too long. For this reason, the coated microcavity was probed at various temperatures so as to shift the exciton energy to within reach of the cavity photon. It was found that at room temperature the heavy hole exciton and cavity photon could be tuned into resonance and the sample exhibited weak coupling phenomena indicated by the lasing like behaviour. A full discussion of the experimental observation is given in chapter 6. Several coated samples were prepared as described below.

The use of a metallic coating introduces a π phase shift to the internal electric field of the completed microcavity, a consequence of the complex refractive index of metals. To compensate for this a $\frac{\lambda}{4}$ layer was required to introduce a second π phase shift. A $\frac{\lambda}{4}$ of SiO_2 at λ = 475 nm was deposited onto the epilayer before the Ag. This ensures that the electric field antinode is located at the quantum wells in the centre of the λ cavity. The $\frac{\lambda}{4}$ layer was coated by magnetron sputtering of a SiO_2 target with a purity of 99.99% whilst the thickness was optically monitored. The SiO_2 and metallic layers were coated by the author, facilities courtesy of the Fibre Optics Group, Heriot-Watt University. An *in-situ* optical monitoring system was designed, assembled and perfected. It is noted that achieving an optical thickness (physical thickness scaled by refractive index) of $\frac{\lambda}{4}$ is more important than achieving a target physical thickness. The advantage of optical monitoring over other methods such as crystal quartz sensors is that the measured optical thickness is independent on the optical properties of the material (i.e. refractive index).

A single mode, 2 × 2 fibre coupler, with one optical fibre fed into the chamber, was used. A solid state laser emitting at λ = 474 nm was coupled to one of the external fibres. The back reflection of the laser light off the facet of the chamber based fibre was monitored at the second external fibre. In this way any material coated onto the facet of the chamber based fibre, with sufficiently contrasting refractive index will alter the intensity of reflected laser light and this can be related to the thickness of the coated layer through a transfer matrix simulation (2.12). It is noted that the refractive index of SiO_2 is 1.46 which is close to the refractive index of the optical fibre used. It was therefore necessary to coat the facet of the chamber based fibre with a material with a significantly different value for refractive index. Ensuring a clean cleave by monitoring the back reflection, the facet of the chamber based fibre was coated with $\leq$ 3 nm of Ag with refractive index of 0.05 at λ = 475 nm. Following the preparation of the chamber based fibre, fused silica reference samples were prepared with a thermally evaporated $\frac{\lambda}{4}$ layer of MgF_2, monitored with the Ag coated fibre. The microcavity,

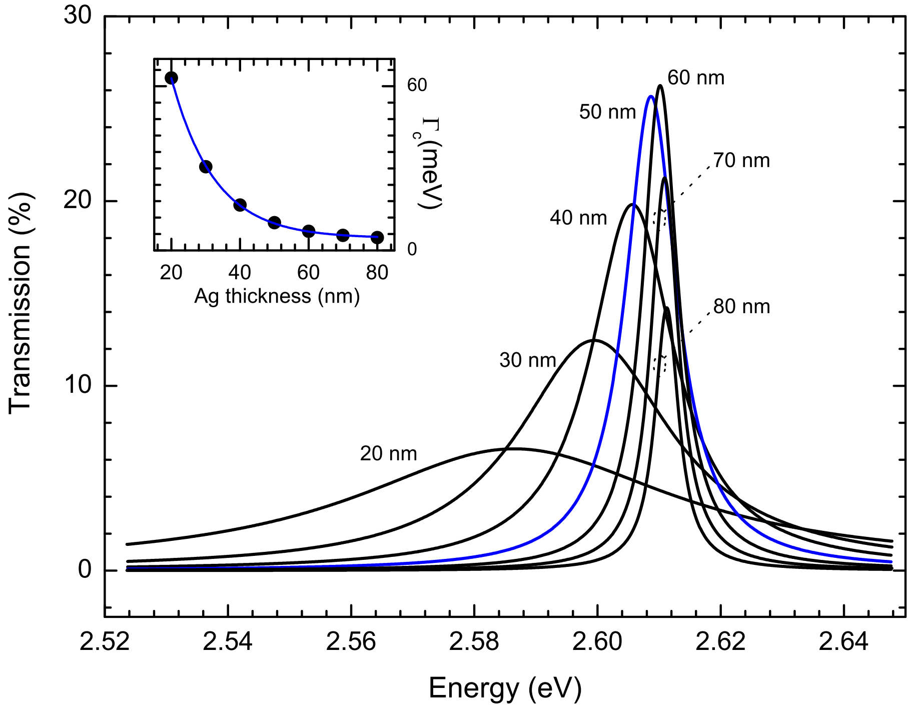

Figure 4.8: Transfer matrix simulations of the completed microcavity with a 170 nm ZnSe cavity and a range of Ag coatings. The lowest energy transmission peak corresponds to a microcavity completed with 20 nm of Ag. The Ag layer thickness is increased in increments of 10 nm until the highest energy transmission peaks corresponding to 80 nm of Ag. The blue spectrum highlights the choice of Ag layer thickness. (inset) Resulting cavity linewidth for the different coating thicknesses.

along with the reference sample was then coated with a $\frac{\lambda}{4}$ layer of SiO$_2$ at λ = 475 nm. The room temperature, broadband transmission spectrum of the fused silica reference sample with the $\frac{\lambda}{4}$MgF$_2$/$\frac{\lambda}{4}$SiO$_2$ coating is presented in figure 4.7. The dip in the transmission (determined by the optical thickness of the coating) occurs at 2.604 eV, the energy of the heavy hole exciton at 80 K (figure 3.5 (b)). The measured transmission (dots) is in good agreement with a transfer matrix simulation (solid line), confirming a SiO$_2$ thickness of 81 nm ($\frac{\lambda}{4}$ layer at 475 nm for refractive index, n = 1.46). A second simulation (dotted line) was performed for a SiO$_2$ thickness of 90 nm and clearly results in an unsatisfactory fit. It is estimated that the accuracy of the optical monitoring system was $\sim \pm 3$ nm.

Finally the microcavities were completed with the resistive thermal evaporation of a Ag

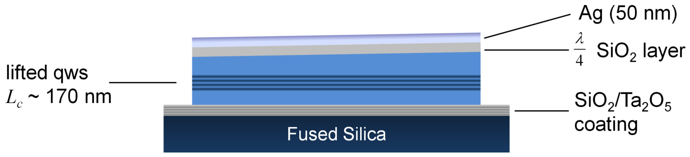

Figure 4.9: Schematic of the monolithic microcavity completed with a $\frac{\lambda}{4}$ layer of SiO$_2$ at λ = 475 nm and 50 nm of silver.

layer. Recall that the effective Q of the quantum wells was found to be $Q \sim 280$. Figure 4.7 (b) shows simulated transmission spectra of the monolithic hybrid microcavity with varying thickness of Ag. The lowest energy peak corresponds to a Ag layer of 20 nm. Moving up in energy the 30 nm spectrum is presented until the highest energy peak, that corresponds to the a Ag layer of 80 nm. It is clear that for a Ag coating thinner than 50 nm (blue spectrum), the optical confinement is poor, whilst at thicker layers the high absorption coefficient of the Ag limits the ability of the microcavity to ‘communicate’ with the outside world. A Ag coating of 50 nm is optimum and by determining the spectral linewidth from figure 4.8 (γ_c = 7.4 meV), the theoretical cavity Q is found to be 346. The 50 nm Ag layer was thermally evaporated and monitored using an acoustic quartz monitor. The quartz oscillates at a resonance frequency that is dependent on the thickness and atomic mass of the Ag film deposited onto it and this is relayed to a calibrated piezoelectric crystal. Quartz monitors are capable of 0.5% accuracy, but this is dependent on the position of the device in the chamber and the age of device. An accuracy of $\sim \pm 2$ nm was estimated.

Figure 4.9 shows a schematic of the completed microcavity with a 50 nm Ag coating. Experimental probing of the microcavity is presented is chapter 6. The experimental setup used was the same as for the fixed microcavity, figure 4.4. As will be discussed, the monolithic microcavity operated in the weak coupling regime at room temperature, exhibiting traditional lasing mechanisms, the first realisation of a ZnSe based hybrid microcavity lasing at room temperature. As with the fixed microcavity the monolithic device required intense processing. It was unfortunate that all of the monolithic devices fabricated did not exhibit strong light matter coupling. This was attributed to the inherent difficulty in matching, energetically, the quantum wells to the cavity photon. The following section will discuss an entirely different type of microcavity where the second mirror is completely external to the rest of the microcavity. This greatly improved the fabrication success rate since the cavity photon could be energetically tuned over a much larger range than the range of tuning for either the fixed or monolithic microcavities.

4.4 Length tunable microcavity

The third microcavity featured in this work is a completely length tunable microcavity. In contrast to the microcavities discussed so far, the tunable microcavity was composed of two separated components, the top and bottom mirrors separated by the epilayer and an air gap. The epilayer was deposited onto the bottom mirror. The advantage of the tunable microcavity was the freedom in which the cavity energy could be tuned by displacement of one of the mirrors relative to the other. Based on the experience from the previous microcavities (lower cavity Q than predicted due to disorder), the reflectivity of the mirror used to fabricate the tunable microcavity was increased to 98%. For a reflectivity of 98% the theoretical linewidth, equation (2.16)) is calculated to be 2.0 meV for a cavity with a λ ZnSe layer and a 2 λ air gap. From the measured exciton linewidth at 80 K (figure 4.13 (c)) and an expected spectral splitting of the cavity polaritons of 24 meV, the strong coupling criteria is $(\gamma_{hh} - \gamma_c)^2 \sim 22$ meV^2 $\ll (\hbar\Omega)^2$ = 576 meV^2, clearly still within the strong coupling regime. The new dielectric mirrors, designed by the author, were deposited onto high optical quality fused silica by Dr. E. Schmidt of Optische Interferenz Bauelemente GmbH. The mirror transmission was measured to be 1.9% at 475 nm with a structure designated by $g(HL)^8a$. Figure 4.10 presents the measured broadband transmission at room temperature. The calculated value of the transmission at the design wavelength was

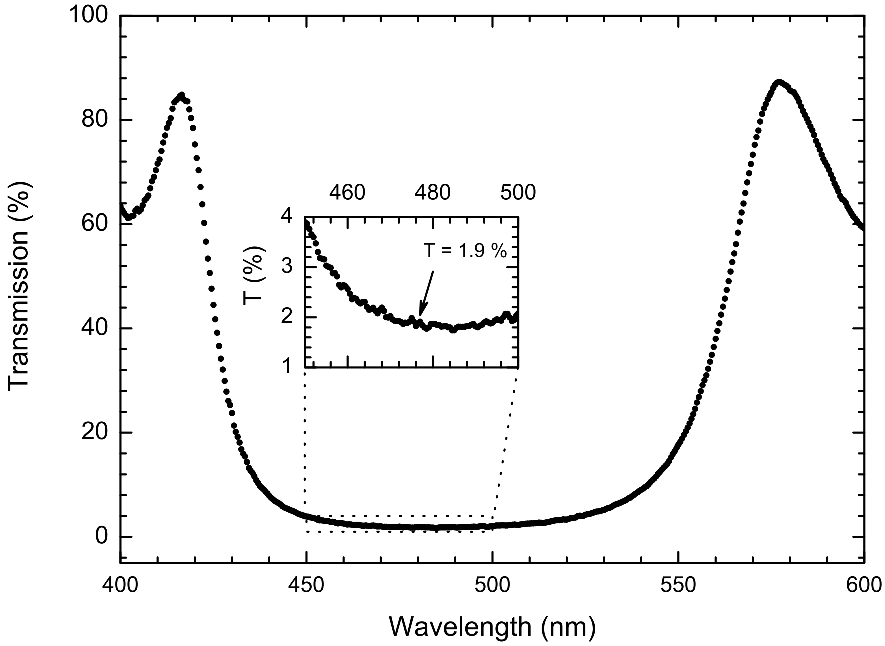

Figure 4.10: Measured transmission of the dielectric mirror used to fabricate the tunable microcavity, coated by Optische Interferenz Bauelemente GmbH with a structure g(HL)^{8}a (L:SiO$_2$, n = 1.46, H:Ta$_2$O$_5$, n = 2.1, g:glass, n = 1.46 and a:air, n = 1.0).

1.3%.

The top dielectric mirror was fixed to a titanium housing containing the bottom mirror mounted on a miniature nanopositioning stage. The lifted epilayer was deposited on the bottom mirror. An image (left) and schematic (right) of the completed tunable microcavity is presented in figure 4.11. A total of four nanopositioners was required to control the experiment. Three course nanopositioners align the entire microcavity in x,y,z and a fourth fine nanopositioner controls the physical length of the cavity. All of the positioners are manufactured and supplied by Attocube Systems AG. The positioners all work on the same principle, namely a slip-slide principle, where a saw-tooth voltage with a slow (fast) rise (fall) is applied to an internal multiple piezo-electric stack which moves the positioners on the slow rise only. The saw-tooth voltage is readily reversed allowing motion in the opposite direction. The course positioners are designed for $\sim$ 5 nm precision at 4.2 K. The spatial resolution of the fine positioner is < 1 nm at 4.2 K. Hysteresis and non-linearity inherent to the piezo-electric stacks limits

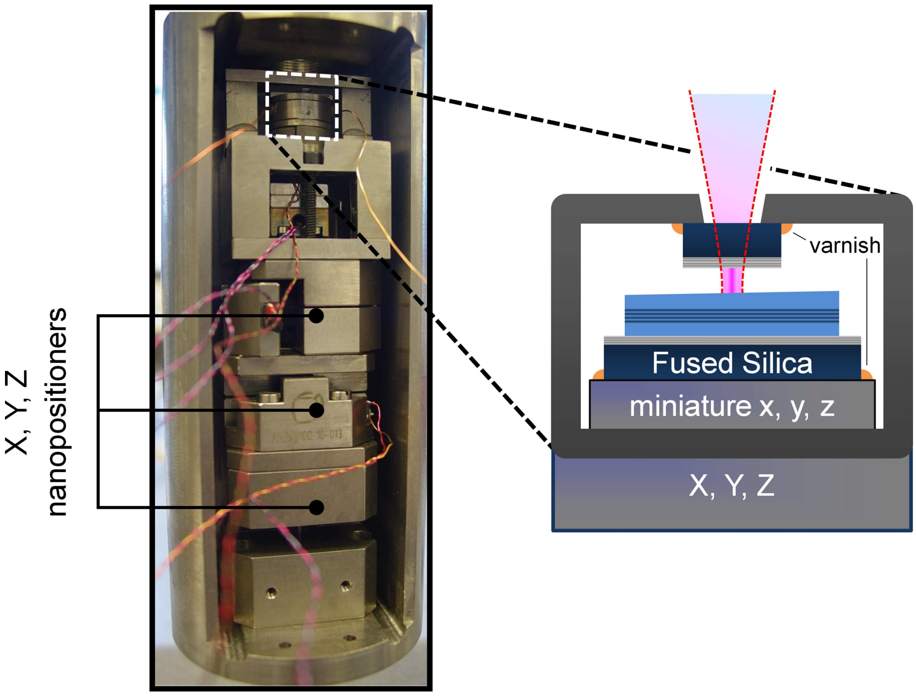

Figure 4.11: Image and schematic of the completed tunable microcavity. The miniature nanopositioning stage allows the cavity length to be varied over a few millimeters (for x and y the range is only a few μm). The air gap was measured to ~ 1 μm (this will be discussed further in chapter 5 section 5.3.

the experimentalist's knowledge to relative spatial positioning only. This is irrelevant for the three course positioners as they are simply used to align to the optical axis and not to travel specific distances. For the fine positioner this issue is readily resolved by using the spectral information collected during the microcavity experiments to deduce the energy of the bare cavity mode and thus the detuning relative to the quantum well exciton. The miniature nanopositioning stage allows the cavity length to be tuned into resonance with the internal quantum wells with nm precision. The microcavity was easily detuned by decreasing (increasing) the cavity length (energy) through resonance with the X$_{hh}$ and beyond with ~ 0.3 nm (~ 4 meV) increments in cavity length (energy).

Great care was taken when fixing the two mirrors in place to ensure parallelism. The degree of quality of parallelism was crucial. The angular tolerance must be satisfied; photons sent into (or generated in, in the case of photoluminescence experiments) the microcavity must not laterally wander out of the collection spot within the lifetime of the photon, determined by the reflectivity of the mirrors. This sets an upper limit to the maximum reflectivity that is useful,

$$R_{max} = 1 - \sqrt{\frac{\theta(d + \frac{L}{n_c})}{\Delta}}, \tag{4.1}$$

where d, L is, respectively, the physical thickness of the air gap, the ZnSe epilayer and the size of the collection spot at the microcavity surface. θ is the angle difference between the top and bottom mirror. From (4.1) the tolerance for parallelism is found to be, θ = 12.2×10^{-3} °for a cavity length composed of 170 nm of ZnSe and 1 μm of air with a mirror reflectivity of 98.2% and a collection spot size of 20 μm. The worst case scenario would be if the top mirror was tilted by θ = 1.2×10^{-2} °. It will be shown in chapter 5 that the angle between the mirrors for the fixed microcavity was found to be 1.1 $\times$ 10^{-4} °, 2 orders of magnitude below the critical angle found here. It is therefore expected that by taking care during the fabrication of the tunable microcavity, angular tolerance will not effect the quality of the microcavity for the given mirror reflectivity. Note that the tolerance of parallelism increases quadratically with $(1 - R)$.

The top and bottom mirrors were installed in the titanium housing with a cryogenic varnish, with the epilayer deposited onto the bottom mirror. The design of the housing and internal layout (except the microcavity itself) is the work of a fellow Ph.D. student. A detailed discussion of this work is reserved for the thesis of R. J. Barbour. To align the plane of the top to the plane of the bottom mirror, the cavity air gap was closed using the miniature nanopositioner whilst the varnish was still soft and left until the varnish was dry.

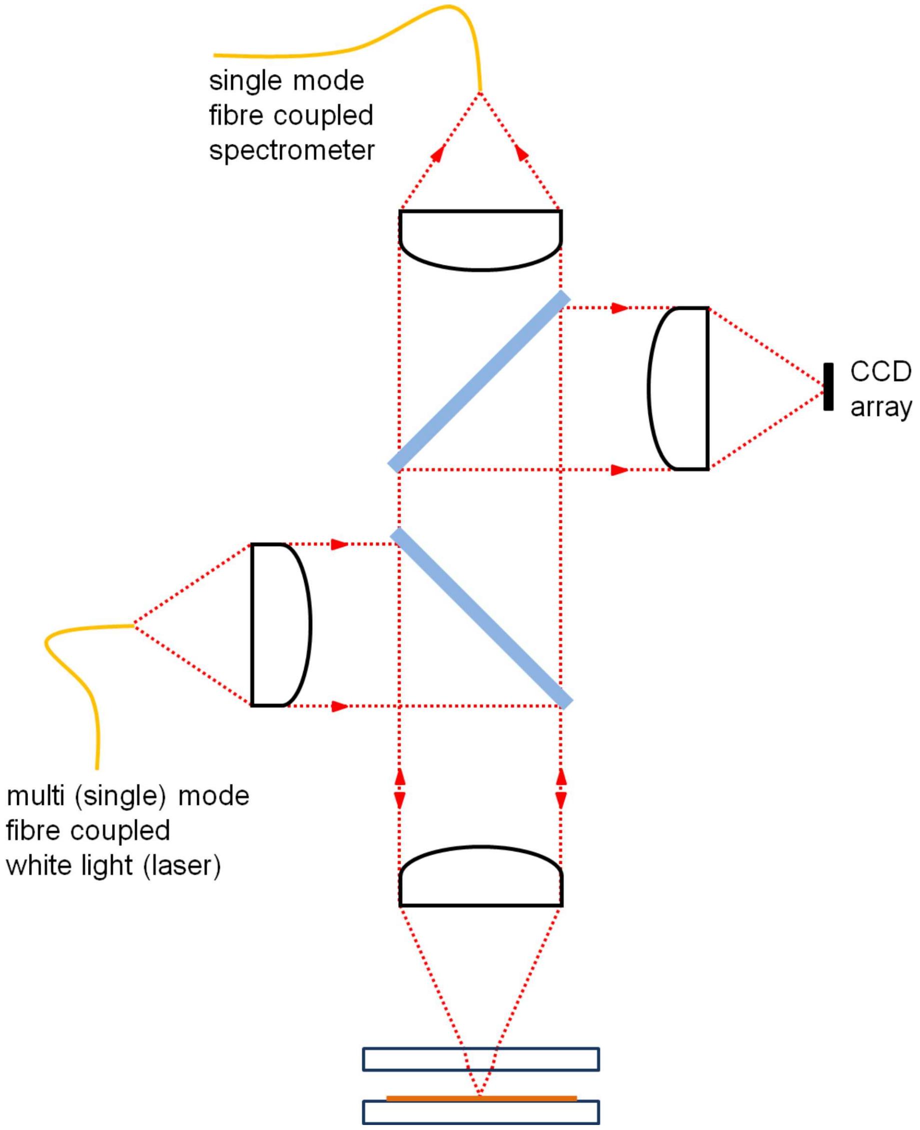

Figure 4.12: Tunable microcavity experimental setup. The optical input is on the left hand side of the confocal microscope followed by a thick glass beam splitter, sending 4% of the input light to the sample object. The same objective is used to collect and collimate optical information from the microcavity. A long focal length (NA = 0.17) microscope objective was used to limit angular dispersion. For reflection experiments, the output from a tungsten bulb was coupled to a multimode fibre and focused to an estimated spot size of $\sim 20\ \mu$m just below the top mirror. For photoluminescence experiments a single mode fibre coupled solid state laser emitting at 474 nm was used as excitation. Both reflection and photoluminescence were dispersed by a fibre coupled spectrometer with a resolution of 0.1 nm and imaged onto a liquid nitrogen cooled CCD camera.

4.4.1 Confocal microscopy

Once the fabrication of the tunable microcavity was finished the housing was transferred to a closed confocal microscope which was then immersed in liquid nitrogen.

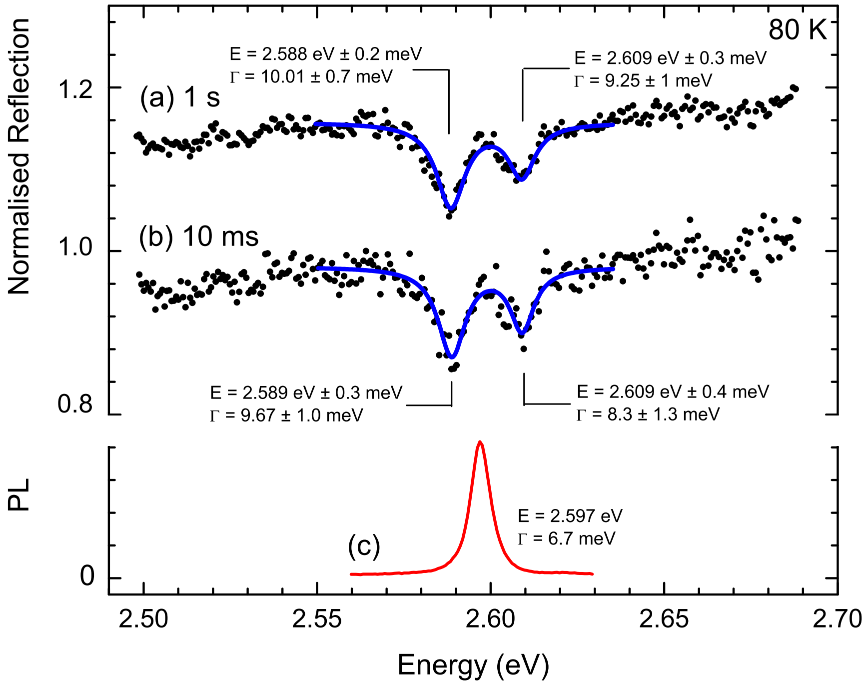

Figure 4.13: Tunable microcavity reflection spectra for (a) 1000 ms and (b) 10 ms exposure times. The measured linewidths confirm a high degree of stability in the cavity. The solid lines are Lorentzian curves as guide to the eye. Spectra are offset for clarity. (c) Photoluminescence from the uncoupled quantum wells.

Figure 4.12 shows a schematic of the confocal microscope setup used. Light is coupled into the setup at the left hand side of the microscope. A thick glass beam splitter was used to send 4% of the input light to the sample object. The same objective is used to collect and collimate optical information from the microcavity which is then focused into a single mode fibre at the top of the microscope and then dispersed by a fibre coupled spectrometer with a resolution of 0.1 nm and imaged onto a liquid nitrogen cooled charged coupled device. A long focal length microscope objective ($\times 10$, NA = 0.17) was used to limit angular dispersion. Taking into account the fused silica substrate, the total angular spread was $\sim 10°$. This was further reduced to $\sim 4°$ with a 3 mm aperture. For reflection experiments, the output from a tungsten bulb was coupled to a multimode fibre and focused to an estimated spot size of ~ 20 μm just below the top mirror. For photoluminescence experiments a single mode fibre coupled solid state laser emitting at 474 nm was used as excitation.

Resonant reflection spectra are presented in figure 4.13 (a-b) clearly showing that the microcavity is operating in the strong coupling regime. Two resolvable transitions are seen at 2.588 eV and 2.609 eV on either side of the energy of the heavy hole exciton. The uncoupled photoluminescence of the heavy hole transition was observed by detuning the microcavity and is presented in figure 4.13 (c). The stability of the two mirrors relative to one another is crucial since poor mechanical stability would ‘dither’ the cavity photon mode resulting in broadening of any observed transitions. A high degree of stability is evident since < 1 meV deviation for spectra taken with 1000 ms and 10 ms exposure times is observed (figures 4.13 (a) and (b), respectively). It is noted that the signal-to-noise ratio (SNR) does not increase by a factor of 10 when the exposure time is increased by a factor of 100, as would be expected. This is attributed to noise associated with the multimode fibre used to couple white light into the optical system. In addition, reflection from the semiconductor-air interface within the microcavity will also contribute to a lower than expected SNR. A detailed discussion of the optical features of the tunable microcavity operating in the strong coupling regime is presented in chapter 5.

Chapter 5

Strong exciton-photon hybridisation

In chapter 4, the fabrication of three different ZnSe based microcavities was discussed. The strong hybridisation of the exciton and cavity photon in a fixed microcavity and a complectly tunable microcavity is detailed in the following sections.

5.1 Fixed microcavity

Following the transfer of the quantum wells to the dielectric mirror the microcavity sample was completed by placing and securing the second mirror on top of the epilayer. The design and fabrication of the fixed microcavity was discussed in detail in chapter 4 section 4.2 and the sample was shown to operate in the strong coupling regime at normal incidence (figure 4.6). The linear characteristics of the cavity polariton were experimentally probed, the findings of which are presented and discussed below. The dispersion of the polariton is generally measured by detuning one of the composite states whilst the other state is energetically stationary. In the case of the cavity polariton either the exciton or the cavity photon is tuned by a variety of experiential methods, for example, by varying the sample temperature to tune the exciton transition to the cavity photon. This is common practice when the excitation state is confined in a three dimensional structure, such as a quantum dot, limiting the possible techniques that can tune the cavity without displacing the sample in the growth plane. The work presented in this thesis is centred around a 2 dimensional quantum well and lateral displacement of the sample is therefore an option. The following experimental methods were employed when measuring the polariton dispersion:

1. Translational tuning, $\delta = E_c(L_c) - E_{hh}$
2. Angle of incident tuning, $\delta = E_c(\theta_i) - E_{hh}$

In each experiment, the tuning variable has a negligible effect on one of the composite states whilst tuning the other state. Translational tuning was achieved by introducing a gradient across the wafer during the last stage of the semiconductor growth (see chapter 3 section 3.1). Ensuring the region over which the microcavity sample was probed was free from microscopic defects, for example cracks in the epilayer or trapped dust particles, the cavity mode could be tuned with ~ 1 meV increments. For angle of incidence tuning, the dispersion curves of the bare exciton and cavity photon are parabolic-like, dependent on the effective mass of the particle, but since the cavity photon effective mass is five orders of magnitude smaller than the exciton, the dispersion of the exciton is negligible and appears as a constant.

5.1.1 Translational tuning of the cavity mode

The ZnSe based epilayer used to fabricate the microcavities was carefully designed such that the thickness at the centre of the wafer corresponded to a single optical wavelength at 475 nm with a gradient across the wafer, giving a variance in thickness. This was achieved by stopping the wafer rotation during the growth of the last ZnSe spacer. This allows the cavity photon to be energetically tuned relative to the quantum well exciton, by varying the position where the sample is probed. The experimental details were discussed in chapter 4 section 4.2.

A series of WLC transmission spectra taken for a sample temperature of 80 K, for increasing cavity energy (decreasing cavity length) by translating the sample in the plane normal to the optical axis is presented in figure 5.1. In the sample presented here, there are three composite states, the light and heavy hole excitons and the cavity

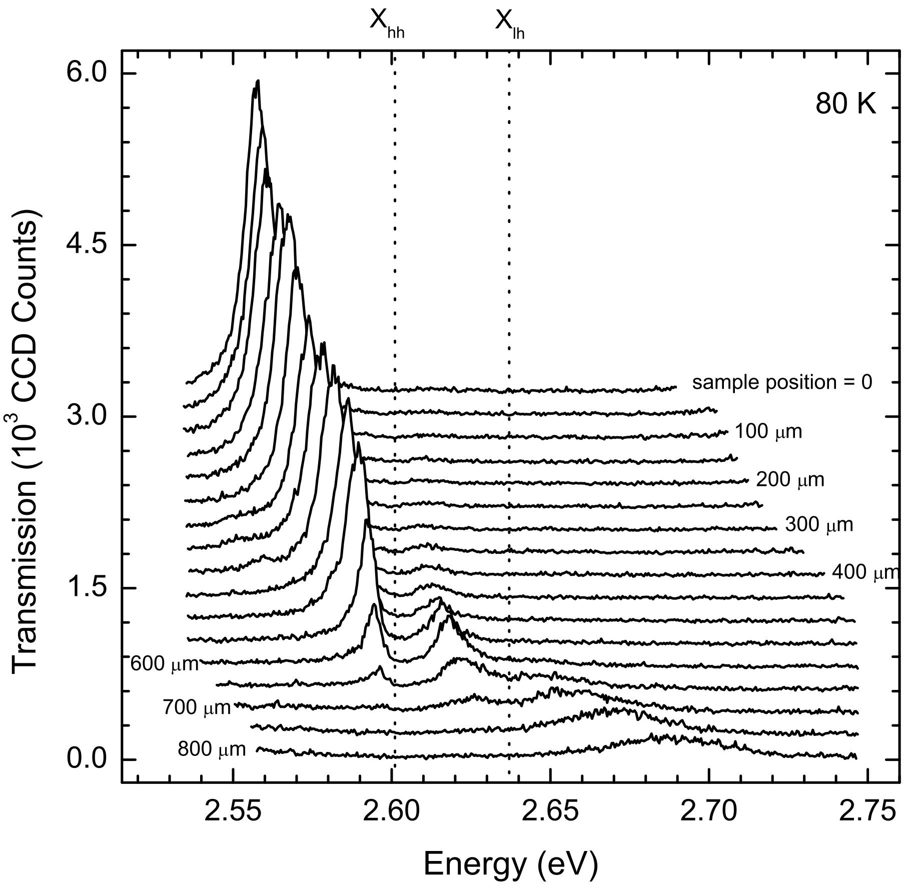

Figure 5.1: White light transmission spectra collected as the sample is translated in a plane normal to the optical axis. Due to the wedge shape of the semiconductor epilayer, laterally translating the sample tunes the energy of the cavity mode. The experiment starts with the cavity at E$_c$ = 2.560 eV ($<$ E$_{Xhh}$ = 2.601 eV) and is increased to E$_c$ = 2.685 eV ($>$ E$_{Xlh}$ $\sim$ 2.637 ± 0.05 eV). The energies of the heavy and light hole excitons were measured from transmission experiments on a bare reference sample (dotted lines). White light continuum generated from ~ 2 μJ, fs pulses from a Ti:Sapphire laser was used to illuminate the sample (see chapter 4 section 4.2). Spectra are offset and data at the high and low bandedges of the dielectric mirrors have been removed for clarity.

photon, leading to three coupled states, the lower, middle and upper polariton. The transmission spectra are offset with the highest spectrum corresponding to a cavity energy, E$_c$ = 2.560 eV ($<$ E$_{X_{hh}}$ = 2.601 eV) and is then tuned through the heavy hole and light hole exciton transitions. The sample was translated in increments of 50 μm. The entire experiment was over a spatial region of ~ 1 mm $\times$ the white light spot size (~ 20 μm). Care was taken when selecting the region of sample such that a sufficient range of detuning was accessible within a crack free region of the quantum wells. The energies of the heavy hole and light hole excitons, measured from transmission

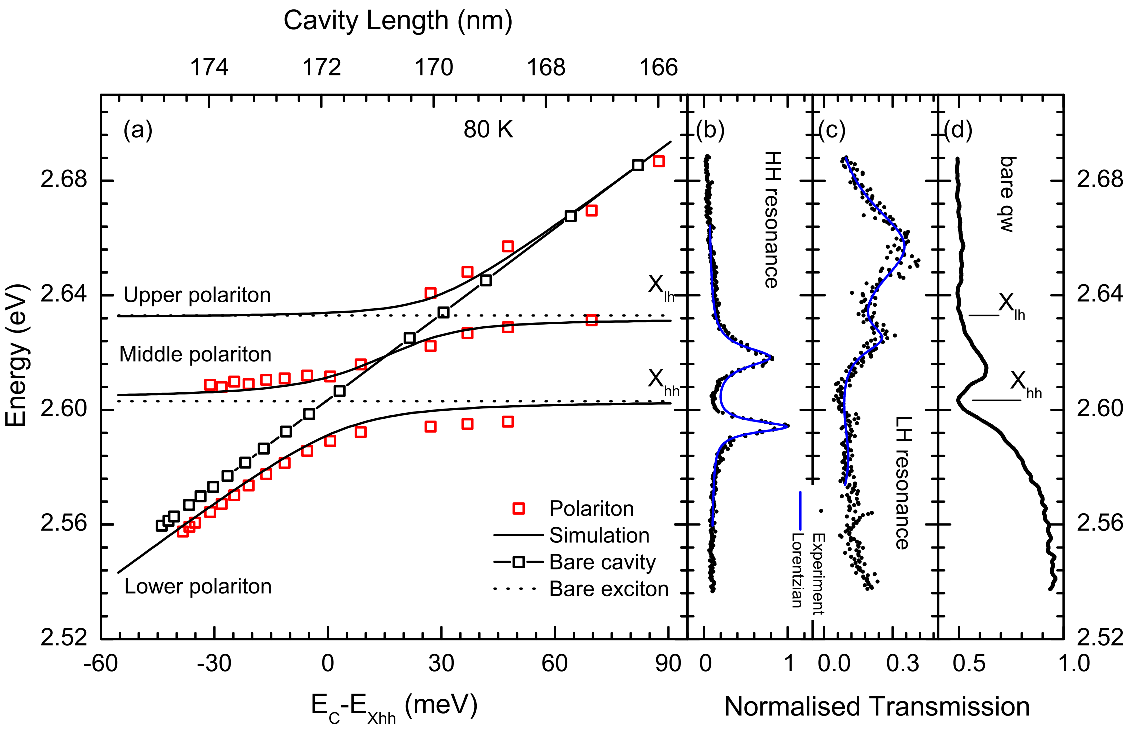

Figure 5.2: (a) Energy peak values from Lorentzian curves fitted to the spectra in figure 5.1 (open red squares). The polariton dispersion curves are compared to the model discussed in the text (solid lines). The bare cavity energy was also deduced using the model (open black squares) and used to calibrate the detuning. Resonance occurs with the heavy (light) hole (identified by the dotted lines) with a matrix element $\hbar V_{hh(lh)}$ = 10.2 (7.5) meV. Normalised transmission spectra for when the cavity is resonant with the (b) heavy hole and (c) light hole excitons. (d) Normalised transmission spectrum for the bare quantum well. All the data is taken at a sample temperature of 80 K.

spectrum taken from lifted quantum well reference samples (figure 3.5 (b) and figure 5.2 (d)), are E$_{X_{hh}}$ = 2.601 eV and E$_{X_{lh}}$ $\sim 2.637 \pm 0.05$ eV, highlighted by the dotted lines.

The energy peak values for each coupled state, the lower, middle and upper polaritons were measured using Lorentzian fits to the spectra in figure 5.1 and are presented in figure 5.2 (a) (open red squares). Treating the composite states of the polariton as coupled oscillators, the eigenvalues of the coupling Hamiltonian were used to calculate the energy dispersion of the lower, middle and upper polaritons taking the matrix elements, $\hbar V_{hh(lh)}$ as fit parameters. The 2 level coupled oscillator model was introduced and discussed in chapter 2 section 2.3.2. Since there are three composite states a 3×3 coupling matrix is required to describe the coupled states. The response of the system can then be determined from the eigenvalues and eigenvectors of the coupling matrix,

$$M_\delta = \begin{pmatrix} E_c(\delta) + i\gamma_c & \hbar V_{hh} & \hbar V_{lh} \\ \hbar V_{hh} & E_{hh}(\delta) + i\gamma_{hh} & 0 \\ \hbar V_{lh} & 0 & E_{lh}(\delta) + i\gamma_{lh} \end{pmatrix}, \tag{5.1}$$

where $V_{hh(lh)} = \sqrt{\frac{c\Gamma_0^{hh(lh)}(1+\sqrt{R})}{n_c L_{eff}\sqrt{R}}}$ is the matrix element between $X_{hh(lh)}$ and the cavity photon. Γ_0 is the exciton amplitude decay rate.

To calibrate the detuning, $\delta = E_c(\delta) - E_{hh}$ the coupling matrix (5.1) was first solved for cavity energy, $E_c(\delta)$. The three polariton states observed in the transmission were then used to deduce the actual cavity dispersion (open black squares, figure 5.2 (a)). From the calibrated detuning the energetic (cavity length) detuning increments were found to be ~ 7 meV (0.5 nm). The average translational tuning was designed and measured to be ~ 20 meV mm^{-1} from optical interference measurements performed on reference ZnSe samples, discussed in chapter 3. This is nearly an order of magnitude smaller that observed here, ~ 140 meV mm^{-1}, deduced from the observed cavity dispersion (figure 5.2 (a)). This cannot be simply explained by surface roughness in the fused silica substrates used since the surface roughness was measured to be $< \frac{\lambda}{10}$ using AFM. The discrepancy between the thickness gradient of the bare reference samples and completed microcavities is most likely due to dust particles becoming trapped within the microcavity during the fabrication stage. Even though great care was taken to reduce this, it is noted that a 10 nm particle trapped within the 5×5 mm microcavity would be sufficiently large enough to result in a similar magnitude of translational tuning.

As the energy of the cavity mode approaches resonance with the heavy and light hole exciton transitions in figure 5.2 (a), the observed spectral peaks clearly anti-cross around each resonance. This is a clear demonstration of strong exciton photon coupling. The best fit to the dispersion as a function of detuning was achieved with matrix elements, $\hbar V_{hh(lh)}$ = 10.2 ± 0.4(7.5 ± 0.6) meV. In the high reflectivity limit, and assuming exciton cavity resonance, an analytic formula for the observable spectral splitting in transmission, $\hbar\Omega_T$ is given by [50],

$$\hbar\Omega_T^{hh(lh)} \simeq 2\sqrt{\sqrt{(\hbar V_{hh(lh)})^4 + 2(\hbar V_{hh(lh)})^2 \gamma_{X_{hh(lh)}}(\gamma_{X_{hh(lh)}} + \gamma_c)} - \gamma_c^2}. \tag{5.2}$$

From the spectral observations of the uncoupled microcavity, $\gamma_{hh(c)}$ = 10.1 ± 0.1 (15.5 $\pm$ 0.2) meV (figure 4.5) the expected spectral splitting from the coupled heavy hole exciton and cavity photon can be calculated using the fit parameter, $\hbar V_{hh}$ = 10.2 ± 0.4 meV, deduced from fitting to the polariton dispersion, and compared to the observed spectral splitting. $\hbar\Omega_T^{hh}$ = 24.7 ± 1.8 meV compares well with the experimental splitting of 24.1 ± 0.5 meV, further confirming the quality of the fit in figure 5.2. It was not possible to measure accurately the linewidth of the quantum well light hole exciton. Using the value measured for the heavy hole exciton and $\hbar V_{lh}$ = 7.5 meV, equation (5.2) is purely imaginary. This would be expected if the states were coupling in the weak regime, but the experimental observations clearly evidence strong coupling. It is likely that the linewidth is broadened for the light hole and the use of the heavy hole linewidth is not valid (see figure 5.2 (d)). From figure 5.2 (a) the observed spectral splitting of the light hole exciton and cavity photon is measured to be, $\hbar\Omega_T^{lh}$ = 13.6 ± 0.3 meV. The expressions for the spectral splitting in transmission, $\hbar\Omega_T^{hh(lh)}$, equation (5.2) and the normal mode splitting, $\hbar\Omega$, equation (2.28) are plotted in figure 5.3 for γ_c = 15.5 ± 0.2 meV and $\hbar V_{lh}$ = 7.5 ± 0.3 meV. The striking comparison of the two expressions is that they are equivalent for only one value of γ_X, below which the observable spectral splitting in transmission is actually greater than the normal mode splitting. From figure 5.3 the light hole exciton linewidth is found to be 12.8 ± 1.2 meV. A solid circle marks this point along the calculated $\hbar\Omega_T^{lh}$ curve.

The heavy hole exciton oscillator strength per quantum well, $f_{hh(lh)}$ can be determined from the matrix elements, $\hbar V_{hh(lh)}$ [50],

$$f_{hh(lh)} = \frac{\epsilon_o m_o}{2e^2\hbar^2}\frac{(\hbar V_{hh(lh)} n_c)^2 L_e}{N_{qw}}, \tag{5.3}$$

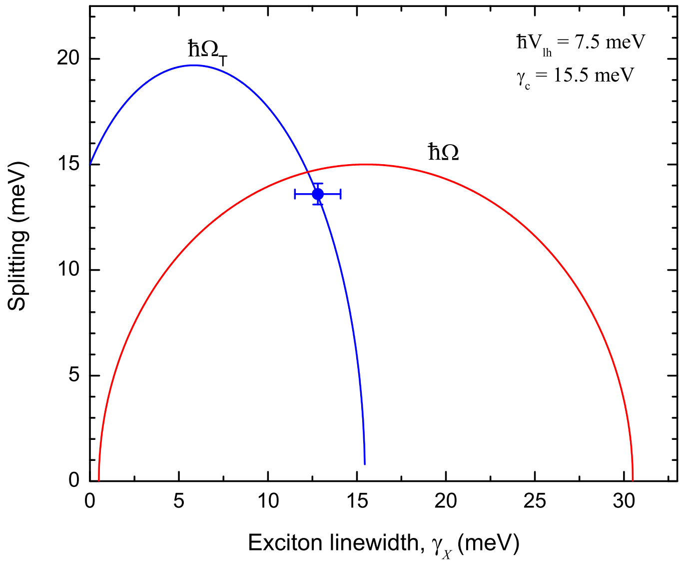

Figure 5.3: Comparison of the expressions for the spectral splitting in transmission, $\hbar\Omega_T$ (5.2) (blue) and the normal mode splitting, $\hbar\Omega$ (2.28) (red) for γ_c = 15.5 ± 0.2 meV and $\hbar V_{lh}$ = 7.5 $\pm$ 0.3 meV. The observed spectral splitting for the light hole exciton is marked by a solid dot and corresponds to a linewidth of 12.8 ± 1.2 meV.

where the number of quantum wells, N_{qw}, the cavity refractive index, n_c and effective cavity length, L_{eff} (see chapter 2 section 2.2.1) are 5, 2.78 and 571 nm respectively. m_o is the free electron mass. For the fixed microcavity the linewidth of the composite states was measured to be, $\gamma_{X_{hh(lh)}}$ = 10.12 (12.8) meV and γ_c = 15.5 meV with $\hbar V_{hh(lh)}$ = 10.2 (7.5) meV from the fit in figure 5.6 (a). The light hole exciton linewidth was deduced from the observed spectral splitting (figure 5.3). From (5.3) the oscillator strength for the heavy and light hole exciton at 80 K, $f^{80K}_{hh(lh)}$ is found to be 1.33 ± 0.10 (0.72 ± 0.14) $\times 10^{13}$ cm^{-2}. This is similar to $f^{50K}_{hh} \sim$ 1 $\times 10^{13}$ cm^{-2} for the ZnSe based microcavity studied by Kelkar *et al.* [13] at 50 K, but much smaller than the surprisingly high value, $f^{300K}_{hh} \sim$ 7 $\times 10^{13}$ cm^{-2}, reported by Pawlis *et al.* for their ZnSe based microcavity at room temperature [38]. f_{hh} does not appear in any publications from Pawlis *et al.* and was deduced here based on the published data [38]. The works of Kelkar [13], Pawlis *et al.* [38] are the only published evidence of ZnSe based microcavities operating in the strong coupling regime, beside the work presented here. Both experiments were based on a traditional back etching technique to allow access

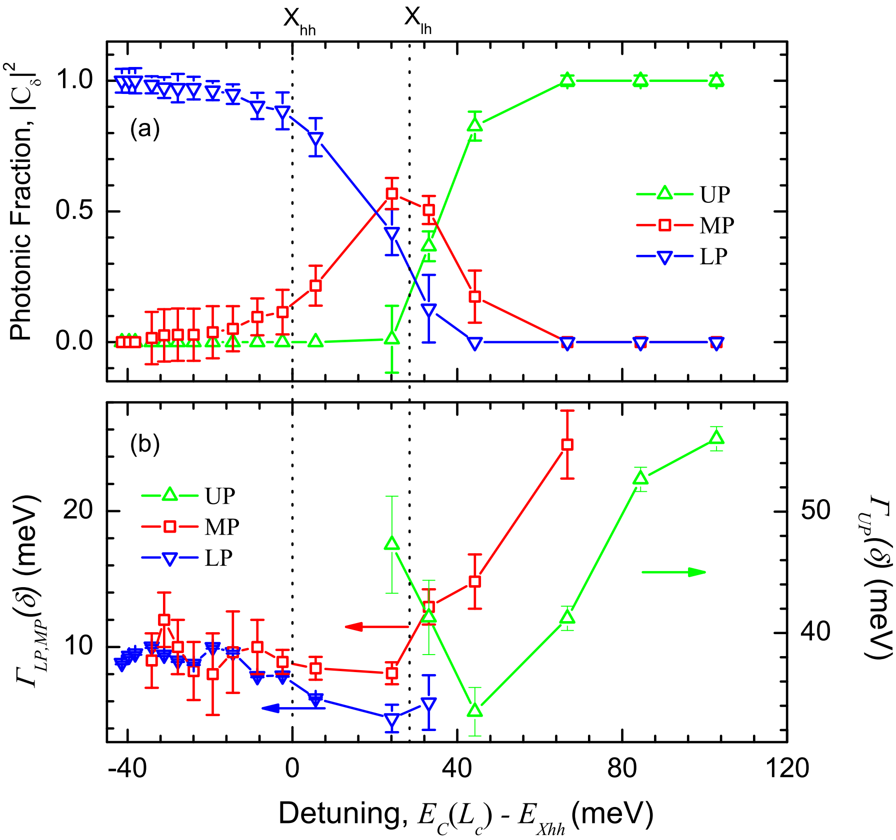

Figure 5.4: (a) Normalised integrated transmission intensity for the lower, middle and upper polariton states as a function of detuning, δ. (b) Measured polariton linewidths, $\Gamma_{LP,MP,UP}(\delta)$. Γ_{UP} is significantly larger than $\Gamma_{LP,MP}$ and has been plotted on its own axis (right) for clarity. Detuning corresponding to the X$_{hh}$ transition at 0 meV and X$_{lh}$ transition at $+32$ meV, are indicated by the dotted lines.

to deposit the bottom dielectric mirror.

The polariton state transmission amplitude is a measure of the polariton composite ratio (chapter 2 section 2.3.2) [34]. From the Lorentzian curves fitted to the white light transmission spectra, the measured integrated intensity, $I_{ii}(\delta)$ was normalised such that $\sum I_{ni}(\delta) = 1$ using, $I_{ni}(\delta) = \frac{I_{ii}(\delta)}{\sum I_{ii}(\delta)}$. The subscripts ii and ni denote, respectively, the measured integrated intensity and the normalised integrated intensity for a given polariton state. The normalisation also removes the intensity profile present in the white light cross section profile. The normalised integrated intensity of the polariton, $I_{ni}(\delta)$ is presented in figure 5.4 (a). For negative detuning and up to $\delta = +$ 20 meV, the lower polariton is predominately photonic-like, indicated by the high optical intensities observed in the spectra (figure 5.1). As the sample is tuned past resonance with the heavy hole exciton the photonic fraction of the middle polariton starts to increase whilst the upper polariton remains excitonic-like. Near zero detuning it is expected that the lower and middle polariton photonic fractions would intersect, however, this is not observed until δ = $+\ 20$ meV, well above resonance with the heavy hole exciton. At the same point the upper polariton begins to exhibit a photonic-like composite fraction, indicated by the increase in the integrated intensity. For detuning of $+$ 35 meV the middle and upper polariton are half photon, half exciton and the lower polariton is predominantly excitonic-like. For large detuning, $\delta \geq$ 80 meV the lower and middle polariton are purely excitonic and the upper polariton is purely photonic. For either $E_{lh} \gg E_{hh}$ or $V_{hh} \gg V_{lh}$ the mixing of the excitonic and photonic states on resonance results in equally weighted composite ratios. In the system presented here $V_{hh} \sim V_{lh}$ and $E_{lh} > E_{hh}$ and the resulting points of crossing of the polariton photonic fractions are expected to be slightly off-resonance. The data presented here evidences some mechanism by which polaritons are 'leaking' out of the upper state.

Another key feature of the cavity polaritons presented here is the point at which the lower polariton linewidth narrows. Figure 5.4 (b) presents the measured linewidth of the three polaritons states as a function of detuning. For negative detuning the lower and middle polariton linewidths are similar, $\sim$ 9 meV and only the lower polariton exhibits significant narrowing around, δ = 20 meV. The additional broadening to the higher energy polariton has been ascribed to absorption effects by the exciton continuum [51], but this was later shown to be inapplicable since the effect was still observed when the exciton continuum was blue shifted in magnetic spectroscopy experiments [52]. However, the present work involves the additional coupling to the broader light hole exciton and the possibility of phonon scattering from the middle and upper polariton branches, both which are contributing factors to broadening effects. Clearly, narrowing of the linewidths does occur, but as with the photonic fractions, does not occur at point of resonance. This is significant since it rules out the spectral filtering due to the overlap of the cavity mode over the exciton transition, proposed by Kavokin [53]. This will be discussed further in section 5.2.

5.1.2 Angle resolved spectroscopy, probing momentum space

Having clearly evidenced the fixed microcavity to operate in the strong coupling regime the optical dispersion of the polariton was measured in momentum space. The simplest experiment to probe the microcavity in momentum space is angle resolved transmission spectroscopy. Transmission spectra taken with varying angles of incidence, θ at the microcavity are related to the internal in-plane wavevector, $k_{||} = \frac{\omega_c}{c} n_c \sin(\theta)$. With angle resolved WLC transmission spectroscopy described in chapter 4 (figure 4.4) the dispersion of the microcavity was be measured in k-space between $\pm 1.4 \times 10^6$ m^{-1} at 20 K.

Figure 5.5 (a) shows a contour plot of the series of individually normalised spectra taken for the fixed microcavity detuned to $\delta = -4.1 \pm 0.2$ meV relative to the X_{hh} transition at normal incidence. The collection fibre was scanned from $k_{||} = -1.4 \times 10^6$ m^{-1} ($-6°$) increasing to $k_{||} = 1.4 \times 10^6$ m^{-1} ($+6°$) in increments of $\sim 0.1 \times 10^6$ m^{-1} ($0.5°$). The uncoupled X_{hh} transition is indicated by the dotted line. The spectra for the angular range $0° \leq \theta \leq 6°$ are presented figure 5.5 (b) and are offset with the lowest spectrum corresponding to $k_{||} = 0$ increasing to $k_{||} = 1.4 \times 10^6$ m^{-1} ($+6°$). The uncoupled X_{hh} and X_{lh} transition are indicated by the dotted lines. Two optical features clearly anticross on either side of the X_{hh} transition, a clear demonstration of strong coupling in momentum space. For large angles of incidence the upper polariton appears to broaden significantly and it is assumed coupling to the light hole exciton at $\sim 2.637 \pm 0.05$ eV is responsible. However the polariton peaks are not well resolved and further discussion is limited to the heavy hole coupling only.

Figure 5.6 (a) clearly shows the dispersion of the spectral peaks observed in figure

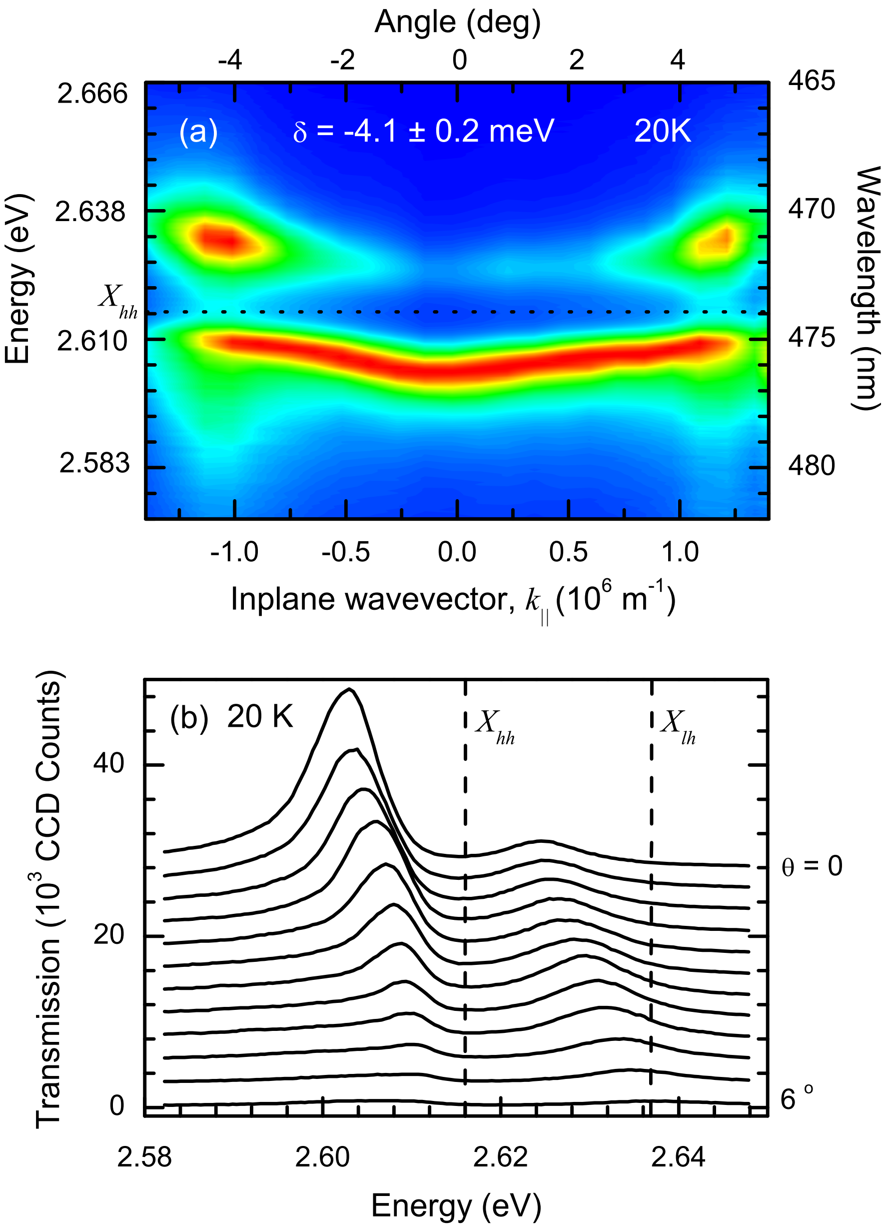

Figure 5.5: (a) Contour plot of the angle resolved transmission spectra from the fixed microcavity, negatively detuned. Each spectrum has been individually normalised. The sample was detuned by -4.1 ± 0.2 meV at $\theta = 0°$ and scanned to $\pm 6°$. The dashed line marks the uncoupled heavy hole exciton transition, X_{hh}. (b) Angle resolved transmission spectra for $0° \leq \theta \leq 6°$. The dashed lines mark the uncoupled heavy hole, X_{hh} and light hole, X_{lh} exciton transitions. Spectra are offset for clarity.

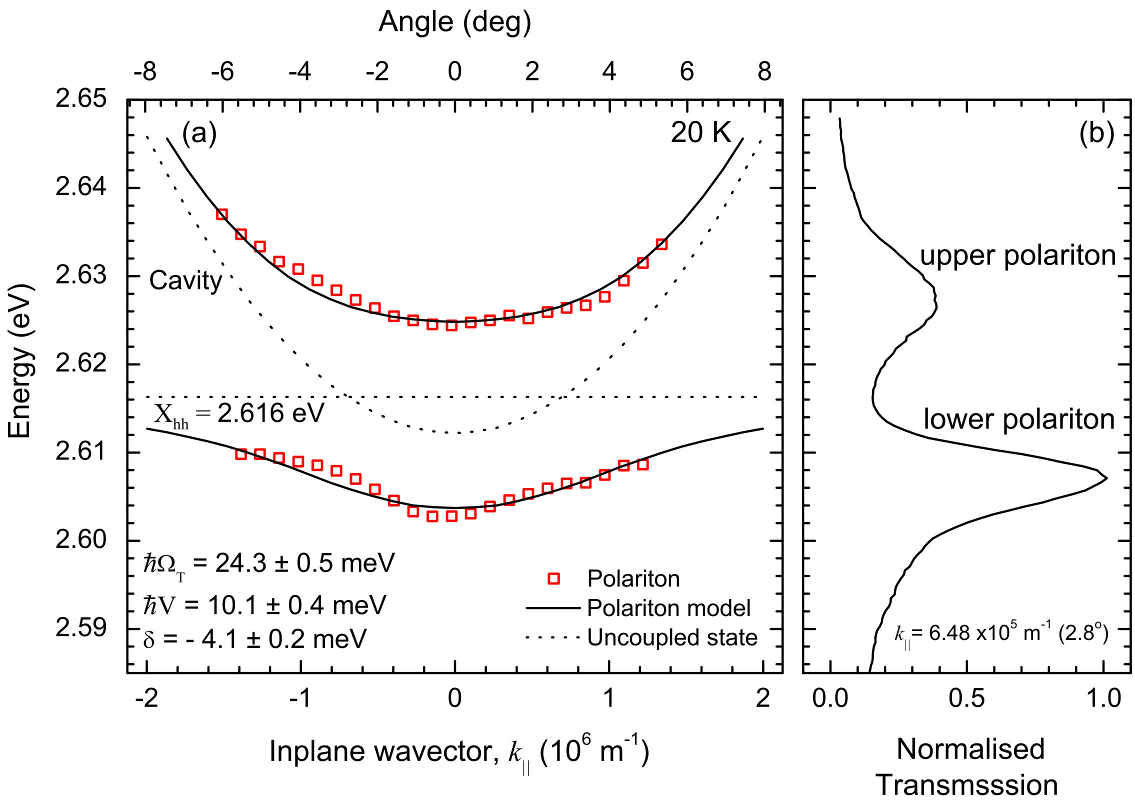

Figure 5.6: (a) Energy peak values from figure 5.5 (open squares). Resonance occurs at $k_{||} = \pm 6.48 \times 10^5$ m^{-1} ($\pm 2.8°$) with $\hbar\Omega_T = 24.3 \pm 0.5$ meV. The polariton dispersion curves are compared to the model discussed in the text (solid lines). Bare cavity and X_{hh} dispersion curves are also shown (dotted lines). (b) Transmission spectrum on resonance for $\delta = -4.1 \pm 0.2$ meV and $k_{||} = 6.48 \times 10^5$ m^{-1} ($2.8°$).

5.5, where the peak energy for the lower and upper polariton is presented as a function of $k_{||}$. The peak energy for the lower and upper polariton was extracted from figure 5.5 by fitting Lorentzian curves to each spectrum. As before, the composite states of the polariton are treated as coupled oscillators and the eigenvalues of the coupling Hamiltonian were used to calculate the energy dispersion of the lower and upper polariton taking the matrix element, $\hbar V$ as fit parameter (2.27). The coupled and bare states are displayed as solid and dotted lines, respectively, and give good agreement with the experimental data with $\hbar V$ = 10.1 ± 0.4 meV. The point of resonance between the heavy hole exciton and the cavity photon is found to occur at $k_{||} = 6.48 \times 10^5$ m^{-1} ($2.8°$) with an observed spectral splitting $\hbar\Omega_T$ = 24.3 ± 0.5 meV (Figure 5.6 (b)). From (5.2) and using γ_c = 15.5 ± 0.2 meV, γ_{hh} = 10.1 ± 0.1 meV and $\hbar V$ = 10.1 ± 0.4 meV,

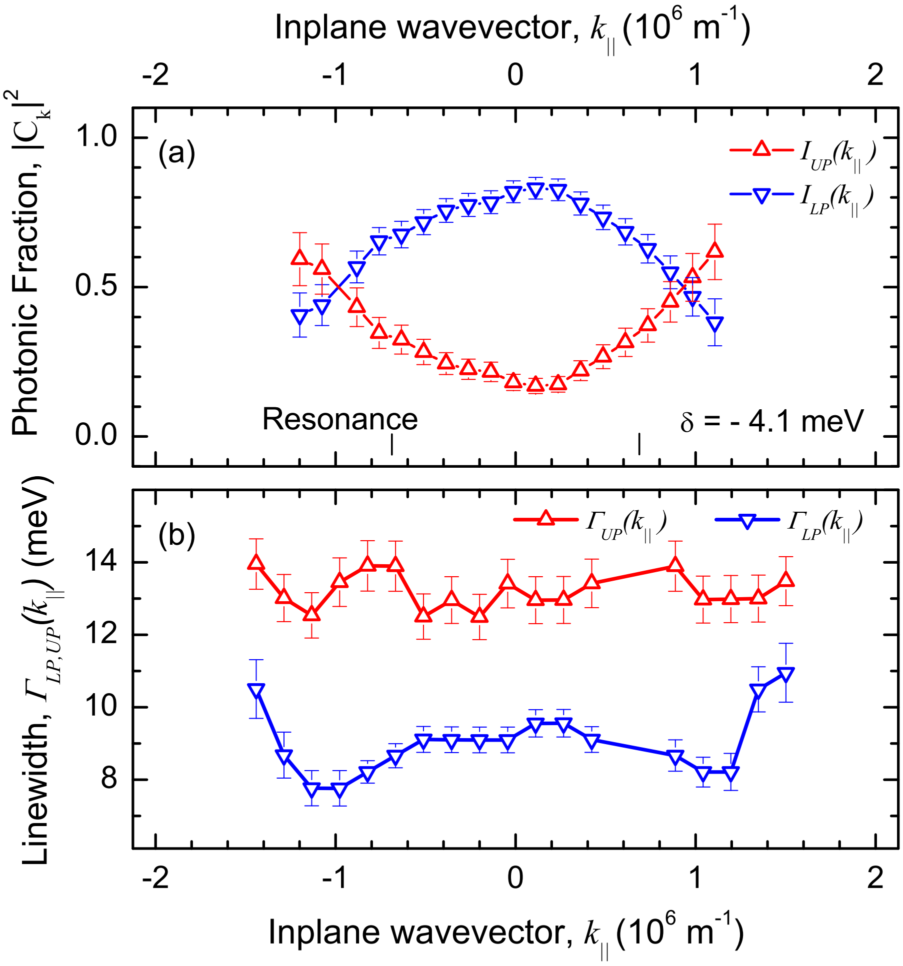

Figure 5.7: (a) Integrated transmission intensity for the lower and upper polariton states in the fixed microcavity, negatively detuned. (b) Measured polariton linewidths, $\Gamma_{LP,UP}(k_{||})$.

the observed splitting, $\hbar\Omega_T$, is calculated to be 24.3 ± 1.8 meV. This evidences the quality of the used fitting parameter $\hbar V$. The oscillator strength per quantum well (5.3) can now be calculating with confidence using $\hbar V$ = 10.1 meV and is found to be, f_{hh}^{20K} = $1.29 \pm 0.10 \times 10^{13}$ cm^{-2}. As for the cavity length tuning experiment (section 5.1.1), this result compares well to $f_{hh}^{50K} \sim 1 \times 10^{13}$ cm^{-2} for the ZnSe based microcavity studied by Kelkar *et al.* [13] at 50 K.

In figure 5.7 (a) the normalized integrated intensities, $I_{ni}(k_{||})$ of the lower and upper polariton branch are presented, giving a proportional indication of the evolution of the photonic fraction of the polariton. The subscript ni denotes the normalised integrated intensity for a given polariton branch. It is convenient to normalise the integrated intensities using $I_{ni}(k_{||}) = \frac{I_{ii}(k_{||})}{\sum I_{ii}(k_{||})}$ such that $I_{LP}(k_{||}) + I_{UP}(k_{||}) = 1$. The subscript ii denotes the measured integrated intensity for a given polariton branch. In the angular range of $-4^{\circ} \leq 0 \leq +4^{\circ}$ the lower polariton is predominantly photonic-like, indicated by the increase in the lower polariton intensity. Beyond this range the lower polariton weakens as it becomes progressively more excitonic and $E_{LP}(k_{||}) \rightarrow E_{hh}$. The upper polariton behaves inversely. It is noted that on resonance, figure 5.6 (b), $I_{lp}(k_{||}) > I_{up}(k_{||})$. $I_{lp}(k_{||}) = I_{up}(k_{||})$ holds at larger $k_{||}$ beyond resonance. This is also the case in the ZnSe based microcavity studied by Kelkar *et al.* [13]. The measured linewidths, $\Gamma_{LP,UP}(k_{||})$ of the lower and upper polariton are presented in figure 5.7 (b). Narrowing of the lower polariton linewidth is clearly evident and occurs at $k_{||} \simeq \pm 1 \times 10^{6}$ m^{-1} ($\sim \pm 3^{\circ}$). This is evidence that the extended nature of the polariton averages out some of the inhomogeneous broadening in the quantum well exciton. As with the resonance intensities, the linewidth of the lower polariton is at a minimum at larger $k_{||} = \pm 1 \times 10^{6}$ beyond resonance. The off-resonance behaviour observed here will be discussed further in section 5.2.

By repositioning the sample relative to the optical axis the dispersion of the polariton can be measured for a variety of detunings. Figure 5.8 presents the angle resolved transmission spectra for a positive detuning of $+4.5 \pm 0.2$ meV at $\theta = 0^{\circ}$ and scanned to $\pm 6^{\circ}$. The dashed lines mark the uncoupled heavy hole, X_{hh} and light hole, X_{lh} exciton transitions. As with the previous data, Lorentzian fits where used to extract detailed information from the spectra. The peak energy values are presented in figure 5.9 (a) where the coupling model is also graphed for $\hbar V$ = 10.3 ± 0.4 meV. To achieve the best fit the exciton energy was taken to be E_{hh} = 2.613 ± 0.01 eV, 3 meV below E_{hh} for the negatively tuned microcavity. The red shift in exciton energy between experiments is within the 0.5% error for the measured energy, and is assumed to be due to fluctuations in strain across the clamped microcavity. The energy of the exciton transition in the positively tuned microcavity was confirmed by solving the coupling

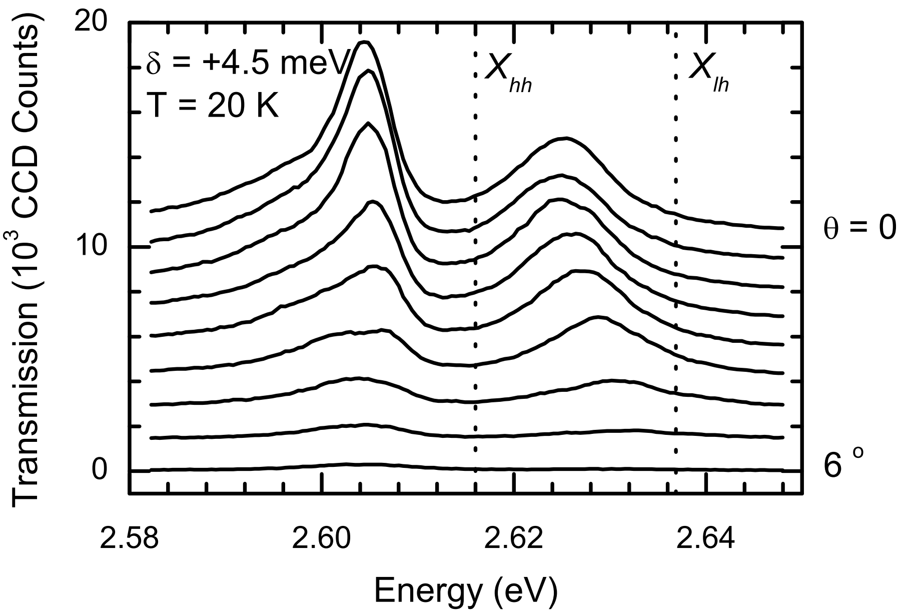

Figure 5.8: Angle resolved transmission spectra for $0^\circ \leq \theta \leq 6^\circ$. The sample was detuned by $+4.5 \pm 0.2$ meV at $\theta = 0^\circ$ and scanned to $\pm 6^\circ$. The dashed lines mark the uncoupled heavy hole, X_{hh} (E_{hh} = 2.1625 eV) and light hole, X_{lh} exciton transitions. Spectra are offset for clarity.

matrix for E_X and using the solution to extract E_X from the experimentally observed peaks and with $\hbar V$ = 10.3 ± 0.4 meV as input parameters.

The integrated intensities for the positively detuned microcavity, presented in figure 5.10 (a), exhibit similar features as for the negatively detuned microcavity. The expected profile of the photonic fractions is not observed and instead the lower polariton has a higher integrated intensity such that the photonic fractions of the lower and upper polariton are of the same order for zero in-plane wavevector. This would be expected only for δ = 0. For a positively detuned microcavity the upper polariton would be expected to be predominantly photonic-like for the full range of in-plane wavevector. No significant polariton narrowing effect is observed for the positively detuned microcavity (figure 5.10 (b)).

The experimental data presented for the fixed microcavity were observed at cryogenic temperatures ≤ 80 K. One of the advantages of working with the II-VI material system

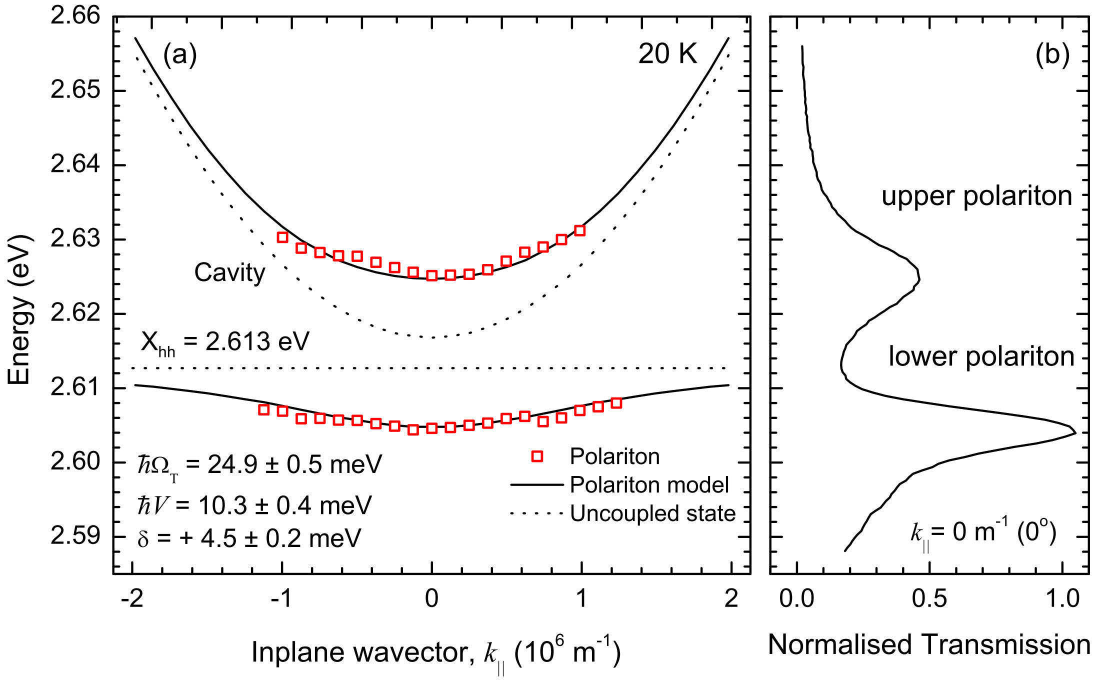

Figure 5.9: (a) Energy peak values (open squares) for detuning, δ = 4.5 ± 0.2 meV. Resonance occurs at $k_{||}$ = 0 m^{-1} ($0°$) with $\hbar\Omega_T = 24.9 \pm 0.5$ meV. The polariton dispersion curves are compared to the model discussed in the text (solid lines). Bare cavity and X_{hh} dispersion curves are also shown (dotted lines). (b) Transmission spectrum on resonance.

is the typical exciton binding energy, $E_b \sim 30$ meV [37]. For the ZnSe based microcavities discussed here the binding energy of the exciton is expected to be of the order of $k_B T$ at room temperature and it is therefore expected that the excitonic component of the polariton will not completely thermalise at room temperature. A transmission spectrum taken at 300 K with the cavity mode tuned to resonance with the exciton is presented in figure 5.11. Two peaks are resolvable at 2.501 eV and 2.522 eV, corresponding to the lower and upper polariton, respectively, with a spectral splitting of $hb\Omega_T$ = 19.5 ± 0.4 meV. From (5.2) and (5.3) the matrix coupling element and oscillator strength per quantum well at room temperature is found to be, $\hbar V$ = 8.8 ± 0.4 meV and f_{hh}^{300K} = 0.98 ± 0.08 $\times 10^{13}$ cm^{-2}, respectively. The polariton peaks off-resonance were not resolvable due to the polariton broadening at room temperature.

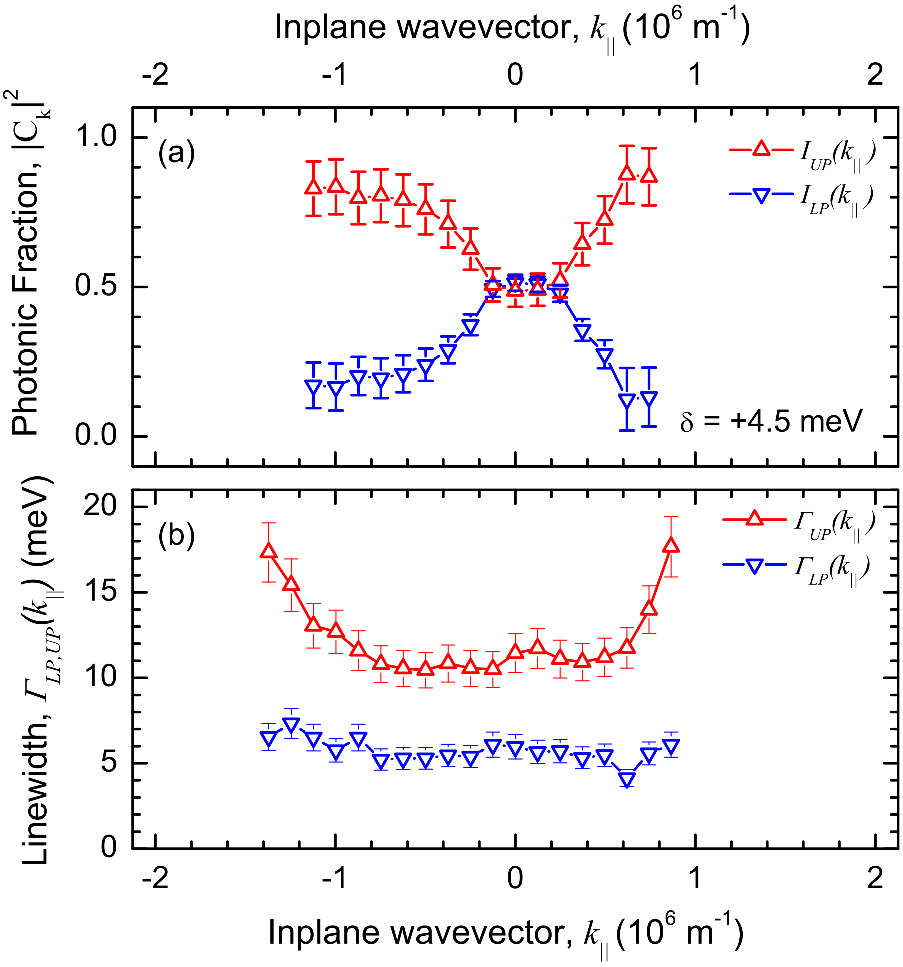

Figure 5.10: (a) Integrated transmission intensity for the lower and upper polariton states in the fixed microcavity, positively detuned. (b) Measured polariton linewidths, $\Gamma_{LP,UP}(k_{||})$.

5.2 Off-resonance behaviour of ZnSe based cavity polaritons

In the previous section of this chapter, the behaviour of the exciton and photon hybridisation was studied by translational tuning and angle resolved spectroscopy techniques. In section 5.1.1 the cavity mode was varied across a large range of cavity energies (~ 140 meV) and it was shown to couple strongly to both the heavy hole and light hole transitions. The polariton dispersion was successfully described using the eigensolutions of a 3×3 coupling matrix, describing each of the energetic states involved. In addition to the dispersion the integrated intensities and full width at half maximum of the polaritons were measured. Due to the hybridisation of the exciton

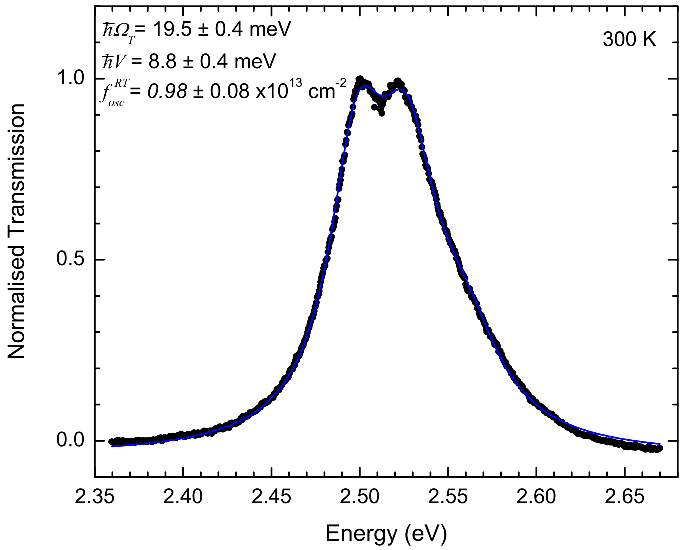

Figure 5.11: Room temperature transmission spectrum for the fixed microcavity showing two resolvable peaks at 2.501 eV and 2.522 eV. A two peak Lorentzian is fitted to the spectrum as guide to the eye.

and photon, the integrated intensities of the lower and middle polaritons are expected to be equivalent and the lower polariton is expected to narrow on resonance with the heavy hole exciton. The experimental findings, discussed above, are not as expected and the both effects were observed to occur off-resonance. The following discussion addresses the mechanisms responsible for the off-resonance behaviour. It will be shown that the experimental findings can not be explained by the inclusion of the light hole exciton.

5.2.1 Photonic fraction

For either $E_{lh} \gg E_{hh}$ or $V_{hh} \gg V_{lh}$ the mixing of the excitonic and photonic states on resonance is expected to result in equally weighted composite ratios. In the system presented here $V_{hh} \sim V_{lh}$ and $E_{lh} > E_{hh}$ and the experimental findings are that the points of crossing of the polariton photonic fractions are off-resonance. The eigenvectors of the 3×3 coupling matrix, (5.1) are not sufficient in describing the evolution of the polariton photonic fraction. Equality of the integrated intensities between the lower and middle polaritons and middle and upper polaritons is experimentally observed to occur for larger detunings than expected. The intersection points predicted by the eigenvectors of (5.1) occur only a few meV above resonance. From the data presented in figure 5.4 (a) and repeated in figure 5.12 (b) for comparison to theory, the lower and middle polariton photonic fraction cross for a detuning of, $\delta = +20$ meV above resonance. Similarly, the expected point of intersection of the photonic fractions of the middle and upper polariton is expected to correspond to the light hole exciton transitions at $\sim +30$ meV above the heavy hole, measured from the uncoupled quantum well transmission (figure 5.2 (d)). The actual intersection is found at a detuning of $+35$ meV, closer to the expected value than in the case of the lower and middle polariton but still evidencing some mechanism which redistributes the photonic fractions. Another key feature of the cavity polariton is the point at which the lower polariton linewidth narrows. Figure 5.4 (b) presents the measured linewidth of the three polaritons states as a function of detuning. Clearly, narrowing of the linewidths does occur, but as with the photonic fractions, does not occur at the point of resonance. This is significant since it rules out the spectral filtering due to the overlap of the cavity mode with the exciton transition, proposed by Kavokin [53], and suggests that the narrowing effect is due to the extended nature of the polariton averaging out some of the inhomogeneous broadening in the quantum well exciton which only occurs for polaritons composed of half exciton, half photon.

It is noted that the energy separation of the lower and middle polariton is $\Delta E \sim 27$ meV and considering the linewidths (figure 5.4 (b)), is of the order of crystal vibration quanta, the longitudinal optical phonon, $\omega_{LO} \sim$ 30 meV for $\mathrm{Zn_{0.9}Cd_{0.1}Se}$ quantum wells [37]. It is therefore anticipated that broadening of the higher energy polariton states will occur due to phonon scattering events. The relatively large polariton linewidths mean that interbranch transitions at detunings away from resonance are also energetically possible. It is estimated that such transitions are allowed over a large range of detunings since the linewidth of the lower and middle polariton ~ 8

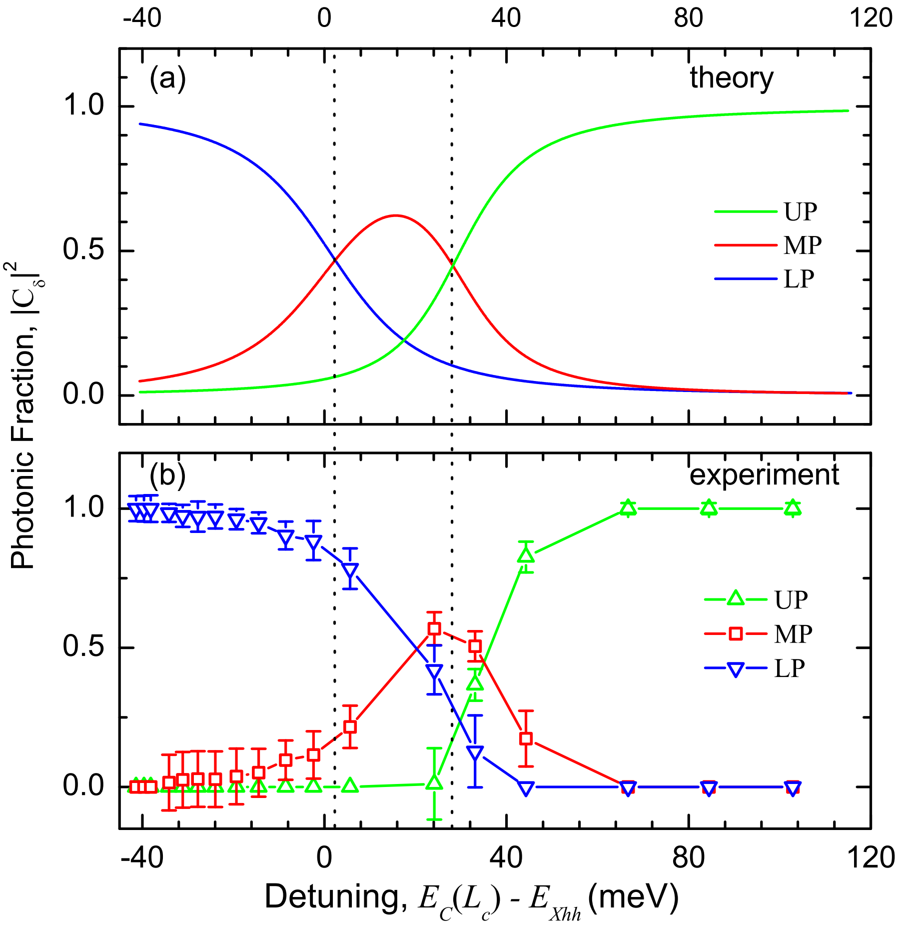

Figure 5.12: (a) Calculated photonic fractions of the upper, middle and lower polariton modes. Analytical expressions from the eigenvectors of the 3 level coupling matrix (5.1) were used with $E_{hh(lh)}$ = 2.601 (2.633) eV and $\hbar\gamma_{hh(lh)}$ = 10.2 (7.5) meV. Dotted lines mark the theoretical intersections. (b) Normalised integrated transmission intensity for the lower, middle and upper polariton states as a function of detuning, δ.

meV. Phonon interactions can therefore explain why the upper polaritons states are generally broader than the energetically lower states.

To understand the origin of the off-resonance behaviour of the cavity polaritons, the simplicity of having only two coupled states is more attractive. For this reason the off-resonance behaviour will be described in momentum space only where coupling to the light hole exciton is not observed. Similar to the translational tuning data, the integrated intensities and full width at half maximum only resembled that which was expected in momentum space. Figure 5.13 (a) presents the dispersion and (b) nor-

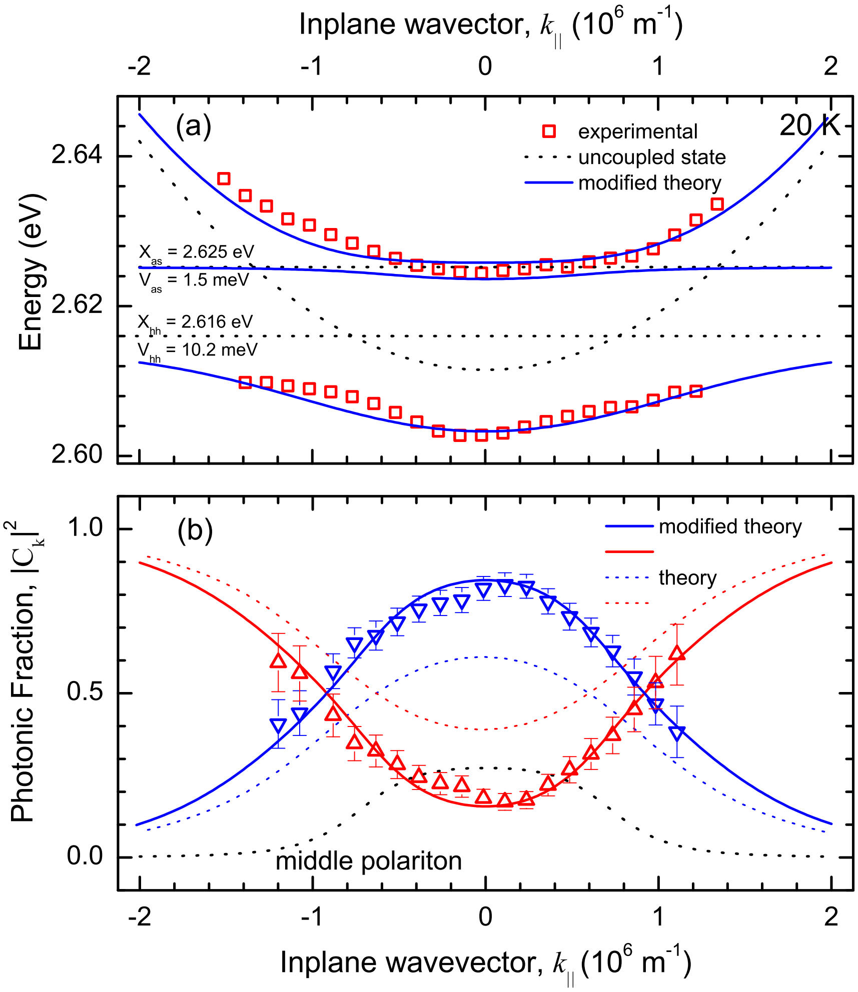

Figure 5.13: (a) Experimental peak values of lower and upper polariton from figure 5.7 (a) along with the 3×3 coupling matrix used to describe the off-resonance behaviour. (b) Off-resonance modeling of the integrated transmission intensity for the fixed microcavity negatively detuned. The experimental data presented is from figure 5.7 (b)

malised integrated intensity for negative detuning. The points of resonance of the heavy hole exciton and cavity photon can be seen in figure 5.13 (a) and clearly do not coincide with the point of equal proportions of the composite states. Following the works of Lidzey *et al.* [54], it is proposed that the off-resonance behaviour is due to spectral asymmetry of the exciton absorption, and that this can be described by introducing a weakly coupled state above the heavy hole exciton. The eigensolutions and eigenvectors of the 3×3 coupling matrix,

$$M_{k_{||}} = \begin{pmatrix} E_c(k_{||}) & \hbar V_{hh} & \hbar V_{as} \\ \hbar V_{hh} & E_{hh}(k_{||}) & 0 \\ \hbar V_{as} & 0 & E_{as}(k_{||}) \end{pmatrix}, \tag{5.4}$$

are presented in figure 5.13 (a) and (b), respectively. The parameters relating to the cavity photon and the heavy hole exciton used in the original fit to the polariton dispersion were used here with the high energy shoulder, E_{as} = 2.625 eV and the coupling strength to the cavity photon, $\hbar V_{as}$ = 1.5 meV as fit parameters ($\hbar V_{hh}$ = 10.2 $\pm$ 0.4 meV, E_{hh} = 2.616 eV and δ = -4.1 meV). The three polariton dispersion curves are presented in figure 5.13 (a) along with the measured dispersion. The upper and lower polariton branches still fit well to the data. The middle polariton from the weakly coupled high energy shoulder, 9 meV above the heavy hole transitions has negligible effect on the quality of the fit and the resulting polariton state is not resolvable in the experimental data. However, the impact is significant on the eigenvectors of the coupling matrix, describing the evolution of the photon fraction of the upper and lower polariton. The coloured dashed lines in figure 5.13 (b) are the eigenvectors from the 2×2 coupling matrix, intersecting at the resonance, clearly insufficient in describing the experimental data. The new eigenvectors from 5.4 are also presented in figure 5.13 (b) (solid lines, the black dotted line corresponds to the middle polariton) and are in excellent agreement with the experimental data, with the intersection point occurring at $k_{||} \sim \pm 1 \times 10^6$ m^{-1} ($\sim$ ± 3°). For small $k_{||}$ the two upper polariton states would be experimentally observed as one and for high $k_{||}$ the photonic fraction of the middle polariton is very small. It is noted that the coupling strength of E_{as} is very weak and is therefore not expected to contributed to the photonic fraction of the upper polariton, otherwise the sum of the simulated photonic fraction of the middle and upper polariton states would be presented.

The calculation of the photonic fraction in momentum space, describing the off-resonance behaviour, was also applied to the translational tuning experiment (figure 5.4 (a)). Since the light hole exciton was observed to couple to the cavity photon, a

$4x4$ coupling matrix was used to account for the three states coupling to the cavity photon. The eigenvectors of the coupling matrix,

$$M_{k_{||}} = \begin{pmatrix} E_c(k_{||}) & \hbar V_{hh} & \hbar V_{as} & \hbar V_{lh} \\ \hbar V_{hh} & E_{hh}(k_{||}) & 0 & 0 \\ \hbar V_{as} & 0 & E_{as}(k_{||}) & 0 \\ \hbar V_{lh} & 0 & 0 & E_{lh}(k_{||}) \end{pmatrix}, \tag{5.5}$$

are presented in figure 5.14 (a) along with the eigenvectors of the $3x3$ coupling matrix, solid and dotted curves, respectively. The parameters used for the 4 level coupling matrix were $E_{hh(as)}$ = 2.595 (2.608) eV, E_{lh} = 2.633, $\hbar\gamma_{hh(as)}$ = 5 (8) meV and $\hbar\gamma_{lh}$ = 7.5. The parameters used for the 3 level coupling matrix are stated in the caption of figure 5.12. From figure 5.14 (a) the lower and middle polariton photonic fractions are predicted to intersect for a detuning of, δ = $+\ 9$ meV above resonance. This does not correspond to the actual intersection point of 20 meV (figure 5.14 (b)). The middle and upper polariton photonic fractions are correctly predicted to intersect for a detuning of, δ = $+\ 35$ meV above resonance. It is not currently understood why the inclusion of the spectral asymmetry of the exciton absorption successfully describes the evolution of the photon fraction in momentum space but not in Euclidean space.

5.2.2 Linewidth narrowing

Narrowing effects of cavity polariton linewidths in microcavities were intensely studied at the end of the 1990s. The effect was first experimentally evidenced in the works of Whittaker *et. al.* [52]. Measuring the sum of full widths at half maximum for two cavity polariton resonances in reflection spectra as a function of incidence angle, the experimentalists found a minimum of this function at the anticrossing of exciton and cavity modes, unpredicted in the framework of the simple model of two coupled oscillators (chapter 2). Clearly, this treatment of the cavity polariton is not a complete picture if, instead of a single free exciton transition, one has a large number of reso-

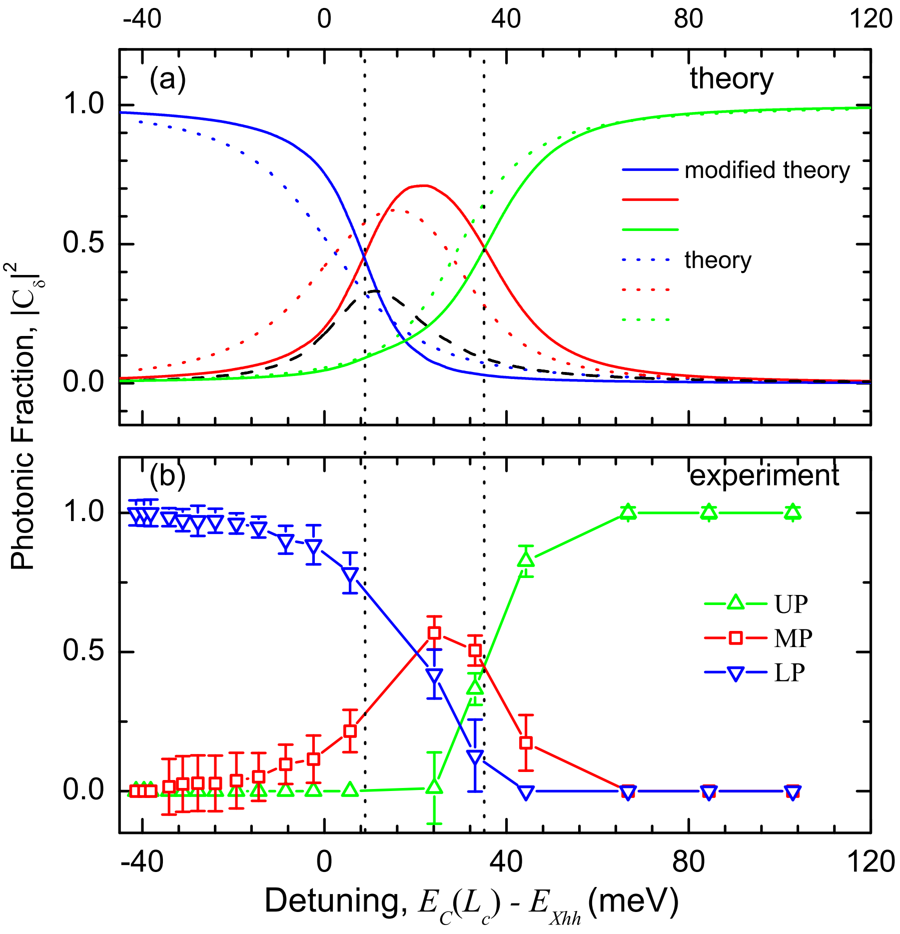

Figure 5.14: (a) (solid curves) Off-resonance calculation for the photonic fractions of the upper, middle and lower polariton modes using the eigenvectors of the 4 level coupling matrix (5.5) with $E_{hh(as)}$ = 2.595 (2.608) eV, E_{lh} = 2.633, $\hbar\gamma_{hh(as)}$ = 5 (8) meV and $\hbar\gamma_{lh}$ = 7.5. Vertical dotted lines mark the off-resonance theoretical intersections. (dotted curves) Analytical expressions from the eigenvectors of the 3 level coupling matrix (5.1) with the same parameters as stated in figure 5.12. (dashed curve) Photonic fraction of the asymmetric component of the heavy hole exciton. (b) Experimental values of the normalised integrated transmission intensity for the lower, middle and upper polariton states as a function of detuning, δ.

nances distributed in energy. This is what happens in realistic quantum wells, where in-plane potential fluctuations caused by the quantum well width and alloy fluctuations induce inhomogeneous broadening of an exciton resonance. The interpretation of the experimental findings was that cavity polaritons, having a smaller effective mass than bare excitons, are less sensitive to the disorder potential. Thus, the inhomogeneous broadening of cavity polariton modes is less than that of a pure exciton state, which is a consequence of the polariton motional narrowing effect. At the anticrossing point this effect is especially strong, since at this point both polaritons are half exciton, half photon. Further analysis [53, 55] has shown, however, that experimentally observed narrowing of polariton lines at the anticrossing point could be caused by exciton inhomogeneous broadening, and possibly by the motional narrowing effect. Motional narrowing is the narrowing of a distribution function of a quantum particle propagating in a disordered medium due to averaging of the disorder potential over the size of the wave-function of a particle. In other words, a quantum particle, which is never localised at a given point in space but always occupies some non-zero volume, has a potential energy that is the average of the potential within this volume. This is why, in a random fluctuation potential, the energy distribution function of a quantum particle is always narrower than the potential distribution function. The reduction in linewidth due to the exciton's finite extension averaging over the disorder potential in single and multiple quantum wells has been calculated and experimentally confirmed by Savona *et al.* [56] and Kocherscheidt *et al.* [57].

The observed narrowing effect in III-V microcavities was later interpreted by Kavokin in the following way [53]. The coupling to light has a different strength for excitons from the centre and from the tails of an inhomogeneous distribution. As the density of states of excitons has a maximum at $E = E_X$, these excitons have the highest radiative recombination rate and the strongest coupling to light. The strong coupling regime holds only for excitons situated in the vicinity of E_X, while the tails remain in the weak-coupling regime. The central part of the excitonic distribution is of course less broadened than the entire distribution. Therefore, the two polariton modes that arise due to its coupling with the cavity photon are also narrower than one would expect for the case of all excitons equally coupled to the cavity photon. At zero detuning, both polariton modes are far enough from the bare exciton energy, so that the tails of the exciton resonance give no contribution to the linewidth of polariton resonances. On the contrary, for strong negative or positive detunings, one of two polariton states almost coincides in energy with a bare exciton state, so that the line shape of the corresponding spectral resonance is necessarily affected by the tails of the excitonic distribution. It is noted that this interpretation does not involve any motional narrowing and that any spectral asymmetry of the exciton absorption will not redistribute the narrowing effect since the maximum exciton oscillator strength will not spectrally shift relative to a symmetric absorption. Another remark made by Kavokin [53] concerns the in-plane wavevector asymmetric behaviour of the broadenings of the two polariton peaks observed in [52]. It was proposed that the spectral asymmetry of the excitonic absorption is the cause of the difference in broadening between the lower and upper polariton. The lower polariton branch is the result of mixing between the photon mode and the lower part of the excitonic distribution, which is sharper than the upper part. This is why the lower branch has a narrower linewidth at the anticrossing condition. This interpretation successfully describes the experimental observing in [52]. However, it does not describe off-resonance narrowing, as observed here.

From figure 5.13 (b) (and 5.7 (a)), equal polariton composite ratio occurs at $k_{||} \sim \pm 1 \times 10^{6}$ m^{-1} ($\sim \pm 3$ °), where the lower polariton linewidth is observed to narrow to a minimum of $\sim$ 7 meV (figure 5.7 (b)), above resonance at $k_{||} \sim \pm 0.65 \times 10^{6}$ m^{-1} ($\sim \pm$ 2.8 °). At $k_{||} \sim \pm 1 \times 10^{6}$ m^{-1} ($\sim \pm$ 3°) the high energy tail of the exciton is overlapping with the low energy tail of the cavity photon distribution. This is clearly represented by Lorentzian curves created using the parameters of the observed spectra presented in figure 5.5 and are presented in figure 5.15. The Lorentzian curves at 2.607 and 2.627 eV correspond to the lower and upper polaritons at $k_{||} \sim \pm 1 \times 10^{6}$ m^{-1} ($\sim \pm$ 3 °), simulated with $\Gamma_{LP(UP)}$ = 7 (13) meV, respectively. Lorentzian curves were also created for the bare exciton (cavity) using peak energies 2.616 (2.622) eV and $\gamma_{hh(c)}$ = 10.1 (15.5) meV. Clearly the bare heavy hole exciton and cavity photon states of the system are not aligned. The interpretation given above, from [53], is therefore not valid since it relies on the alignment of the exciton and cavity photon, leading to an effective filtering of the polariton linewidth. It is proposed that the interpretation first put forward by Whittaker *et al.* [52] is more satisfactory in explaining the narrowing effects

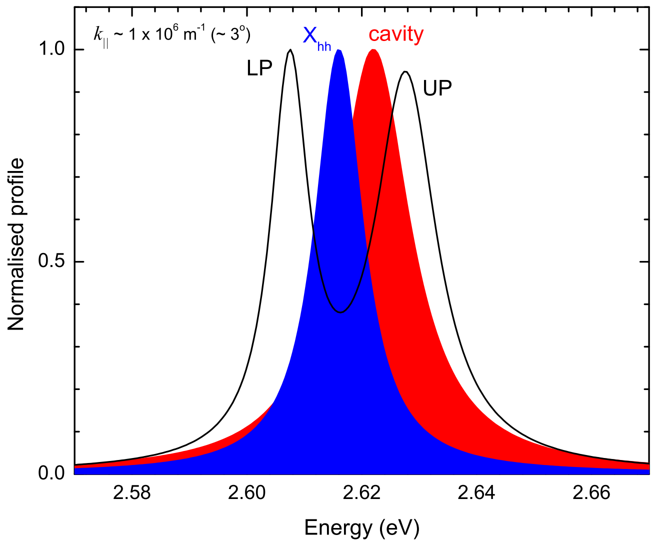

Figure 5.15: Lorentzian curves representing the lower and upper polariton at $k_{||} \sim \pm 1 \times 10^6$ m^{-1} ($\sim \pm$ 3°), where the photonic fractions of the polariton peaks cross in k-space for the fixed microcavity, negatively detuned. Lorentzian curves representing spectral positions of bare heavy hole exciton and cavity photon, deduced from the model highlight the fact that the they are not resonant at the point of narrowing. The polariton curves were created using the parameters, $E_{LP(UP)}$ = 2.607 (2.628) eV and $\Gamma_{LP(UP)}$ = 7 (13) meV, respectively. Lorentzian curves representing the uncoupled states were created using peak energies $E_{X_{hh}(c)}$ = 2.616 (2.622) eV and $\gamma_{hh(c)}$ = 10.1 (15.5) meV.

observed here. The intersection of the composite ratios occurs not on resonance but at $k_{||} \sim \pm 1 \times 10^6$ m^{-1} ($\sim \pm$ 3 °), at which point the polariton is half exciton, half cavity photon. The equality results in the disorder potential seen by the polariton being averaged out due to the decreased effective mass, in other words, the polariton narrows due to motional narrowing of the quantum state.

5.3 Completely tunable microcavity

For the second type of microcavity presented a completely tunable microcavity was fabricated, composed of two identical mirrors externally separated such that the cavity length could be varied with nanometer precision. For a detailed discussion of the tunable microcavity and the experimental procedure see chapter 4 section 4.4. After

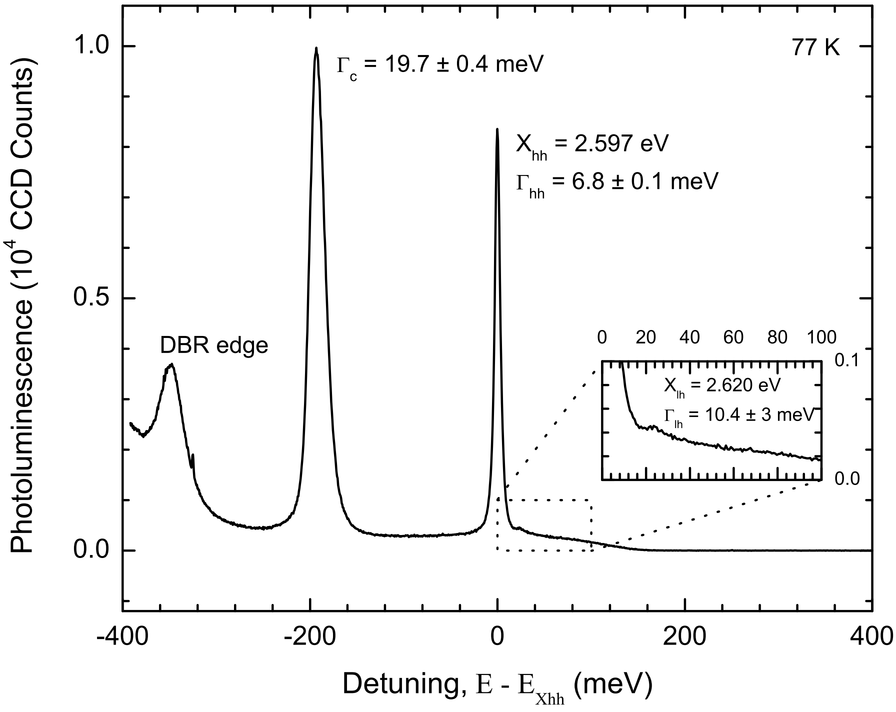

Figure 5.16: Photoluminescence spectrum taken for $\delta = -200$ meV detuning. The inset shows, in detail, the light hole transition. The heavy (light) hole exciton transitions are found to be at 2.597 (2.620) eV with a linewidth of 6.8 ± 0.1 (10.4 ± 3) meV and the cavity linewidth is 19.7 ± 0.4 meV.

fabricating the microcavity the entire experiment was submerged in liquid nitrogen and cooled to 77 K. Since the microcavity was mounted on top of nanopositioners, used for positioning and control of the microcavity, experiments were performed in reflection geometry. Optical measurements were taken using a tungsten bulb for reflection spectroscopy and a GaN laser diode emitting at a wavelength of 400 nm with 10 mW of power (3.2 kW cm^{-2}) for photoluminescence spectroscopy. The optical beam was focused to a 20 μm spot diameter and collected with a single multi-mode fibre (50 μm core), dispersed and detected with a liquid nitrogen cooled charged coupled device.

To measure the uncoupled parameters, γ_c, γ_{hh}, E_{hh}, γ_{lh} and E_{lh}, the microcavity was detuned to ~ 200 meV ensuring the cavity photon and exciton were not coupled. Photoluminescence from the uncoupled microcavity at 77 K is presented in figure 5.16. Three optical features are clearly observed. The data is presented on a detuning scale relative to the heavy hole exciton (2.597 eV). The DBR edge is observed around

-350 meV followed by the uncoupled cavity photon around -200 meV and the heavy hole exciton at 0 meV. The linewidths of the uncoupled cavity and heavy hole exciton were found to be, γ_c = 19.7 ± 0.4 and γ_{hh} = 6.8 ± 0.1 meV, respectively, from Lorentzian curves fitted to the spectrum. The light hole exciton is also observed at 23 ± 3 meV. The inset in figure 5.16 shows a partial part of the spectrum highlighting the photoluminescence from the light hole exciton and as before the linewidth was measured to be 10.4 ± 1.0 meV.

5.3.1 White light reflection spectroscopy

The microcavity was easily detuned by decreasing (increasing) the cavity length (energy) through resonance with the X$_{hh}$ and beyond with ~ 1 nm (~ 5 meV) increments. Figure 5.17 (a) shows a contour plot of the reflection spectra taken for a decreasing cavity length. Note that cavity length is not linear with applied voltage to the nanopositioner. This will be calibrated later. The dip in reflection (indicated by colour red) can be clearly seen to increase in energy with the applied voltage and anticrosses with the heavy (light) hole transitions at 2.597 (2.620) eV. A selection of the spectra is presented in figure 5.17 (b). The anticrossing occurs with a normal mode splitting of 19 meV. Coupling to the light hole exciton is seen at higher energies.

As with the previous experiments, Lorentzian fits were used to extract the peak energy values of the lower, middle and upper polariton. The peak energy values are presented in figure 5.18 (a) along with the eigenvalues of the 3×3 coupling matrix. The nano-positioner used to tune the cavity length is not linear with the applied voltage so to calibrate the detuning, the cavity energy was deduced from the peak energy values using the coupling matrix. The observed spectral splitting in the reflection data for the lower and middle polariton was found to be 19 meV. The spectral splitting between the middle and upper polariton could not be accurately measured due to insufficient

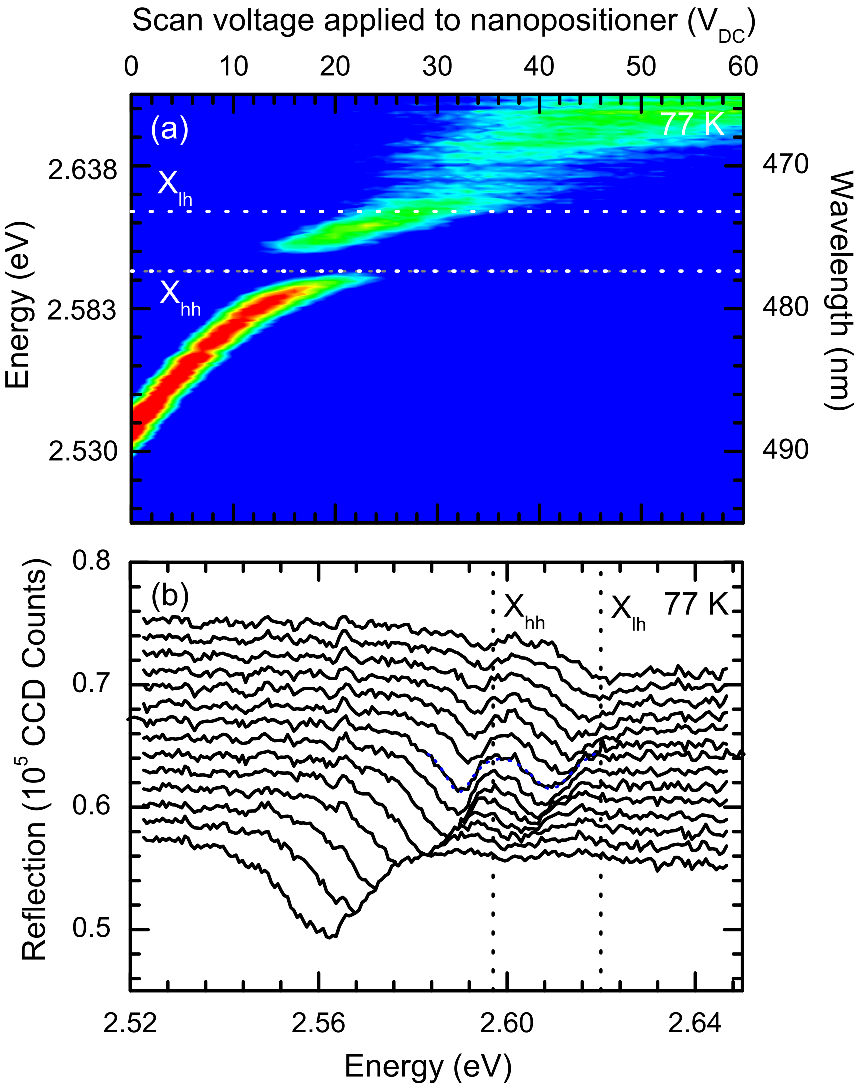

Figure 5.17: (a) Contour plot of the reflection spectra taken for the tunable microcavity. he dip in the reflectivity is indicated by the colour red. The cavity length was decreased in increments of ~ 1 nm (~ 5 meV) (calibration of this will be discussed later) with applied voltage to the nanopositioner. The dashed lines mark the uncoupled heavy and light hole exciton transitions at 2.597 and 2.620 eV, respectively. (b) Reflection spectra for the tunable microcavity. Spectra are offset for clarity. The sample was maintained at a temperature of 77 K.

fits to the spectra for upper polariton. The parameters used for the bare states were measured from the photoluminescence presented in figure 5.16. The best fit was achieved using the fit parameters $\hbar V_{hh(lh)}$ = 10.3 ± 0.4 (7.5 ± 0.8) meV. In the high reflectivity limit, and assuming exciton cavity resonance, an analytic formula for the observable spectral splitting in reflection, $\hbar\Omega_R$ is given by [50],

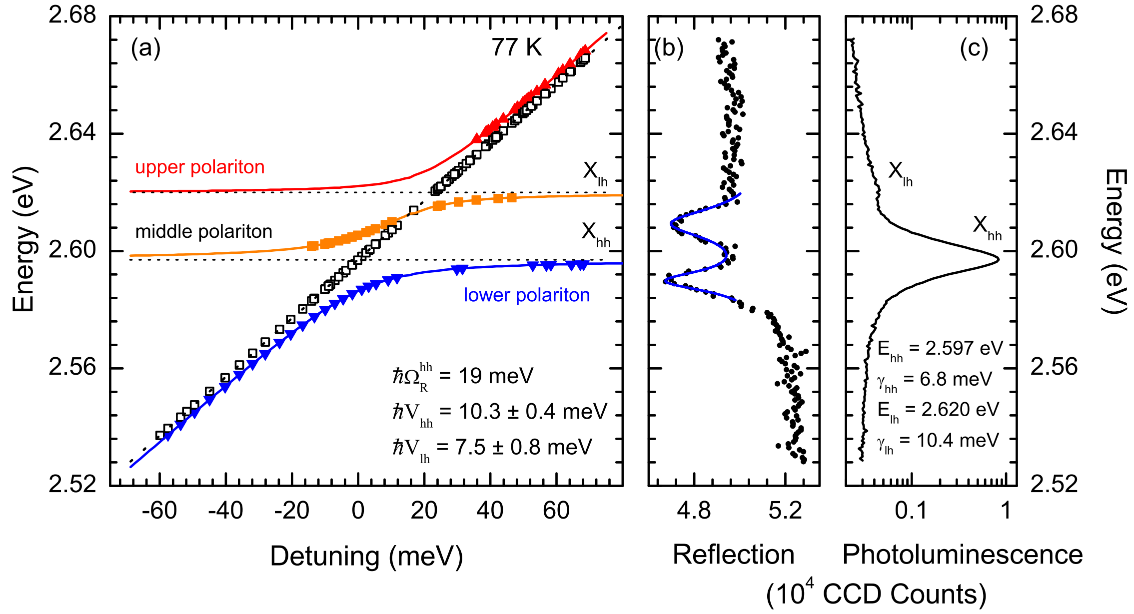

Figure 5.18: (a) Energy peak values from Lorentzian curves fitted to the spectra in figure 5.17. The lower, middle and upper polariton dispersion are marked with blue upward triangles, orange squares and red downward triangles, respectively. The polariton dispersion curves are compared to the model discussed in the text (solid lines). The bare cavity energy was also deduced using the model (open black squares) and used to calibrate the detuning. Resonance occurs with the heavy (light) hole (identified by the dotted lines) with a matrix element $\hbar V_{hh(lh)}$ = 10.3 ± 0.4 (7.5 ± 0.8) meV. (b) Reflection spectrum for resonance with the heavy hole exciton (solid black circles). Lorentzian curves fitted to the spectrum (solid blue line). (c) Photoluminescence spectrum for the bare quantum well evidencing the spectral features of the heavy and light hole excitons. All the data is taken at a sample temperature of 77 K.

$$\hbar\Omega_R^{hh} \simeq 2\sqrt{\sqrt{V^4(1+\frac{2\gamma_{hh}}{\gamma_c})^2 + 2V^2\gamma_{hh}^2(1+\frac{\gamma_{hh}}{\gamma_c})} - 2V^2\frac{\gamma_{hh}}{\gamma_c} - \gamma_{hh}^2}, \tag{5.6}$$

From the photoluminescence of the uncoupled microcavity, $\gamma_{hh(c)}$ = 6.8 ± 0.1 (19.7 ± 0.2) meV (figure 5.16) the expected spectral splitting from the coupled heavy hole exciton and cavity photon can be calculated using the fit parameter, $\hbar V$ = 10.3 ± 0.4, deduced from fitting to the polariton dispersion, and compared to the observed spectral splitting. $\hbar\Omega_R^{hh}$ = 19.4 ± 2.5 meV compares well with the experimental splitting of 19 ± 0.4 meV, further confirming the quality of the fit in figure 5.18 (a).

The full width at half maximum of the lower polariton is presented in figure 5.19. It

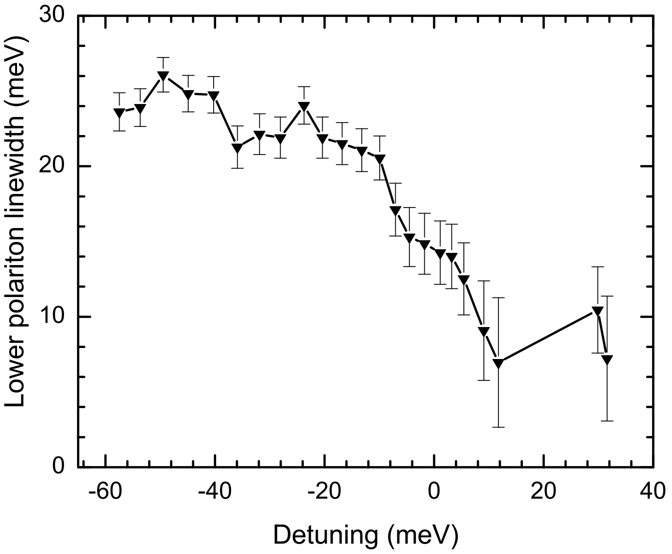

Figure 5.19: Lower polariton linewidth for the tunable microcavity measured from the reflection spectra. Linewidth narrowing is evident and occurs at, δ = $+$ 12 meV, above resonance with the heavy hole exciton. It was not possible to achieve sufficient Lorentzian fits to the middle and upper polaritons due to low signal contrast.

was difficult to measure accurately the linewidths of the middle and upper polaritons which have been omitted for clarity. The same applies to the integrated area of the dip in the reflection. However, figure 5.19 indicates similar off-resonance behaviour observed previously in section 5.2. For the three level system the narrowing of the lower polariton linewidth is expected to occur a few meV above resonance, however, the lower polariton linewidth narrows to 7 ± 4 meV, at δ = $+$ 12 meV, well above resonance with the heavy hole exciton.

5.3.2 Photoluminescence spectroscopy

All of the experimental findings presented so far lie within the linear regime of spectroscopic techniques. At this point it is convenient to briefly discuss the physical processes involved in the generation of photoluminescence and the unique difference between photoluminescence from semiconductor heterostructures and photoluminescence from microcavities. For any semiconductor that is nonresonantly excited the generalised physical processes are as follows:

1. Excitation generates coherent e-h pairs which redistribute in momentum space, losing their initial coherence.
2. At this point the e-h pairs are ‘hot’ and cooling is required before the formation of excitons occurs. Phonon scattering is the mechanism by which the hot carriers can exchange their excess energy with the surrounding lattice, via the emission of optical phonons. During this cooling process the formation of excitons may occur.
3. The excitons can then further cool via interactions with acoustic phonons, until an optical transition becomes possible, typically near the central part of reciprocal space.

The optical emission due to the annihilations of excitons contains information which can be collected and analysed to determine the electronic states of the semiconductor under examination. In a semiconductor the emission of a photon comes from localised states, where the DOS is a maximum, and which are spectrally red shifted relative to absorption states. This means that emitted photons are not reabsorbed in traditional semiconductors. This is not the case for the microcavity since the emission of photons does not come from electronic states but rather from polariton states. The works of Houdré *et al.* [10] clearly evidence this. The dispersion of the lower polariton branch constitutes the uniqueness of microcavity physics whilst also being the source of a key obstacle in the drive toward polariton based devices. The polariton trap at the centre of the dispersion curve, where a polariton condensate can form due to the hybridisation, is often less populated than expected due the large photonic fraction in this region and therefore short lifetimes. This effect results in a build up of polariton states at the anticrossing point on the lower polariton dispersion curve. Subsequently emission from microcavities is often maximum at this point. This kinetic limitation in the relaxation process along the dispersion curve is referred to as the bottleneck effect. In chapter 6 the bottleneck effect will be discussed in more detail. In the remainder of this chapter the photoluminescence collected from the tunable microcavity will be presented.

Photoluminescence measurements were taken from the same lateral spot on the sample and for the same detuning range. The sample was excited with a continuous wave excitation density of 3.2 kW cm^{-2} focused to a spot diameter of 20 μm.

Figure 5.20 (a) presents the collected photoluminescence as a contour plot where red in the colour scale represents high photoluminescence intensity and blue, low intensity. For clarity, each spectrum has been individually normalised such that the evolution of the energetic peaks can be clearly viewed. The data is presented as a function of scan voltage applied to the nanopositioner. For scan voltages below 10 V the prominent peak lies along the bare heavy hole exciton transition, indicated by the dotted line. For zero applied voltage, a second peak at 2.53 eV with lower intensity increases in energy with applied voltage and is attributed to the cavity mode. As the cavity mode approaches resonance with the heavy hole exciton at 11 V, a splitting of, $\hbar\Omega_{PL}$ = 11 ± 0.2 meV is observed. As expected, the splitting observed here is lower than the spectral splitting observed in the white light reflection experiment discussed in section 5.3.1 [50]. The original spectra are presented in figure 5.20 (b).

The evolution of the polariton peaks, extracted from figure 5.20(b), is presented in figure 5.21 (a). A clear demonstration of anticrossing of the cavity mode and heavy hole exciton is evident. The bare exciton transition at 2.587 eV is marked with a dotted line. As before, the cavity mode energy was deduced from the actual polariton peaks using the coupling matrix and is presented as open black squares in figure 5.21 (a). The solutions to the coupling matrix are also presented along with the polariton peaks and give an excellent fit, with fit parameter, $\hbar\Omega_{PL}$ = 11 ± 0.8 meV which corresponds

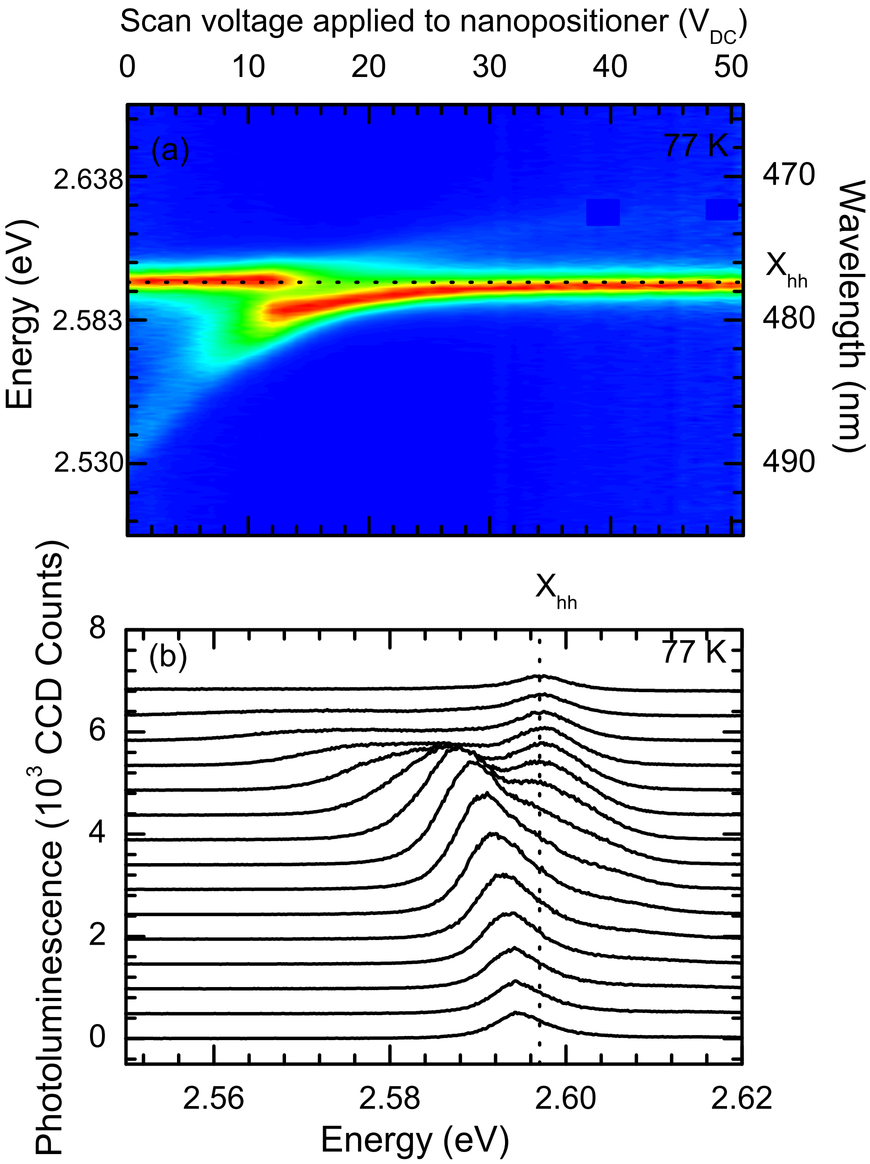

Figure 5.20: (a) Contour plot of the photoluminescence spectra from the tunable microcavity as a function of the applied voltage to the nanopositioner. The colour map relates to the photoluminescence intensity with red indicating high intensity. The spectra have been individually normalised for clarity. (b) Photoluminescence spectra for the same detuning as in (a). Spectra are offset for clarity.

to a coupling constant, $\hbar V$ = 10.3 ± 0.4 meV. The photoluminescence spectrum (solid black line) corresponding to zero detuning is presented in figure 5.21 (b) along with fitted Lorentzian curves (dotted colour lines). The spectral splitting is not immediately obvious due to the low splitting-linewidth ratio ($\frac{\hbar\Omega_{PL}}{\Gamma_{LP}} \sim 1$). The lower polariton peak is at 2.591 eV, 11 meV below the upper polariton peak at 2.602 eV.

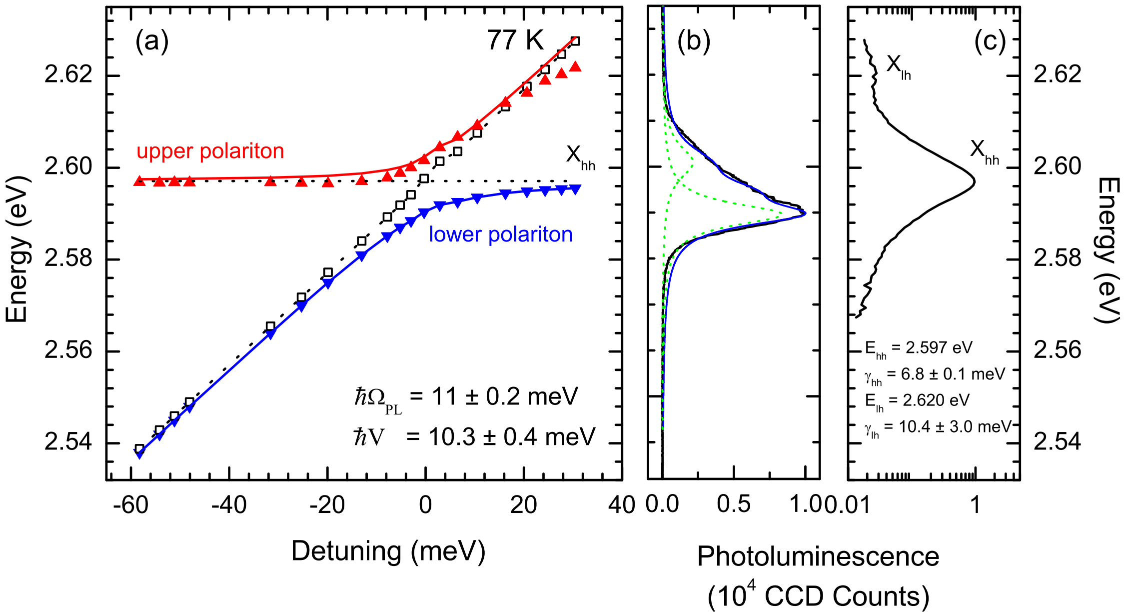

Figure 5.21: (a) Peak values extracted from the photoluminescence spectra for the tunable microcavity presented in figure 5.20(b). (b) Photoluminescence spectrum on resonance with a spectral splitting of 11 meV. (c) Bare quantum well photoluminescence.

As discussed in the context of the transmission and reflection experiments, the observed spectral splitting is dependent of the type of spectroscopy used to measure it. For photoluminescence experiments the observable spectral splitting, $\hbar\Omega_{PL}$ is related to the actual normal mode splitting, $\hbar\Omega$ (equation (2.28)) and is given by [50],

$$\hbar\Omega_{PL} \simeq \sqrt{2\hbar\Omega\sqrt{(\hbar\Omega)^2 + 4\Gamma^2} - (\hbar\Omega)^2 - 4\Gamma^2}, \qquad (5.7)$$

where $\Gamma = \frac{\gamma_X + \gamma_c}{2}$. All the spectral splitting expressions for transmission, $\hbar\Omega_T$ (5.2), reflection, $\hbar\Omega_R$ (5.6) and photoluminescence, $\hbar\Omega_{PL}$ (5.7) are presented in figure 5.22 along with the actual normal mode splitting, $\hbar\Omega$ (2.28). For each of the expressions $\hbar V$ = 10.3 ± 0.4 meV. The data points marked with closed circles are the observed spectral splittings measured for the tunable microcavity from reflection and photoluminescence spectra and fit well with the respective expressions with fit parameter, γ_c = 18.2 ± 0.4 meV. This is slightly lower that the cavity linewidth, γ_c = 19.7 ± 0.4 meV,

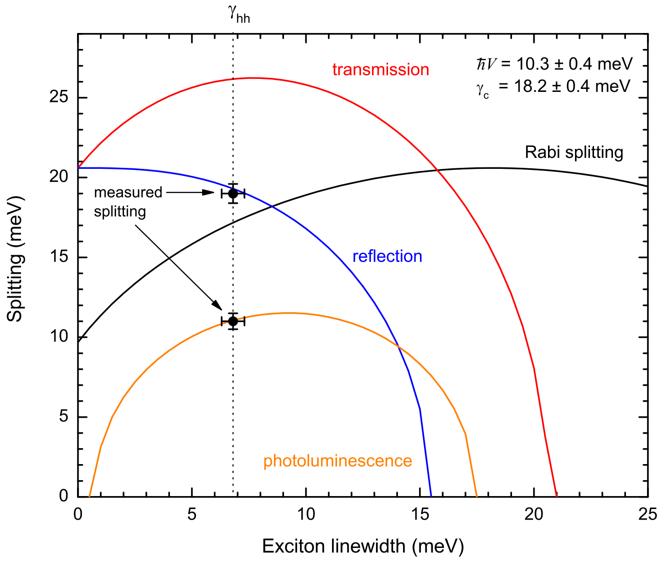

Figure 5.22: Calculated spectral splitting for transmission, $\hbar\Omega_T$ (5.2), reflection, $\hbar\Omega_R$ (5.6) and photoluminescence, $\hbar\Omega_{PL}$ (5.7) experiments along with the Rabi splitting. $\hbar\Omega$ (2.28). For each of the expression $\hbar V$ = 10.3 ± 0.4 meV. The closed circles mark the observed spectral splitting measured for the tunable microcavity from reflection and photoluminescence spectra and fit well with the respective expressions for γ_c = 18.2 ± 0.4 meV.

measured from the uncoupled photoluminescence (figure 5.16). This is attributed to a drop in mirror reflectivity near the stopband edge, where γ_c was measured.

From the Lorentzian fits to the photoluminescence spectra the polariton linewidth and normalised integrated intensity are presented in figures 5.23 (a) and (b), respectively. For negative detuning below -7 meV the point of resonance between the exciton and cavity photon in momentum space is beyond the angular range of the $\times\ 10$ microscope objective ($\sim \pm$ 4° with a 3 mm aperture) and collected photoluminescence is from the central photonic-like part of lower polariton dispersion curve. The drop in photoluminescence intensity for negative detuning is due to the lower polaritons' large photonic fraction in this region limiting relaxation into the polariton trap which is then less populated. In the detuning region $-7 < \delta < 0$ meV the anticrossing region, and thus the bottleneck region, is within the collection angle of the objective lens. The integrated intensity of the photoluminescence from the lower polariton reaches a maximum at δ = -5 meV. For this detuning the bottleneck will be emitting at an angle of $\sim$ 4° normal to the microcavity, within the collection angle of the objective lens. This is an indication of a population build up of cavity polaritons at the bottleneck region. For positive detuning the composite states of the polariton do not intersect in momentum space. This reduces the characteristic transition from excitonic-like to photonic-like dispersion on the lower polariton dispersion curve. From figure 5.23 (a) the bottleneck effect clearly decreases for positive detunings. The decrease in bottleneck emission for increasing detuning, observed here, is supported by the experimental findings of Müller *et al.* [58] for their CdTe based microcavity and Stokker-Cheregi *et al.* [59] for their bulk GaN microcavity. The lower polariton dispersion as a function of detuning is presented in figure 5.23 (a) (inset). The size of the data point represents the integrated intensity.

Figure 5.23 (b) presents the full width at half maximum of the lower (downward triangles) and upper (upward triangles) polariton for the same range of detuning as figure 5.23 (a). For negative detunings $-7<\delta<0$ meV the lower polariton linewidth abruptly decreases to a minimum of Γ_{LP} = 6.4 ± 0.6 meV at δ = 0. The interpretation, presented here, of the observed narrowing is based on the following key point:

1. In the detuning experiments presented here the collected optical information is spread in k-space due to the numerical aperture of the objective lens ($\sim$ 4°).
2. The off-resonance behaviour observed in transmission experiments (section 5.1) is not expected here since the smaller spectral splitting means that the upper polariton will interact less with the high energy tail of the asymmetric exciton absorption.
3. Narrowing effects are then expected to occur at points of resonance in k-space.

The experimental observation is that the lower polariton reaches a minimum linewidth at δ = 0 and that the linewidth is then constant for positive detuning. This indicates that when the bottleneck region is emitting at oblique angles ($k \neq 0$) the polariton

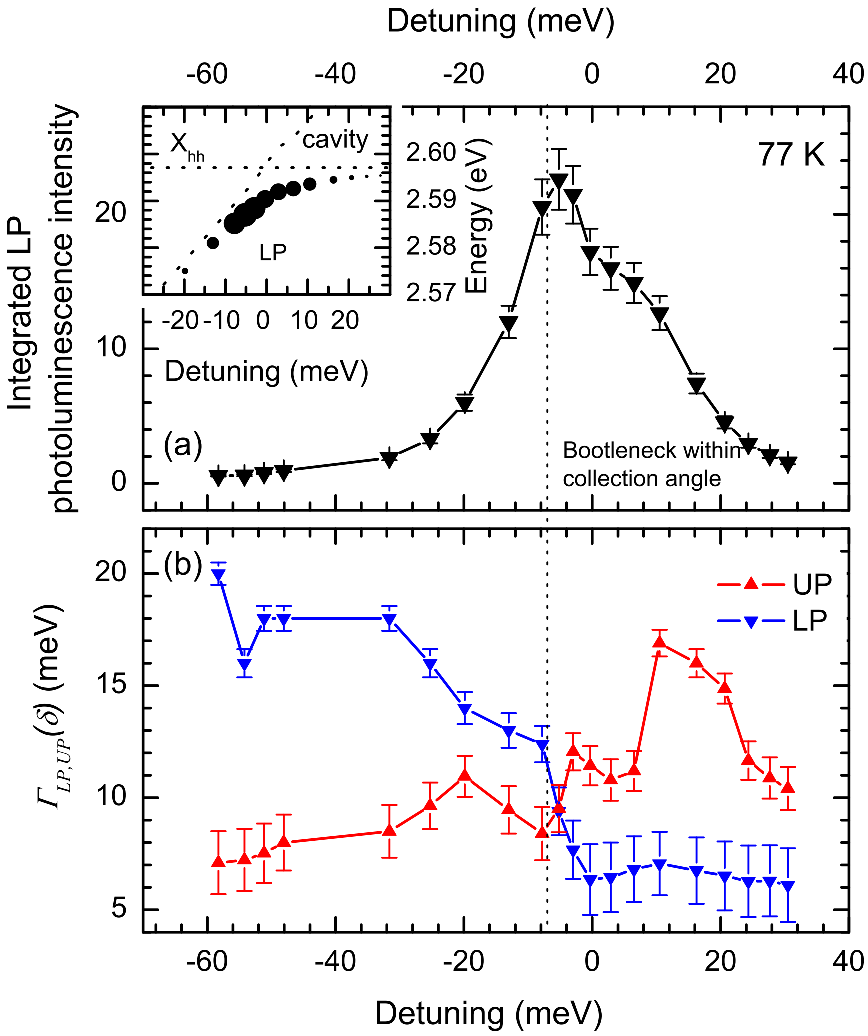

Figure 5.23: (a) Integrated intensity of the lower polariton measured from the photoluminescence spectra presented in figure 5.20. The integrated intensity is a maximum at $\delta = -5$ meV, evidencing increased population of polaritons in the bottleneck region. (b) Lower and upper polariton linewidths. The lower polariton clearly narrows on resonance with the heavy hole exciton.

population is still experiencing some broadening effects. The cause of the broadening is minimised when the exciton and photon dispersion curves no longer intersect in k-space. The experimental observations here suggest that the bottleneck effect can be suppressed (by how much is inconclusive) by conducting future experimental works with ZnSe based microcavities positively detuned.

Chapter 6

Nonlinear exciton-photon hybridisation

Exciton photon hybridisation, resulting in the formation of cavity polaritons, has been discussed in the linear regime, where the polariton state was demonstrated via an anticrossing in k-space, in chapter 5. In section 5.3.2 the normalised integrated intensity of photoluminescence as a function of the cavity length was presented giving the first indication of the bottleneck effect in the ZnSe based material system. In this chapter, observations in the nonlinear regime are presented. Further evidence of the cavity polariton bottleneck in the ZnSe material system is presented in section 6.1. The bottleneck arises from phonon cooling of the polariton from hot states. As this mechanism evolves, the system approaches the photonic-like dispersion on the lower dispersion curve at which point the quanta of momentum that can be released is reduced, a consequence of energy-momentum conservation, resulting in a population 'traffic jam'. This is the bottleneck effect. In addition, the observation of off-branch dispersion is presented, possibly arising from a coherent population in the bottleneck. Finally, the emission from a monolithic microcavity is shown to behave superlinearly at room temperature as a function of exciton power. In all the observations presented in this chapter, the samples were probed using non-resonant excitation.

6.1 Cavity polariton bottleneck & off-branch scattering

In this section the angle resolved nonresonant photoluminescence is presented for the same fixed microcavity discussed in chapter 5 section 5.1, detuned to -34 meV. The sample was optically excited with a continuous wave GaN laser diode, emitting at a wavelength of 400 nm (3.1 eV) and an estimated power of 10 mW (3.2 kW cm^{-2}) at the sample. The excitation was focused to a spot diameter of ~ 20 μm. The experimental cooling and optical detection was performed as described in figure 4.4. The sample was cooled to 20 K.

6.1.1 Polariton bottleneck

The laser excitation creates e-h pairs in the quantum wells, 0.5 eV above the uncoupled heavy hole exciton. As discussed in the chapter 5 section 5.3.2 the e-h pairs relax via optical phonon interaction, followed by acoustic phonon assisted cooling to form polariton states where the excitation laser coherence is completely lost. Figure 6.1 presents a series of spectra on a logarithmic scale, starting with emission normal to the sample (θ_{em} = 0 °) (red line), to just above resonance (E_X = E_c), at (θ_{em} = 5.4 °) (blue line). The normal emission clearly exhibits three spectral features, the lower polariton at 2.574 eV and two peaks at 2.603 eV and 2.609 eV. The latter is attributed to uncoupled heavy hole exciton. The energy, linewidth and integrated intensity of this peak have very flat dispersions. Photoluminescence of the uncoupled quantum wells is presented along with the data, taken for large positive detuning, ensuring the cavity photon and exciton were uncoupled. The unidentified peak at 2.603 eV has little energetic dispersion, however the intensity clearly increases as resonance is approached.

To understand further the observed optical features, the spectra from figure 6.1 are presented in figure 6.2 (a) as a contour plot, showing both positive and negative k-space. The intensity of the photoluminescence is represented by a colour map. Blue indicates low intensity through to red for high intensity. The intensity is on a logarithmic scale. The intensity increases by $\sim$ 2 orders of magnitude, indicated by the red spots at the point of anticrossing on the lower dispersion curve, around $k_{||}$ = $\pm$ 1.5 $\times$ 10^6 m^{-1}. Using the coupling matrix element, $\hbar V_{hh}$ = 10.1 ± 0.4 meV deduced in chapter

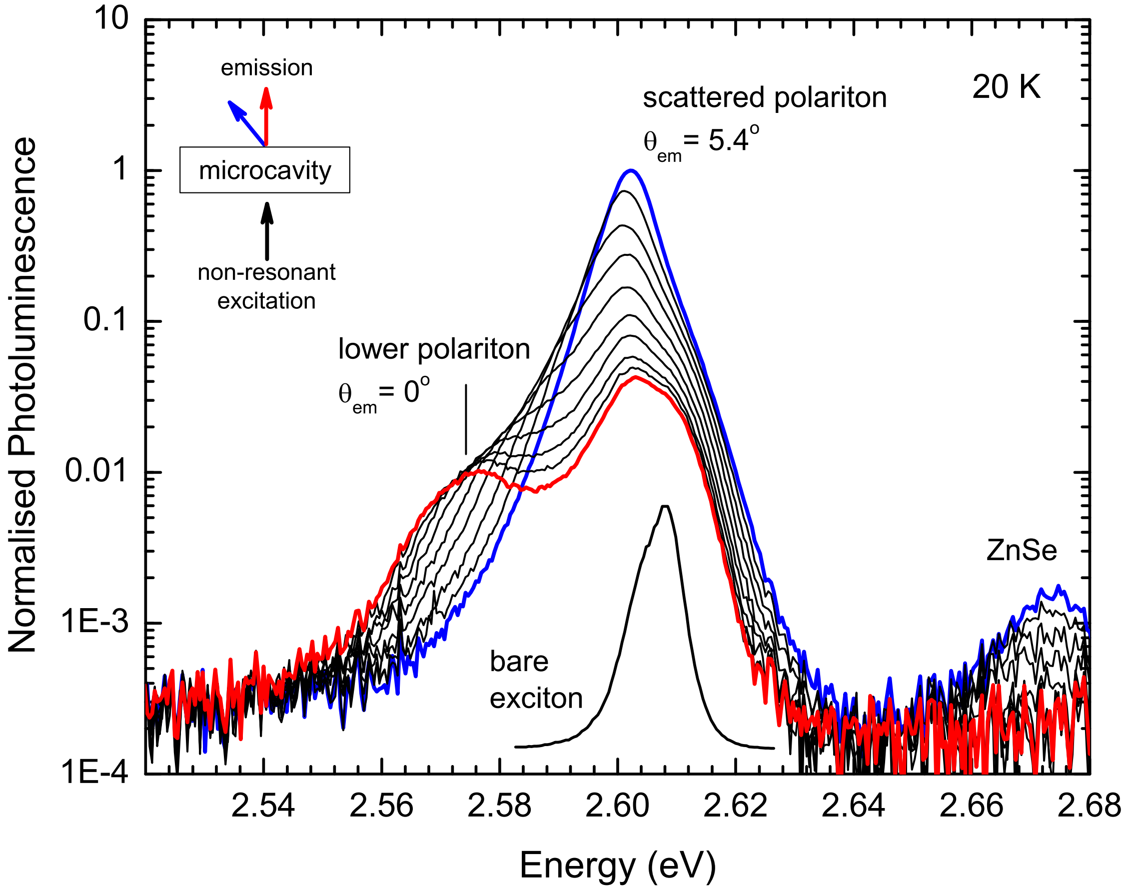

Figure 6.1: Photoluminescence spectra for the fixed microcavity (see chapter 5 section 4.2). Emission normal to the sample ($\theta_{em} = 0\ °$) is highlighted in red. The other spectra correspond to oblique emission up to just above resonance ($E_X = E_c$), at ($\theta_{em} = 5.4\ °$) (blue line). The normal emission clearly exhibits three spectral features, the lower polariton at 2.574 eV, an off-branch peak at 2.603 eV and the uncoupled exciton at 2.609 eV. Completely uncoupled photoluminescence spectrum is presented at the bottom of the graph.

5 (figure 5.6) and the cavity and exciton linewidths, $\gamma_{c(X)} = 15.5 \pm 0.3\ (10.1 \pm 0.2)$ meV, respectively (figure 4.5), the dispersion curves for the upper and lower polariton were calculated using the detuning, δ as fit parameter. The best fit was achieved for $\delta = -\ 34$ meV. The simulation is presented as solid white curves along with the uncoupled cavity and exciton dispersion (dotted white). Lorentzian curves were fitted to the spectra in figure 6.1 and the energetic peaks are presented in figure 6.2 (b) along with the simulated lower polariton dispersion (solid), and uncoupled cavity and exciton (dotted). The excellent fit to the lower polariton dispersion confirms that the observed behaviour falls within the strong coupling regime and that the observed increase in

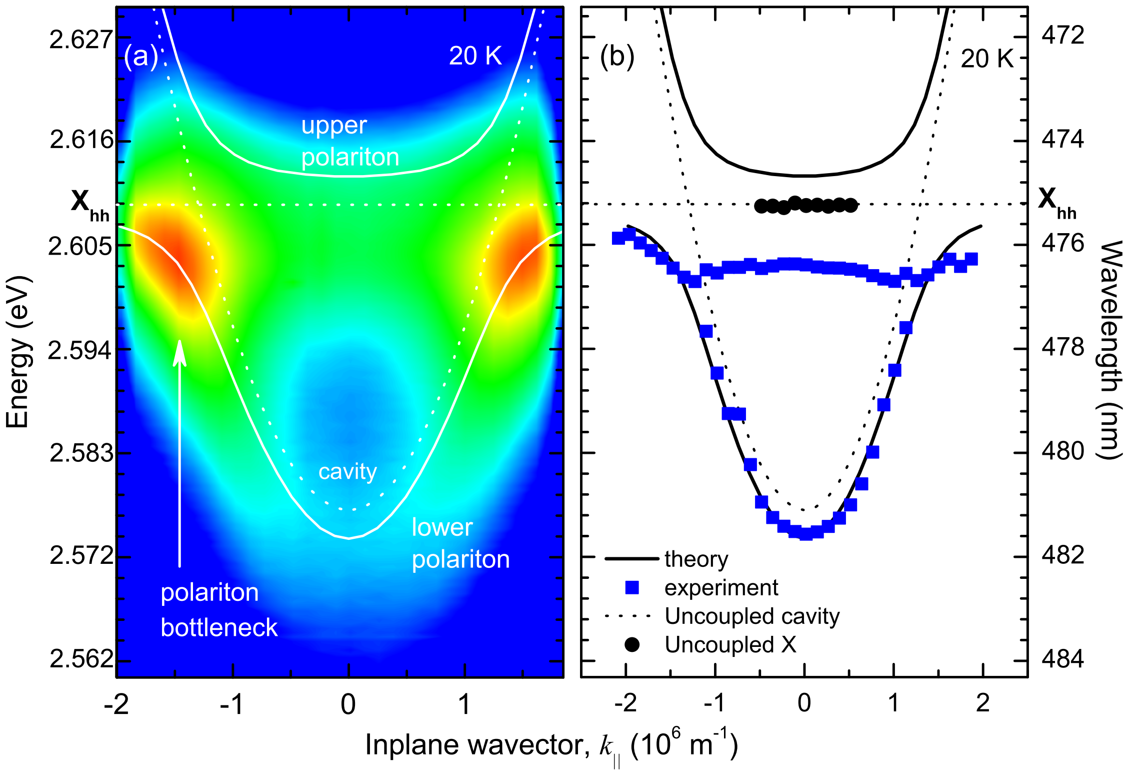

Figure 6.2: (a) Contour plot of the angle resolved photoluminescence spectra presented in figure 6.1. Using the coupling matrix element, $\hbar V_{hh}$ = 10.1 ± 0.4 meV and the cavity and exciton linewidths, $\gamma_{c(X)}$ = 15.5 ± 0.3 (10.1 ± 0.2) meV, respectively, the dispersion curves for the upper and lower polariton were calculated using the detuning, δ = $-$ 34 meV as fit parameter (solid white curves) along with the uncoupled cavity and exciton dispersion (dotted white). The contour scale is logarithmic with blue (red) corresponding to 1 (5×10^4) CCD count(s). (b) Lorentzian curves were fitted to the spectra in figure 6.1 (blue squares) along with the simulated lower polariton dispersion (solid lines), and uncoupled cavity and exciton (dotted lines).

the photoluminescence is due to polariton population build up at the bottleneck. Since the observations are in the strong coupling regime they can not be explained in the frame work of weak coupling lasing mechanisms.

The interpretation of the data is as follows. The e-h gas injected by the excitation source cools to from polaritons with large kinetic energy, which populate the entire dispersion curve via phonon emission. At the point of resonance between the cavity photon and exciton, the lower polariton dispersion makes a transition from excitonic-like to photonic-like dispersion, resulting in a relaxation edge in the polariton dispersion, where polariton densities build up, increasing the probability of the annihilation of a polariton and the emission of the observed photon. The abrupt increase in the photoluminescence is attributed to this polariton build up which marks the bottleneck region in k-space.

The preliminary works presented in this section are very encouraging. The observed increase in photoluminescence at the bottleneck region indicates large coherent polariton populations are achievable in the ZnSe material system. The completion of a rigorous excitation power dependent angle resolved photoluminescence experiment will complete the current understanding of the spectral evolution of coherent polariton populations in ZnSe based microcavities. In addition, the spatial evolution of polariton emission, using micro-photoluminescence, would also be informative.

6.1.2 Off-branch dispersion

The peak at around 2.603 eV significantly deviates from the polariton dispersion. The presence of the uncoupled heavy hole exciton at 2.609 eV, observed around k = $\pm\ 0.5 \times 10^6$ m^{-1} evidences the uniqueness of the peak spanning the two bottleneck regions, clearly presented in figure 6.2 (b). The origins of the unidentified peak are not fully understood. A possible explanation is that the off-branch dispersion originates from polariton-polariton scattering events with the highly populated bottleneck region. This is discussed further in the following section. This is then followed by a discussion of uncoupled localised excitons emitting due to the nonuniform excitation spot.

Polariton-polariton scattering

Polariton-polariton scattering, giving rise to the off-branch polariton dispersion curve has been extensively studied in the III-V material system using resonant pump-probe experiments [60, 61, 62]. The theoretical discussions presented by Ciuti *et al.* [60, 61] describe the experimental observation when a microcavity is resonantly excited with a spectrally narrow source such that scattering events within the populated region result in a signal polariton with zero momentum and an idler polariton with twice the momentum of the populated state. For injection of large polariton populations with momentum corresponding to such a scattering event, the lower dispersion curve was found to blue shift [62] and was successfully described by considering coherent polariton-polariton scattering originating from the injected coherent polariton population. Elastic scattering of polaritons, originating from the injected population was found to be spectrally degenerate with the pump energy [62]. It could be considered that the explanation for this breaking in momentum conservation (but not energy conservation) is Rayleigh scattering due to in-plane disorder. However, the existence of the dispersive lower polariton suggests that this is not the case, since the scattering magnitude would have to be dependent on the population because only the densely populated region is effected.

Following from [62], the off-branch dispersion may originate from coherent collisions within the highly populated bottleneck region. The significance here is that any coherence in the densely populated region would be inherent to the ZnSe polaritons and not a consequence of the excitation since inherited coherence from the excitation is lost during the formation of cavity polaritons. Under non-resonant excitation, off-branch polaritons have been observed in the II-VI material system, namely CdTe [63].

Figure 6.3 (a) presents the dispersion as a scatter plot with the circle size indicating the logarithmic integrated intensity of the measured peak. Clearly the population of the scattered polariton decreases toward $k_{||} = 0$, further suggesting that Rayleigh scattering is unlikely to be the source of the off-branch dispersion. The lower polariton and uncoupled exciton have near constant intensities in k-space. The bottleneck regions are readily identified by the large increase in the integrated intensities around $k_{||} = \pm$

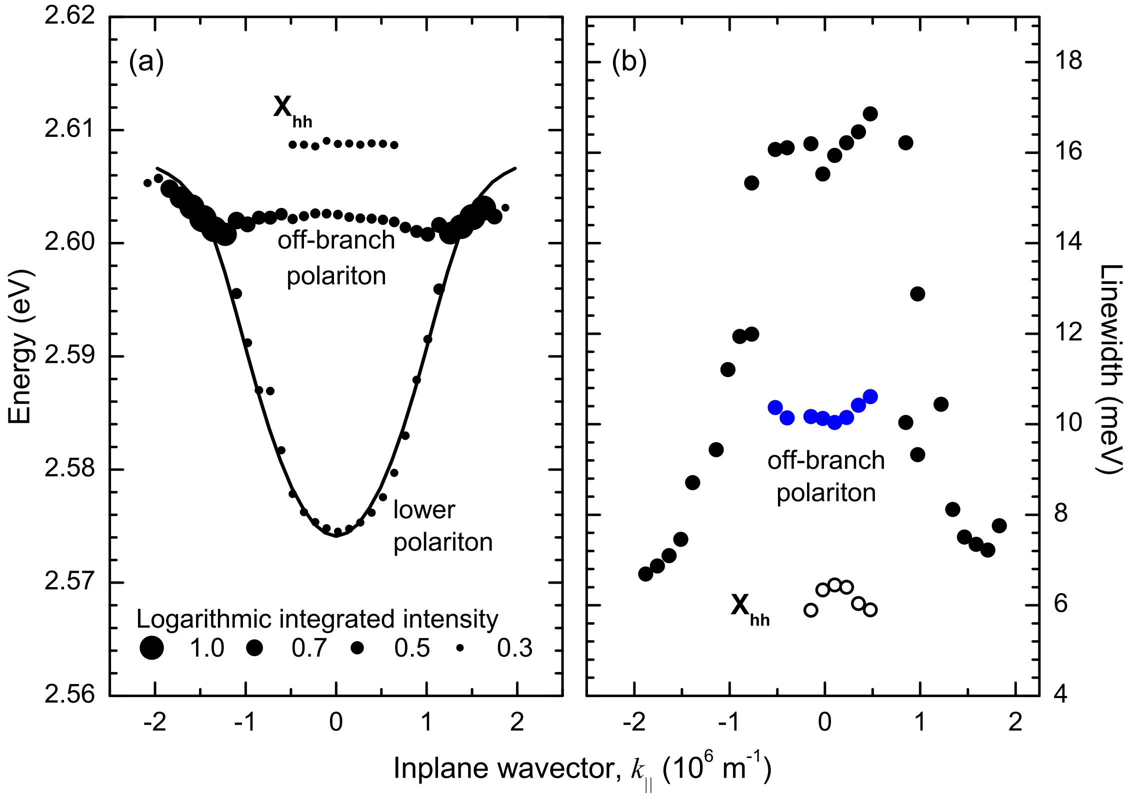

Figure 6.3: (a) Dispersion as a scatter plot with the circle size indicating the logarithmic integrated intensity of the measured peak. (b) Measured linewidth of the lower polariton along with the off-branch dispersion and uncoupled heavy hole exciton.

1.5×10^6 m^{-1}. For coherent collisions, the high density of polaritons gives rise to the flattened, off-branch dispersion, the extent of which in k-space is dependent on the strength of polariton-polariton interaction. The interaction strength can be measured from the separation between the ground lower and off-branch dispersion at $k_{||}$ = 0. From figure 6.2 (b) the polariton-polariton interaction strength, $V^{p-p}_{k=0}$ is found to be $\sim$ 34 meV. Comparing this to the model from [60, 61],

$$V^{p-p}_{k} = \frac{6e^2 a_B X^8_{k_b}}{\epsilon A}\langle p_{k_b}\rangle, \tag{6.1}$$

where X_{k_b}, a_B and A are, respectively, the Hopfield coefficient at the bottleneck, the effective two dimensional exciton radius (a_B = 3.5 nm here) and the in-plane quantization area taken to be the excitation spot size ($\pi 10 \mu m^2$). Applying (6.1) to the experiment here, the average coherent population in the bottleneck is estimated to be, $\langle p_{k_b}\rangle$ $\sim$ 4 $\times$ 10^6. This is a very large population of coherent polaritons. A coherent polariton population of 10^5 has been reported by Richard *et al.* [63] for a CdTe microcavity with $V^{p-p}_{k=0}$ = 1.5 meV. The experimental findings in [63] indicate that $\langle p_{k_b}\rangle$ = 10^5 is larger than expected for their excitation regime and that the observed the polariton-polariton interaction, $V^{p-p}_{k=0}$ = 1.5 meV could not be increased for their material system.

The measured linewidth of the lower polariton along with the off-branch peak and the uncoupled heavy hole exciton are presented in figure 6.3 (b). The linewidths of the off-branch peak and heavy hole exciton are quite constant, whereas the lower polariton is broadest at k = 0 and narrows significantly as the bottleneck region is approached at $k_{||}$ $\sim$ $\pm$ 1.5×10^6 m^{-1}. The point of anticrossing is near the edges of the viewing angle of the objective lens used to collect the photoluminescence and therefore little can be said about the behaviour beyond $k_{||}$ = $\pm$ 1.5×10^6 m^{-1}.

Uncoupled localised excitons

The highly populated bottleneck regions appear to give rise to the off-branch dispersion, however, the off-branch peak may originate from uncoupled localised excitons [64, 65, 58]. The presence of weak and strong coupling can be understood by considering the nonuniform distribution of the excitation spot. In regions of high power density the excitons will be completely ionized, switching the microcavity into the weak coupling regime where the uncoupled free and localised excitons are observed. The region of highest power density in the excitation spot is assumed to be at the centre of the spot. At the spot edge the power density will be lower, such that the microcavity continues to operate in the strong coupling regime where the lower polariton is observed. Simultaneous observations of weak and strong coupling have been reported by Le Si Dang *et al.* [17] and Müller *et al.* [58].

It is noted that the experimental observations presented here are not complete and a conclusion to the origin of the peak around 2.603 eV can not be made. Polariton-polariton scattering from the bottleneck region is very power dependent (equation (6.1)) and can therefore be readily tested with a power dependent angle resolved photoluminescence experiment. Additionally, the presence of uncoupled localised excitons would be confirmed with a power dependence experiment. Since the the lifetime of uncoupled localised exciton is slower than the uncoupled free exciton, a time resolved photoluminescence experiment would also be beneficial in identifying the unknown off-branch dispersion.

6.2 Room temperature hybridisation

As discussed in the introduction to this thesis (chapter 1), the drive in developing and optimising the vertical cavity surface emitting laser led to the first demonstration of strong light matter hybridisation in a solid state environment [3]. The drive in developing and optimising the strong light matter hybridisation presented in this thesis, led to the first room temperature demonstration of a ZnSe based vertical cavity surface emitting laser fabricated using the epitaxial liftoff technology. Having successfully observed cavity polaritons in the fixed microcavity, the alternative method of coating the second mirror onto the microcavity was introduced so as to reduce the damaging impact of trapped dust particles and to reduce the cavity mode volume. Although not a direct goal of the project, it is expected that the use of a metallic mirror will improve the heat management of the device, greatly improving the life time of the device. In chapter 4 section 4.3 the fabrication of a monolithic hybrid ZnSe based microcavity was discussed. It was found that the exciton transitions in all the monolithic microcavities fabricated were energetically out of reach of the cavity photon at cryogenic temperatures. Although the cavity polariton was not observed in the monolithic microcavity an interaction between the electric field and exciton can still exist. Probing the samples at room temperature led to the observation of population inversion, a traditional lasing mechanism in semiconductor devices.

The monolithic microcavities were probed at room temperature using the experimental setup described in chapter 4, figure 4.4. An optical parametric amplifier, emitting with an energy of ~ 2.1 μJ per pulse (2.1 mW average power), with an estimated pulse width of ~ 200 fs at a rep rate of 1 kHz was used to inject quantified doses of e-h pairs into the microcavity. The excitation was focused to a diffraction limited spot diameter of 20 μm at the sample. The corresponding (average power) energy density per pulse is 175 mJ cm^{-2} (175 W cm^{-2}). The output of the optical parametric amplifier was at a wavelength of 400 nm (3.1 eV).

Figure 6.4 shows the broadband transmission of the bare quantum wells at 300 K (top spectrum). The heavy hole exciton transition is estimated to be at 2.556 ± 0.1 eV. Above this is the ZnSe bulk exciton transition at 2.72 eV. The epilayer thickness is es-

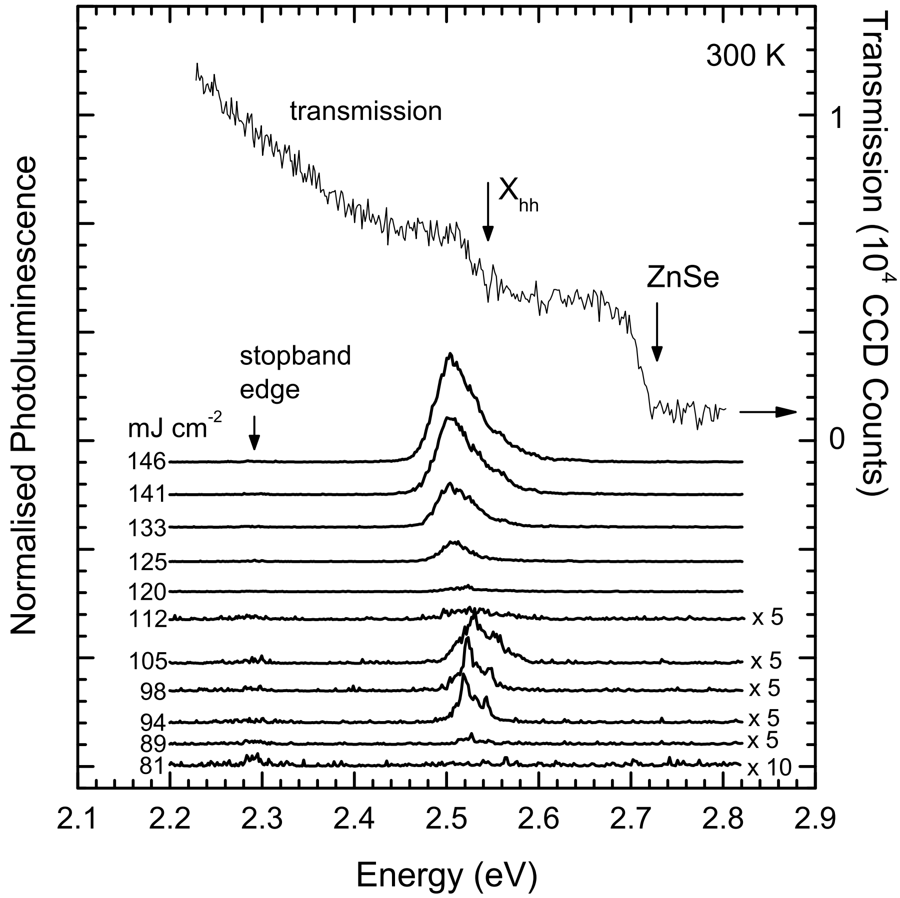

Figure 6.4: Photoluminescence spectra from the monolithic microcavity at room temperature for increasing excitation power. The top spectrum is the transmission of the bare quantum wells on the dielectric mirror. The heavy hole transition was estimated to be at 2.556 ± 0.1 eV by fitting the low energy shoulder of a Lorentzian curve to the transmission edge attributed to the exciton. Spectra are offset for clarity.

timated to be 210 nm from a low energy oscillation in the transmission spectra around 2.086 eV (not shown), confirming that the cavity mode is energetically out of reach of the exciton transitions at cryogenic temperatures. The completed microcavity photoluminescence spectra at room temperature for varying excitation power are presented in figure 6.4. The excitation pulses were increased from 81 to 175 mJ cm^{-2} (lowest spectrum corresponds to the lowest energy excitation). For low energy excitation, two peaks are observed at 2.518 and 2.543 eV. As the excitation energy is increased the dominant photoluminescence peak at 2.522 eV increases in intensity by an order of magnitude, followed by a sudden decrease in intensity for excitation energy of ~ 100 mJ cm^{-2}. For excitation energies above 110 mJ cm^{-2} a new peak emerges around

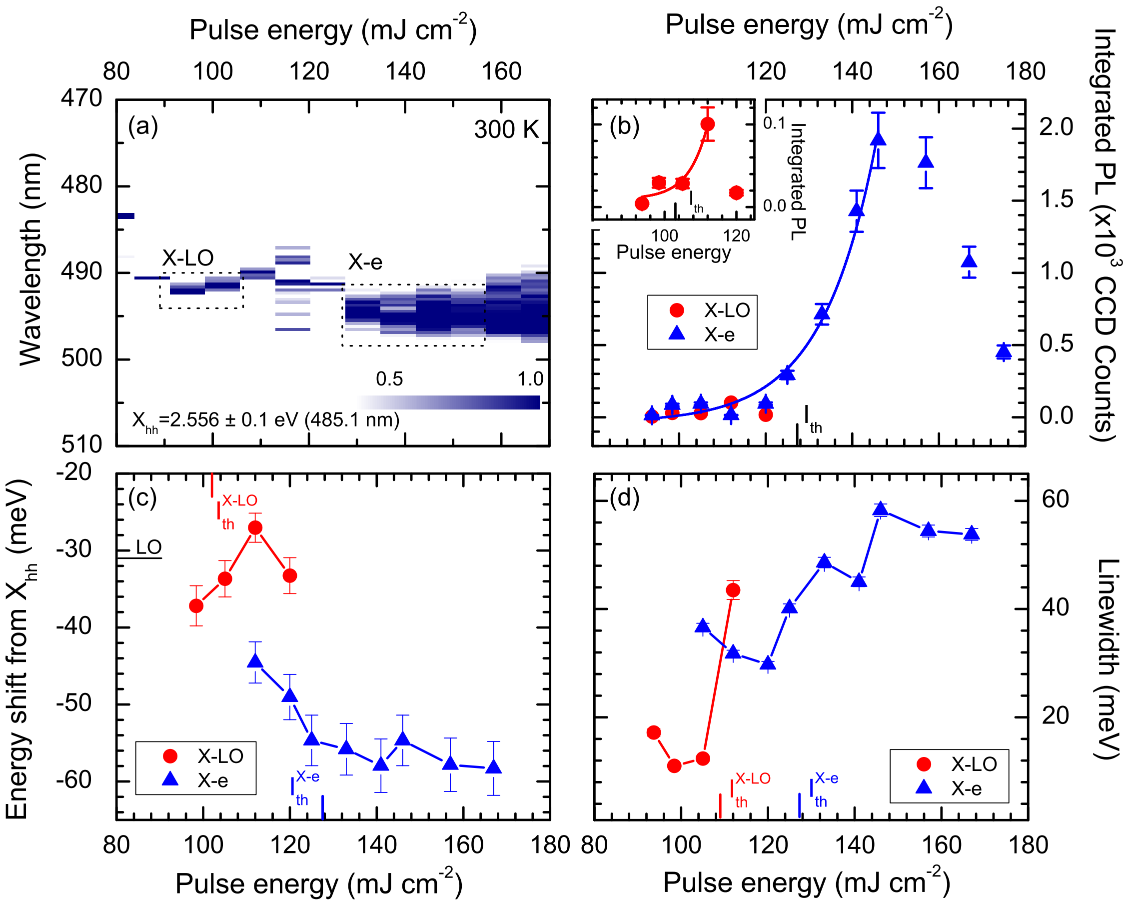

Figure 6.5: (a) Contour plot of the spectra from figure 6.4. The two lasing regions are indicated by the dotted boxes. (b) The integrated intensities (c) peak energy and (d) full width at half maximum of the two peaks. Exponential curves are fitted to the integrated intensities as guide to the eye. The threshold pulse energy is indicated in each plot.

2.507 eV and continues to grow exponentially until the excitation pulse energy reaches 150 mJ cm^{-2}. For higher pulse energies the photoluminescence intensity decreases. The entire experiment was found to be repeatable over a period of two weeks with no obvious signs of degradation. The device lifetime was not measured. Details of the power dependence of the microcavity are presented in figure 6.5. A contour plot of the spectra from figure 6.4 is presented in figure 6.5 (a) along with (b) the integrated intensities (c) peak energy and (d) full width at half maximum. The observed behaviour is clearly split into a low and high excitation regime.

6.2.1 Low excitation regime

Figure 6.5 (b) (inset) shows the integrated intensities of the peak observed for low excitations. An exponential curve has been fitted to the low excitation data as a guide to the eye (red line). The integrated photoluminescence increases by an order magnitude for 94 to 112 mJ cm^{-2}, a clear demonstration of superlinear behaviour with an estimated threshold of 103 ± 4 mJ cm^{-2}. Superlinear behaviour is further evidenced by narrowing of the photoluminescence peak to a minimum of 11 ± 0.4 meV near threshold, significantly narrower than either the bare heavy hole exciton transition or the cavity photon linewidths, ~ 30 meV (figure 6.5 (d)). The energetic position of the low excitation peak (around 2.518 eV), suggests an exciton-phonon scattering mechanism is behind the lasing characteristic. Phonon-assisted lasing can be described as an exciton $\rightarrow$ LO phonon + photon ($\hbar\omega_{em}$ = E_g - E_b - $\hbar\omega_{LO}$). The excitation pulse generates an e-h plasma that cools via phonon emission until Coulomb attraction between the electrons and holes form excitons at $\sim 2.556 \pm 0.1$ eV, as measured from the transmission spectrum of the bare quantum wells. The exciton then annihilates, emitting a phonon of ~ 31 meV [66] and a photon ($E_{hh} - \hbar\omega_{LO} \sim 2.525$ (491.0 nm)). The shift in the photoluminescence peak is presented in figure 6.5 (c). The energetic position of the low excitation peak at threshold is -33.6 ± 2.4 meV relative to the heavy hole exciton, and blue shifts for further increase in the excitation pulse energy above the threshold. Above 105 mJ cm^{-2} the phonon lasing mechanism appears to break down, the integrated intensity drops by an order of magnitude and the peak energy shifts to the red, before the peak completely disappears into the broad spontaneous emission around 2.52 eV. The break down of the phonon assisted lasing is attributed to screening affects of the e-h gas. The formation of excitons can only occur below a critical carrier density, above which the Coulomb potential is screened and the electron and holes can no longer couple to form excitons. The critical density can be calculated by equating the exciton Bohr radius to the Debye-Hückel screening length of an electron gas. However, to determine the injected carrier densities the excitation pulse width, carrier lifetime and the penetration depth into the microcavity must all be accurately measured and these parameters are not known in detail. The peak energy of the phonon-assisted lasing line clearly shifts toward the blue for increasing excitation, as seen in figure 6.5 (c). This can not be explained by band filling alone, since the energetic shift observed is of the order of 10 meV. Although the cavity polariton was not observed in the monolithic microcavity an interaction between the electric field and exciton can still result in the well documented exciton polariton [34, 67]. The intermixing of the exciton and photonic cavity leads to a significant reduction of the effective mass, even in the weak coupling regime. As the excitation energy is increased the density of exciton polaritons increases, causing a bottleneck at the anticrossing point on the exciton polariton dispersion curve. The bottleneck effect will energetically elevate the point where the exciton polariton can scatter too, thereby increasing the energy of the observed emission. The blue shift would then continue until a critical density is reached at which point the phonon assisted lasing will begin to break down. The observed red shift just before the peak completely disappears is attributing to the ionisation effect where only a portion of the exciton population is ionised, thereby reducing the bottleneck such that the remaining excitons can propagate further down the exciton polariton curve before emitting at a lower energy.

6.2.2 High excitation regime

The second optical feature present in figure 6.4 (a) is found in the high excitation spectra above 120 mJ cm^{-2}. The integrated intensities are presented in figure 6.5 (b) along with a fitted exponential curve as guide to the eye. A clear superlinear increase in the integrated photoluminescence is evident, with an estimated threshold of 122 ± 2 mJ cm^{-2}. As with the phonon-assisted lasing mechanism, the full width at half maximum narrows near threshold, to a minimum of $\sim 30 \pm 0.6$ meV. The optical

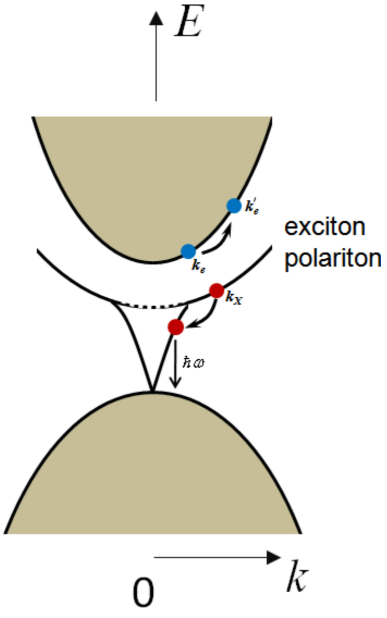

Figure 6.6: Schematic description of the exciton-electron scattering mechanism where the exciton is scattered to a photonic state on the exciton polariton dispersion, whilst the ionised e-h pair scatters to the conduction and valence bands, respectively.

features observed for high excitation can be described by exciton-electron assisted lasing. Modification of the dispersion curve due to the exciton polariton provides a photonic state, energetically below the exciton. A schematic of the modified dispersion is shown in figure 6.6. Exciton-electron scattering is the mechanism whereby the exciton is scattered to a photonic state on the exciton polariton dispersion, whilst the ionised e-h pair scatters in the conduction and valence bands, respectively, where the carriers diffuse. The energetic shift of the exciton-electron scattering has been calculated, [68] by calculating the spontaneous emission, via an integral over all possible exciton-electron configurations. The result is that the maximum energy shift for exciton-electron scattering is given by,

$$\hbar\omega_{em} = E_X - \alpha k_B T_c, \tag{6.2}$$

where the constant, α is material dependent and is given by the ratio of the exciton and electron effective mass [69, 70]. For the ZnCdSe quantum wells in this thesis α = $\frac{m_X^*}{2m_e^*}$

= 2.5, leading to a maximum theoretical red shift of 64.8 meV. For excitation energy $>$ 140 mJ cm^{-2} the observed redshift is $\sim 58 \pm 3$ meV. Hauksson [69] determined the α value for lasing in a ZnCdSe quantum heterostructure to be ~ 1.8 from a detailed temperature study. This corresponds to a redshift of 46.6 meV at the onset of lasing. From the data presented here, the lasing threshold is estimated to be 122 mJ $\pm$ 2 cm^{-2} at which point the energetic shift is 49 ± 3 meV.

A detailed temperature and sample dependent study of the lasing mechanism is required to complete the above analysis of the mechanism responsible for the superlinear behaviour observed. However, the data presented strongly suggests that at low excitation energies exciton-phonon scattering is occurring and for high excitation energies the exciton density is above the critical density for thermalization and exciton-electron scattering is observed.

Chapter 7

Concluding remarks and outlook

7.1 Summary

The design and fabrication of a variety ZnSe based microcavities was detailed in chapters 3 and 4. A novel epitaxial liftoff technique using MgS as a sacrificial layer was developed, perfected and successfully applied to the fabrication of three types of ZnSe based microcavities, that exhibit exciton photon hybridisation in the strong coupling regime up to room temperature.

The dispersion of the mixed state, the cavity polariton, was measured in momentum space using angle resolved transmission spectroscopy on a fixed microcavity (chapter 5 section 5.1) and successfully described using the coupled oscillator model. The oscillator strength of heavy hole ZnSe/$Zn_{0.19}Cd_{0.1}Se$ excitons (f_{hh}^{20K} = 1.29 $\times 10^{13}$ cm^{-2}) was deduced from the experimental observation and found to compare well with literature [13]. A study of the characteristic cavity polariton in k-space was presented and discussed. The observed composite ratios of the cavity polariton were found to differ from experimental findings for III-V microcavities. The intersection of the photonic fraction of the lower and upper polariton was found to occur above resonance and this was successfully understood by considering the asymmetry of the exciton absorbtion [54]. It was also proposed that motional narrowing is the only acceptable description of the observed lower polariton linewidth narrowing beyond resonance in momentum space.

In section 5.3 of chapter 5 a completely tunable microcavity was discussed that operated in the strong coupling regime. The experimental setup was completely cavity length tunable with nanometer precision. Reflection spectroscopy data was presented showing clear anticrossing of the heavy hole exciton and cavity photon. The presence of the cavity polariton bottleneck was evidenced with photoluminescence probing of the microcavity. The nonlinear optical features of two of the fabricated microcavities were presented in chapter 6. The first demonstration of cavity polariton bottleneck in the ZnSe material system was presented. The origins of the non-dispersive branch in momentum space were discussed. Finally, room temperature population inversion in a Ag-dielectric hybrid microcavity was evidenced. Room temperature power dependent photoluminescence of the hybrid device was presented and shown to exhibit two lasing mechanisms, a low pump power regime and a high power regime. The lasing mechanisms were understood to originate in exciton-phonon scattering and exciton-electron scattering, respectively.

7.2 Current status of ZnSe based microcavities

The inherently large oscillator strength along with the fabrication technique presented in this thesis, makes the ZnSe material system ideally suited to the study of cavity polariton physics. The works presented here strongly support ZnSe as a promising candidate for the observation of cavity polariton condensates at elevated temperatures. The epitaxial liftoff technology can potentially be developed to fabricate microcavities with ZnMgSSe/ZnSe quantum wells with even higher exciton binding energies, ~ 40 meV [71].

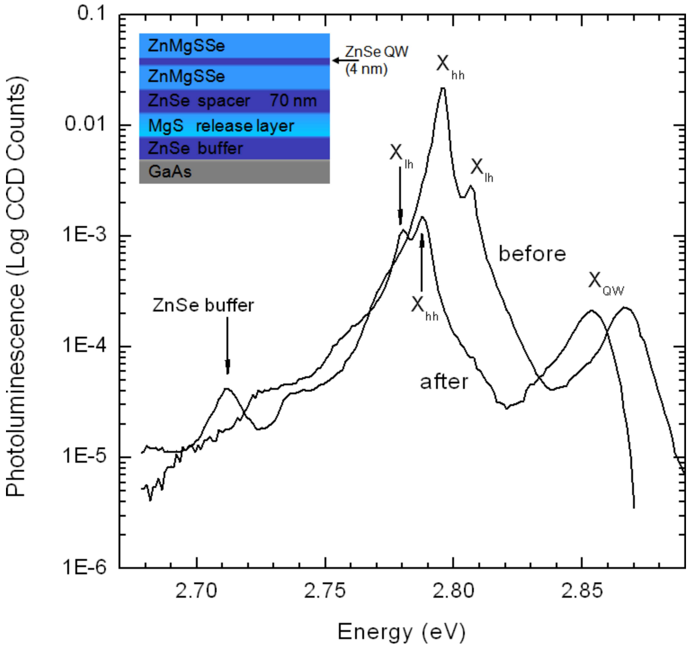

Figure 7.1: Photoluminescence from a ZnMgSSe/ZnSe quantum well heterostructure before and after liftoff. The prominent optical features around 2.8 eV are attributed to the heavy and light excitons of the thick ZnSe spacer. The emission before (after) liftoff at 2.866 (2.853) eV is attributed to thin ZnSe quantum well, confirming the ZnMgSSe barriers to be etch resistant. The integrated intensity before and after liftoff are equivalent evidencing the quantum efficiency to be unchanged by the liftoff process.

7.2.1 Improving the coupling strength in ZnSe based microcavities

In an effort to overcome the observed bottleneck, allowing polaritons to relax further toward a condensate, recent works have been undertaken to eliminate the cadmium alloy component of the microcavities presented here, thus increasing the oscillator strength and reducing exciton broadening. ZnMgSSe has been successfully shown to be resistant to the HCl etchant and single ZnSe quantum wells with ZnMgSSe barriers have been successfully lifted and transferred to fused silica substrates.

Figure 7.1 presents the photoluminescence before and after the liftoff technique. The heterostructure (figure 7.1 (inset)) was prepared and lifted as described in chapter 3. Three key spectral features are observed in the photoluminescence before and after liftoff. Due to the smaller lattice constant of GaAs compared to the rest of the materials used, the quantum well is under compressive strain before liftoff. After liftoff the large lattice parameter of the ZnMgSSe barriers dominates the structure and the result is that the quantum well is under tensile strain. This explains the observed red shift of the spectrum after liftoff. The prominent optical features around 2.8 eV are attributed to the heavy and light excitons of the thick ZnSe spacer. Before the liftoff there is a very wide ZnSe quantum well with ZnMgSSe and MgS barriers. After the liftoff the MgS barrier is replaced by a vacuum barrier and the free surface reduces the photoluminescence efficiency. This is why the ZnSe photoluminescence intensity drops by over an order of magnitude after liftoff. The red shift for the heavy and light hole exciton is a well understood phenomenon resulting from the transition from compressive to tensile strain. The crucial feature is the emission before (after) liftoff at 2.866 (2.853) eV which is attributed to thin ZnSe quantum well, confirming the ZnMgSSe barriers to be etch resistent. The quantum well integrated photoluminescence intensities before and after liftoff are very similar evidencing the quantum efficiency to be unchanged by the liftoff process. The relative intensities of the thin and thick quantum wells before and after liftoff is assumed to be due to carrier capture. Any e-h pairs excited in the thick ZnSe layer will go onto to form excitons, energetically below the thinner well. The key point is that the epitaxial liftoff technology has been successfully adapted and applied to a ZnSe/ZnMgSSe heterostructure. This is a very positive result and paves the way for the fabrication of ZnSe/ZnMgSSe microcavities.

Publications list

Journal papers

A. Balocchi, A. Curran, T. C. M. Graham, C. Bradford, K. A. Prior, and R. J. Warburton. Epitaxial lift-off of ZnSe-based heterostructures using a II-VI release layer. Appl. Phys. Lett. **86**, 011916 (2005).

C. Bradford, A. Curran, A. Balocchi, B. C. Cavenett, K. A. Prior, and R. J. Warburton. Epitaxial lift-off of MBE grown II-VI heterostructures using a novel MgS release layer. J. Crystal Growth **278**, 325 (2005).

T. C. M. Graham, A. Curran, X. Tang, J. K. Morrod, K. A. Prior, and R. J. Warburton. Direct and exchange Coulomb energies in CdSe/ZnSe quantum dots. Phys. Stat. Sol. B **243**, 782 (2006).

A. Curran, J. K. Morrod, K. A. Prior, A. K. Kar, and R. J. Warburton. Exciton-photon coupling in a ZnSe based microcavity fabricated using epitaxial liftoff. Semicond. Sci. Technol. (*IOP Select*). **22**, 1189 (2007).

A. Curran, R. J. Barbour, J. K. Morrod, K. A. Prior, A. K. Kar, and R. J. Warburton. ZnSe hybrid microcavities fabricated using a MgS release layer: Strong and weak exciton-photon coupling. J. Korean Phys. Soc. *in press*.

C. Bradford, R. T. Moug, A. Curran, D. Thuau, R. J. Warburton, and K. A. Prior. Growth and characterisation of ZnMgS grown by MBE on GaAs (100). J. Korean Phys. Soc. *in press*.

R. T. Moug, C. Bradford, D. Thuau, A. Curran, R. J. Warburton, and K. A. Prior. MBE growth and characterisation of MgS-rich zincblende $\mathrm{Zn}_x\mathrm{Mg}_{1-x}\mathrm{S}_{1-y}\mathrm{Se}_y$ alloys. J. Korean Phys. Soc. *in press*.

Conference presentations

C. Bradford, A. Curran, A. Balocchi, B. C. Cavenett, K. A. Prior, and R. J. Warburton. Epitaxial lift-off of MBE grown II-VI heterostructures using a novel MgS release layer. 11^{th} International Conference on II-VI Compounds, Edinburgh, U.K. (Aug 2004).

A. Curran, J. K. Morrod, R. Barbour, I. Weidle, R. Moug, C. Bradford, K. A. Prior, A. K. Kar, and R. J. Warburton. Angle resolved transmission spectroscopy of ZnSe-based microcavities fabricated using epitaxial liftoff technique. Conference on Lasers and Electro-Optics (CLEO), Baltimore, Maryland U.S.A. (May 2007).

A. Curran, J. K. Morrod, K. A. Prior, A. K. Kar, and R. J. Warburton. ZnSe-based microcavity fabricated using epitaxial liftoff. 7th Pacific Rim Conference on Lasers and Electro-Optics (CLEO PS), Seoul, South Korea (Aug 2007).

A. Curran, R. J. Barbour, J. K. Morrod, K. A. Prior, A. K. Kar, and R. J. Warburton. ZnSe hybrid microcavities fabricated using a MgS release layer: Strong and weak exciton-photon coupling. 13th International Conference on II-VI Compounds, Jeju, South Korea (Sept 2007).

A. Curran, R. J. Barbour, C. Bradford, J. K. Morrod, R. T. Moug, K. A. Prior and R. J. Warburton. Light-matter hybridisation in wide-bandgap ZnSe-based microcavities. UK Semiconductor 2008, Sheffield, U.K. (Jul 2008).

Media

Cover article featuring the works of A. Curran *et al.* R. Szweda. ELO MBE of II-VIs at Heriot-Watt. III-Vs Review. The Advanced Semiconductor Magazine **18**, 30 (2005).

References

[1] K. Iga, F. Koyama, and S. Kinoshita. Surface emitting semiconductor lasers. *IEEE J. Quantum Electron.* **24**, 1845 (1988).

[2] H. E. Li and K. Iga. *Vertical-cavity surface-emitting laser devices*. Springer, 7^{th} edition, 2003.

[3] C. Weisbuch, M. Nishioka, A. Ishikawa, and Y. Arakawa. Observation of the coupled exciton-photon mode splitting in a semiconductor quantum microcavity. *Phys. Rev. Lett.* **69**, 3314 (1992).

[4] M. S. Skolnick, T. A. Fisher, and D. M. Whittaker. Strong coupling phenomena in quantum microcavity structures. *Semicond. Sci. Technol.* **13**, 645 (1998).

[5] G. Khitrova, H. M. Gibbs, F. Jahnke, M. Kira, and S. W. Koch. Nonlinear optics of normal-mode-coupling semiconductor microcavities. *Rev. Mod. Phys.* **71**, 1591 (1999).

[6] P. G. Savvidis, J. J. Baumberg, R. M. Stevenson, M. S. Skolnick, D. M. Whittaker, and J. S. Roberts. Angle-resonant stimulated polariton amplifier. *Phys. Rev. Lett.* **84**, 1547 (2000).

[7] J. H. Dickerson, E. E. Mendez, A. A. Allerman, S. Manotas, F. Agulló-Rueda, and C. Pecharromán. Enhancement of Rabi splitting in a microcavity with an embedded superlattice. *Phys. Rev. B* **64**, 155302 (2001).

[8] M. Saba, C. Ciuti, J. Bloch, V. Thierry-Mieg, R. André, D. Le Si Dang, S. Kundermann, A. Mura, G. Bongiovanni, J. L. Staehli, and B. Deveaud. High-temperature ultrafast polariton parametric amplification in semiconductor microcavities. *Nature* **414**, 731 (2001).

[9] A. Imamoğlu, R. J. Ram, S. Pau, and Y. Yamamoto. Nonequilibrium condensates and lasers without inversion: Exciton-polariton lasers. *Phys. Rev. A* **53**, 4250 (1996).

[10] R. Houdré, C. Weisbuch, R. P. Stanley, U. Oesterle, P. Pellandini, and M. Ilegems. Measurement of cavity-polariton dispersion curve from angle-resolved photoluminescence experiments. *Phys. Rev. Lett.* **73**, 2043 (1994).

[11] S. Pau, H. Cao, J. Jacobson, G. Björk, Y. Yamamoto, and A. Imamoğlu. Observation of a laserlike transition in a microcavity exciton polariton system. *Phys. Rev. A* **54**, R1789 (1996).

[12] M. Kira, F. Jahnke, S. W. Koch, J. D. Berger, D. V. Wick, T. R. Nelson, G. Khitrova, and H. M. Gibbs. Quantum theory of nonlinear semiconductor microcavity luminescence explaining “boser” experiments. *Phys. Rev. Lett.* **79**, 5170 (1997).

[13] P. Kelkar, V. Kozlov, H. Jeon, A. V. Nurmikko, C. C. Chu, D. C. Grillo, J. Han, C. G. Hua, and R. L. Gunshor. Excitons in a II-VI semiconductor microcavity in the strong-coupling regime. *Phys. Rev. B* **52**, R5491 (1995).

[14] R. André, D. Heger, D. Le Si Dang, and Y. M. d’Aubigné. Spectroscopy of polaritons in CdTe-based microcavities. *J. Crys. Growth* **184**, 758 (1998).

[15] D. Le Si Dang, D. Heger, R. André, F. Bœuf, and R. Romestain. Spectroscopy of polaritons in CdTe-based microcavities. *J. Crys. Growth* **184**, 758 (1998).

[16] N. Antoine-Vincent, F. Natali, D. Byrne, A. Vasson, P. Disseix, J. Leymarie, M. Leroux, F. Semond, and J. Massies. Observation of Rabi splitting in a bulk GaN microcavity grown on silicon. *Phys. Rev. B* **68**, 153313 (2003).

[17] D. Le Si Dang, D. Heger, R. André, F. Bœuf, and R. Romestain. Stimulation of polariton photoluminescence in semiconductor microcavity. *Phys. Rev. Lett.* **81**, 3920 (1998).

[18] J. Kasprzak, M. Richard, S. Kundermann, A. Baas, P. Jeambrun, J. M. J. Keeling, F. M. Marchetti, M. H. Szymańska, R. André, J. L. Staehli, V. Savona, P. B. Littlewood, B. Deveaud, and D. Le Si Dang. Bose-Einstein condensation of exciton polaritons. *Nature* **443**, 409 (2006).

[19] M. Leroux, N. Grandjean, M. Laügt, J. Massies, B. Gil, P. Lefebvre, and P. Bigenwald. Quantum confined Stark effect due to built-in internal polarization fields in (Al,Ga)N/GaN quantum wells. *Phys. Rev. B* **58**, R13371 (1998).

[20] E. Feltin, G. Christmann, R. Butté, J. Carlin, M. Mosca, and N. Grandjean. Room temperature polariton luminescence from a GaN/AlGaN quantum well microcavity. *Appl. Phys. Lett.* **89**, 071107 (2006).

[21] S. Christopoulos, G. B. H. von Högersthal, A. J. D. Grundy, P. G. Lagoudakis, A. V. Kavokin, J. J. Baumberg, G. Christmann, R. Butté, E. Feltin, J.-F. Carlin, and N. Grandjean. Room-temperature polariton lasing in semiconductor microcavities. *Phys. Rev. Lett.* **98**, 126405 (2007).

[22] I. C. Robin, R. André, A. Balocchi, S. Carayon, S. Moehl, J. M. Gérard, and L. Ferlazzo. Purcell effect for CdSe/ZnSe quantum dots placed into hybrid micropillars. *Appl. Phys. Lett.* **87**, 233114 (2005).

[23] K. A. Prior, private communication.

[24] M. D. Sturge. Optical absorption of gallium arsenide between 0.6 and 2.75 eV. *Phys. Rev.* **127**, 768 (1962).

[25] J. S. Blakemore. Semiconducting and other major properties of gallium arsenide. *J. Appl. Phys.* **53**, R123 (1982); M. Aven and B. Segall. Carrier mobility and shallow impurity states in ZnSe and ZnTe. *Phys. Rev.* **130**, 81 (1963); M. Aven, D. T. F. Marple, and B. Segall. Some electrical and optical properties of ZnSe. *J. Appl. Phys.* **32**, 2261 (1961).

[26] C. Weisbuch and B. Vinter. *Quantum semiconductor structures: Fundamentals and applications*. Academic Press, 1991.

[27] L. Esaki and R. Tsu. Superlattice and negative differential conductivity in semiconductors. *IBM J. Dev.* **14**, 61 (1970).

[28] L. Esaki and L. L. Chang. New transport phenomenon in a semiconductor "Superlattice". *Phys. Rev. Lett.* **33**, 495 (1974).

[29] R. Dingle, W. Wiegmann, and C. H. Henry. Quantum states of confined carriers in very thin Al$_x$Ga$_{1-x}$As-GaAs/Al$_x$Ga$_{1-x}$As heterostructures. *Phys. Rev. Lett.* **33**, 827 (1974).

[30] Y. Zhu, D. J. Gauthier, S. E. Morin, Q. Wu, H. J. Carmichael, and T. W. Mossberg. Vacuum Rabi splitting as a feature of linear-dispersion theory: Analysis and experimental observations. *Phys. Rev. Lett.* **64**, 2499 (1990).

[31] H. A. MacLeod. *Thin film optical filters*. Institute of Physics Publishing, 3rd edition, 2001.

[32] M. Born and E. Wolf. *Principles of optics*. Cambridge University Press, 7th edition, 1999.

[33] D. I. Babic and S. W. Corzine. Analytic expressions for the reflection delay, penetration depth, and absorptance of quarter-wave dielectric mirrors. *IEEE J. Quantum Electron.* **28**, 514 (1992).

[34] J. J. Hopfield. Theory of the contribution of excitons to the complex dielectric constant of crystals. *Phys. Rev.* **112**, 1555 (1958).

[35] C. Ciuti, P. Schwendimann, and A. Quattropani. Theory of polariton parametric interactions in semiconductor microcavities. *Semicond. Sci. Technol.* **18**, S279 (2003).

[36] A. Curran, J. K. Morrod, K. A. Prior, A. K. Kar, and R. J. Warburton. Exciton-photon coupling in a ZnSe-based microcavity fabricated using epitaxial liftoff. *Semicond. Sci. Technol.* **2**, 1189 (2007).

[37] O. Madelung, editor. *Semiconductors - Basic data*. Springer, 2^{nd} edition, 1996.

[38] A. Pawlis, A. Khartchenko, O. Husberg, D. L. As, K. Lischka, and D. Schikora. Large room temperature Rabi-splitting in a ZnSe/(Zn,Cd)Se semiconductor microcavity structure. *Sol. Stat. Comm.* **123**, 235 (2002).

[39] H. Lohmeyer, K. Sebald, C. Kruse, R. Kröger, J. Gutowski, D. Hommel, J. Wiersig, N. Baer, and F. Jahnke. Confined optical modes in monolithic II-VI pillar microcavities. *Appl. Phys. Lett.* **88**, 51101 (2006).

[40] A. Balocchi, A. Curran, T. C. M. Graham, C. Bradford, K. A. Prior, and R. J. Warburton. Epitaxial lift-off of ZnSe-based heterostructures using a II-VI release layer. *Appl. Phys. Lett.* **86**, 011916 (2005).

[41] J. K. Morrod. *Growth and characterisation of II-VI wide band-gap heterostructures and nanostructures*. PhD thesis, Heriot-Watt University, 2006.

[42] C. Bradford, C. B. O'Donnell, B. Urbaszek, A. Balocchi, C. Morhain, K. A. Prior, and B. C. Cavenett. Growth of Zinc blende MgS and MgS/ZnSe quantum wells by MBE using ZnS as a sulphur source. *J. Cryst. Growth* **227**, 634 (2001).

[43] E. Yablonovitch, T. Gmitter, J. P. Harbison, and R. Bhat. Extreme selectivity in the lift-off of epitaxial GaAs films. *Appl. Phys. Lett.* **51**, 2222 (1987).

[44] J. Maeda, Y. Sasaki, N. Dietz, K. Shibahara, S. Yokoyama, S. Miyazaki, and M. Hirose. High-rate GaAs epitaxial lift-off technique for optoelectronic integrated circuits. *Jpn. J. Appl. Phys.* **36**, 1554 (1997).

[45] E. Yablonovitch, D. M. Hwang, T. J. Gmitter, L. T. Florez, and J. P. Harbison. Van der Waals bonding of GaAs epitaxial liftoff films onto arbitrary substrates. *Appl. Phys. Lett.* **56**, 2419 (1990).

[46] M. Saba, C. Ciuti, S. Kundermann, J. L. Staehli, B. Deveaud, J. Bloch, V. Thierry-Mieg, R. André, D. Le Si Dang, G. Bongiovanni, and A. Mura. Towards a room temperature polariton amplifier. *Phys. Stat. Sol (a)* **190**, 315 (2002).

[47] R. R. Alfano and S. L. Shapiro. Observation of self-phase modulation and small-scale filaments in crystals and glasses. *Phys. Rev. Lett.* **24**, 592 (1970).

[48] R. Pässler. Temperature dependence of exciton peak energies in multiple quantum wells. *Appl. Phys. Lett.* **83**, 3356 (1998).

[49] A. Kavokin and G. Malpuech. *Cavity polaritons*. Thin Films and Nanostructures. Elsevier, 2003.

[50] V. Savona, L. C. Andreani, P. Schwendimann, and A. Quattropani. Quantum well excitons in semiconductor microcavities: Unified treatment of weak and strong coupling regimes. *Solid State Comm.* **93**, 733 (1995).

[51] J. Tignon, P. Voisin, C. Delalande, M. Voos, R. Houdré, U. Oesterle, and R. P. Stanley. From Fermi's Golden Rule to the Vacuum Rabi Splitting: Magnetopolaritons in a Semiconductor Optical Microcavity. *Phys. Rev. Lett.* **74**, 3967 (1995).

[52] D. M. Whittaker, P. Kinsler, T. A. Fisher, M. S. Skolnick, A. Armitage, A. M. Afshar, M. D. Sturge, and J. S. Roberts. Motional narrowing in semiconductor microcavities. *Phys. Rev. Lett.* **77**, 4792 (1996).

[53] A. V. Kavokin. Motional narrowing of inhomogeneously broadened excitons in a semiconductor microcavity: Semiclassical treatment. *Phys. Rev. B* **57**, 3757 (1998).

[54] A. Armitage, D. G. Lidzey, D. D. C. Bradley, T. Virgili, M. S. Skolnick, and S. Walker. Modelling of asymmetric excitons in organic microcavities. *Synthetic Metals* **111**, 377 (2000).

[55] C. Ell, J. Prineas, T. R. Nelson, Jr, S. Park, H. M. Gibbs, G. Khitrova, S. W. Koch, and R. Houdré. Influence of structural disorder and light coupling on the excitonic response of semiconductor microcavities. *Phys. Rev. Lett.* **80**, 4795 (1998).

[56] V. Savona and R. Zimmermann. Time-resolved Rayleigh scattering of excitons: Evidence for level repulsion in a disordered system. *Phys. Rev. B* **60**, 4928 (1999).

[57] G. Kocherscheidt, W. Langbein, U. Woggon, V. Savona, R. Zimmermann, D. Reuter, and A. D. Wieck. Resonant Rayleigh scattering dynamics of excitons in single quantum wells. *Phys. Rev. B* **68**, 085207 (2003).

[58] M. Müller, J. Bleuse, and R. André. Dynamics of the cavity polariton in CdTe-based semiconductor microcavities: Evidence for a relaxation edge. *Phys. Rev. B* **62**, 16886 (2000).

[59] F. Stokker-Cheregi, A. Vinattieri, F. Semond, M. Leroux, I. R. Sellers, J. Massies, D. Solnyshkov, G. Malpuech, M. Colocci, and M. Gurioli. Polariton relaxation bottleneck and its thermal suppression in bulk GaN microcavities. *Appl. Phys. Lett.* **92**, 042119 (2008).

[60] C. Ciuti, P. Schwendimann, B. Deveaud, and A. Quattropani. Theory of the angle-resonant polariton amplifier. *Phys. Rev. B* **62**, R4825 (2000).

[61] C. Ciuti, P. Schwendimann, and A. Quattropani. Parametric luminescence of microcavity polaritons. *Phys. Rev. B* **63**, 041303 (2001).

[62] P. G. Savvidis, C. Ciuti, J. J. Baumberg, D. M. Whittaker, M. S. Skolnick, and J. S. Roberts. Off-branch polaritons and multiple scattering in semiconductor microcavities. *Phys. Rev. B* **64**, 075311 (2001).

[63] M. Richard, J. Kasprzak, R. André, D. Le Si Dang, and R. Romestain. Angle resolved spectroscopy of polariton stimulation under non-resonant excitation in CdTe II-VI microcavity. *J. Phys.: Condens. Matter* **16**, S3683 (2004).

[64] M. Lomascolo, M. D. Dio, D. Greco, L. Calcagnile, R. Cingolani, L. Vanzetti, L. Sorba, and A. Franciosi. Free versus localized exciton recombination in Zn$_{1-x}$Cd$_x$Se/ZnSe multiple quantum wells. *Appl. Phys. Lett.* **69**, 1145 (1996).

[65] Y. Kawakami, M. Funato, S. Fujita, S. Fujita, Y. Yamada, and Y. Masumoto. Localized excitons in cubic Zn$_{1-x}$Cd$_x$S lattice matched to GaAs. *Phys. Rev. B* **50**, 14655 (1994).

[66] W. Mereditha, G. Horsburgh, G. D. Brownlie, K. A. Prior, B. C. Cavenett, W. Rothwell, and A. J. Dann. Microprobe Raman study of the variation of LO phonon frequency with the Cd concentration in the ternary compound Zn$_{1-x}$Cd$_x$Se. *J. Crystal Growth* **159**, 103 (1996).

[67] C. Benoit a la Guillaume, A. Bonnot, and J. M. Debever. Luminescence from Polaritons. *Phys. Rev. Lett.* **24**, 1235 (1970).

[68] T. Fischer and J. Bille. Recombination processes in highly excited CdS. *J. Appl. Phys.* **45**, 3937 (1974).

[69] I. S. Hauksson. *Investigation of spontaneous and stimulated emission from ZnSe epilayers and ZnCdSe/ZnSe quantum well systems grown by molecular beam epitaxy*. PhD thesis, Heriot-Watt University, 1996.

[70] Y. Kawakami, I. Hauksson, H. Stewart, J. Simpson, I. Galbraith, K. A. Prior, and B. C. Cavenett. Exciton-related lasing mechanism in ZnSe-(Zn,Cd)Se multiple quantum wells. *Phys. Rev. B* **48**, 11994 (1993).

[71] B. Urbaszek, C. Morhain, C. Bradford, C. B. O'Donnell, S. A. Telfer, X. Tang, A. Balocchi, K. A. Prior, B. C. Cavenett, C. M. Townsley, and R. J. Nicholas. Excitons with large binding energies in MgS/ZnSe/MgS and ZnMgS/ZnS/ZnMgS quantum wells. *J. Phys. Condens. Matter* **13**, 2317 (2001).